

**Using thermal infrared (TIR) data to characterize dust storms and their sources in the Middle East**

by

Redha Mohammad

Bachelors of Science, University of Oregon, 2002

Masters of Science, University of Pittsburgh, 2008

Submitted to the Graduate Faculty of  
the Kenneth P. Dietrich School of  
Arts and Sciences in partial fulfillment  
of the requirements for the degree of  
Doctor of Philosophy

University of Pittsburgh

2012

UNIVERSITY OF PITTSBURGH  
KENNETH P. DIETRICH SCHOOL OF ARTS AND SCIENCES

This dissertation was presented

by

Redha Mohammad

It was defended on

May 1, 2012

and approved by

William Harbert, Professor, University of Pittsburgh

Michael Rosenmeier, Adjunct Faculty, University of Pittsburgh

Charles Jones, Lecturer, University of Pittsburgh

Dissertation Advisor: Michael Ramsey, Associate Professor, University of Pittsburgh

Nicholas Lancaster, Research Professor, Desert Research Institute, Reno, Nevada

Stephen Scheidt, Research Scientist, Smithsonian Institution

Copyright © by Redha Mohammad

2012

# **Using thermal infrared (TIR) data to characterize dust storms and their sources in the Middle East**

Redha Mohammad, PhD

University of Pittsburgh, 2012

Mineral dust and aerosols can directly and indirectly influence shortwave and longwave radiative forcing. In addition, it can cause health hazards, loss of agricultural soil, and safety hazards to aviation and motorists due to reduced visibility. Previous work utilized satellite and ground-based Thermal Infrared (TIR) data to measure aerosol content in the atmosphere. This research used TIR techniques, by creating a fine-grained (2.7-45  $\mu\text{m}$ ) mineral spectral library, direct laboratory emission spectroscopic analysis, and spectral and image deconvolution models, to characterize both the mineral content and particle size of dust storms affecting Kuwait. These results were validated using a combination of X-ray Diffraction (XRD) and Scanning Electron Microscopy (SEM) analyses that were performed on dust samples for three dust storms (May, July 2010, March 2011) from Kuwait. A combination of forward and backward Hybrid Single-Particle Lagrangian Integrated Trajectory (HYSPLIT) models were used to track air parcels arriving in Kuwait at the time of dust storm sample collection, thus testing the link to dust emitting areas or hotspots in eastern Syria and western Iraq. World soil maps and TIR analysis of surface deposits of these potential hotspots support this interpretation, and identified areas of high calcite concentration. This interpretation was in agreement with prior studies identifying calcite as the major mineral in dust storms affecting Kuwait. Spectral and image deconvolution models provided good tools in estimating mineral end members present in both dust samples and satellite plumes, but failed to identify the accurate particle size fractions present.

## TABLE OF CONTENTS

<b>PREFACE.....</b>	<b>XIX</b>
<b>1.0 INTRODUCTION.....</b>	<b>1</b>
<b>2.0 DUST STORMS IN THE MIDDLE EAST: FORMATION, EXTENT, AND EFFECTS.....</b>	<b>4</b>
<b>2.1 INTRODUCTION AND STUDY GOALS .....</b>	<b>4</b>
<b>2.2 DESCRIPTION OF STUDY AREA .....</b>	<b>5</b>
<b>2.2.1 Regional Climate .....</b>	<b>5</b>
<b>2.2.2 Geology and Surface Deposits .....</b>	<b>6</b>
<b>2.3 DUST STORMS.....</b>	<b>13</b>
<b>2.3.1 Formation of Dust Storms .....</b>	<b>15</b>
<b>2.3.1.1 Dust Source .....</b>	<b>16</b>
<b>2.3.1.2 Threshold Velocity .....</b>	<b>17</b>
<b>2.3.1.3 Particle Deposition .....</b>	<b>19</b>
<b>2.3.2 Dust Composition .....</b>	<b>19</b>
<b>2.3.3 Dust Storm Impact .....</b>	<b>20</b>
<b>2.3.3.1 Geologic Impact.....</b>	<b>20</b>
<b>2.3.3.2 Environmental Impact.....</b>	<b>22</b>
<b>2.3.3.3 Health Impact.....</b>	<b>24</b>

<b>2.4</b>	<b>MEASUREING DUST .....</b>	<b>26</b>
2.4.1	Total Ozone Mapping Spectrometer (TOMS) .....	26
2.4.2	Atmospheric Infrared Sounder (AIRS).....	28
<b>2.5</b>	<b>SUMMARY .....</b>	<b>28</b>
<b>3.0</b>	<b>THERMAL INFRARED SPECTROSCOPY OF SILICATE DUST .....</b>	<b>30</b>
<b>3.1</b>	<b>INTRODUCTION .....</b>	<b>30</b>
<b>3.2</b>	<b>SILICATE THERMAL EMISSION SPECTRA .....</b>	<b>31</b>
<b>3.3</b>	<b>PARTICLE SIZE EFFECT.....</b>	<b>33</b>
<b>3.4</b>	<b>METHODOLOGY .....</b>	<b>36</b>
3.4.1	Dust Collection.....	36
3.4.2	XRD and SEM Analyses .....	39
3.4.3	Spectroscopic Analysis .....	41
3.4.4	Creation of Dust Spectral Library .....	42
<b>3.5</b>	<b>RESULTS .....</b>	<b>45</b>
3.5.1	XRD and CCSEM.....	45
3.5.2	Fine Particles Library .....	48
	Andesine.....	48
	Calcite .....	48
	Dolomite.....	51
	Fayalite.....	53
	Forsterite .....	54
	Kaolinite.....	56
	Muscovite.....	57

		Quartz .....	57
	3.5.3	Dust Spectroscopic Analysis .....	61
	3.6	DISCUSSION.....	78
	3.7	CONCLUSION .....	81
4.0		THERMAL INFRARED REMOTE SENSING OF DUST STORMS IN THE MIDDLE EAST.....	83
	4.1	INTRODUCTION .....	83
	4.2	BACKGROUND AND PREVIOUS WORK.....	83
	4.3	METHODOLOGY .....	85
	4.3.1	Forward and Back Trajectory Models .....	85
	4.3.2	Satellite Data Acquisition.....	96
	4.3.3	Processing of Satellite Data.....	98
	4.4	RESULTS .....	106
	4.4.1	Clear Scenes .....	106
	4.4.2	Dusty Scenes.....	111
	4.5	DISCUSSION.....	120
	4.6	CONCLUSION .....	122
5.0		SUMMARY .....	125
		APPENDIX A .....	129
		APPENDIX B .....	132
		APPENDIX C .....	138
		APPENDIX D .....	143
		BIBLIOGRAPHY.....	147

## LIST OF TABLES

Table 2.1 Difference threshold velocities for surfaces in the United States SW region (Goudie and Middleton, 2006).....	18
Table 2.2 Different threshold velocities for desert surfaces (Edgell, 2006).....	19
Table 2.3 Lyles et al. (2005) identified 147 bacterial colony forming units (CFU) on military personnel in Kuwait. ....	25
Table 3.1 Dates and times of dust storm samples collected for analysis.....	39
Table 3.2 Different combinations of spectral libraries created for this analysis. ....	43
Table 3.3 XRD results outlining major minerals found in the dust samples. ....	47
Table 3.4 Spectral deconvolution results for calcite, quartz, and forsterite mixtures.....	75
Table 4.1 Type, criteria, and purpose for selecting satellite data for analysis.....	97
Table 4.2 Image deconvolution results for clear ASTER and MODIS data.....	110
Table 4.3 Image deconvolution results for one clear ASTER scene. ....	111
Table 4.4 Image deconvolution results for dusty ASTER and MODIS data.....	112



## LIST OF FIGURES

Figure 2.1 Monthly average temperature and precipitation in Kuwait (Al-Sulaimi et al., 1997)...	6
Figure 2.2 Tectonic and geologic map of the Arabian Peninsula (modified from USGS digital soils map of the world). .....	9
Figure 2.3 TOMS Aerosol Index (AI) values identified Africa and the Middle East as the world's largest dust emitters (modified from Washington et al., 2003) .....	14
Figure 2.4 Haboobs form ahead of cold fronts and can reach as high as 2 km, like this storm affecting the suburb of Al-Mangaf in Kuwait on March 25, 2011 (Kuwait International Airport, <a href="http://www.dgca.gov.kw">www.dgca.gov.kw</a> ). .....	15
Figure 2.5 Composition of various dust samples collected throughout the Middle East showing variation in dust content within a relatively small area like Kuwait (Engelbrecht et al., 2009). Higher levels of carbonates found in Iraq and in dust storms affecting Kuwait indicate a source near Iraq. ....	21
Figure 2.6 Annual mean AI map based on TOMS observations. Much of the Middle East and Northern Africa have values higher than 1.50, indicating higher levels of aerosols (Engelstaedter et al., 2007). .....	27

Figure 3.1 Much of the TIR region is obscured due to the presence of carbon dioxide, water, and ozone gases, thus limiting the usable window to the 8-12  $\mu\text{m}$  region (modified from Sabins, 1997). ..... 30

Figure 3.2 Minerals have unique spectral features or signatures in the TIR region (modified from Ramsey and Christensen, 1998). ..... 32

Figure 3.3 Volume scattering dominates as particle size decreases, resulting in spectral features losing their contrast whereas maintaining their general shape. Arrows point to different quartz grain sizes and show the decrease in spectral contrast with decreasing particle size. .... 34

Figure 3.4 Forsterite has emissivity lows (reststrahlen bands) at 10  $\mu\text{m}$  (red arrow). At longer wavelengths, a second set of emissivity lows, called transparency features, forms with finer particle sizes (blue arrow). ..... 35

Figure 3.5 A simplified version of the CAPYR method for collecting dust was used. A. General location of the filter, and B. close up of filter, showing a coating of dust. .... 38

Figure 3.6 SEM image showing individual dust particles under 500X magnification. .... 41

Figure 3.7 Composition of various dust samples collected throughout the Middle East, showing variation in dust content (Engelbrecht et al., 2009). Higher levels of carbonates found in Iraq and in dust storms affecting Kuwait indicate a source near Iraq. .... 46

Figure 3.8 Particle size distribution identified by CCSEM for the three dust storm samples (a = May 2010, b = July 2010, c = March 2011) shows 60% of particles were in the 1-4  $\mu\text{m}$  size range. .... 49

Figure 3.9 Coarse (>125  $\mu\text{m}$ ) andesine spectrum from ASU's spectral library (Christensen et al., 2000) ..... 50

Figure 3.10 Andesine spectral library showing a reflectance feature at 9.2 $\mu\text{m}$ (blue arrow) and a transparency feature at 11.8 $\mu\text{m}$ (red arrow).....	51
Figure 3.11 Coarse (>125 $\mu\text{m}$ ) calcite spectrum from ASU’s spectral library (Christensen et al., 2000). .....	52
Figure 3.12 Calcite spectral library showing emissivity lows at 6.5 $\mu\text{m}$ and 11.3 $\mu\text{m}$ (blue arrows) and transparency features (red arrows).....	52
Figure 3.13 Coarse (>125 $\mu\text{m}$ ) dolomite spectrum from ASU’s spectral library (Christensen et al., 2000). .....	53
Figure 3.14 Dolomite spectral library showing emissivity lows at 6.4 $\mu\text{m}$ and 10.8 $\mu\text{m}$ (blue arrows) and transparency features (red arrows).....	54
Figure 3.15 Coarse (>125 $\mu\text{m}$ ) fayalite spectrum from ASU’s spectral library (Christensen et al., 2000). .....	55
Figure 3.16 Spectra of the fayalite mixture showed an emissivity low at 9 $\mu\text{m}$ , indicating the presence of other minerals in the mixture, whereas pure fayalite has an emissivity low at 11.5 $\mu\text{m}$ . .....	55
Figure 3.17 Coarse (>125 $\mu\text{m}$ ) forsterite spectrum from ASU’s spectral library (Christensen et al., 2000). .....	56
Figure 3.18 Forsterite spectral library showing an emissivity low at 10.4 $\mu\text{m}$ (blue arrow) and a transparency feature (red arrow).....	57
Figure 3.19 Coarse (>125 $\mu\text{m}$ ) kaolinite spectrum from ASU’s spectral library (Christensen et al., 2000). .....	58
Figure 3.20 Spectral data obtained from ASU’s spectral library was used to plot a single size fraction spectrum of kaolinite. It has an emissivity low at 9.2 $\mu\text{m}$ (blue arrow). .....	58

Figure 3.21 Coarse (>125 $\mu\text{m}$ ) muscovite spectrum from ASU's spectral library (Christensen et al., 2000).	59
Figure 3.22 Muscovite spectra show an emissivity feature at 9.6 $\mu\text{m}$ (blue arrow) and no transparency feature.	59
Figure 3.23 Coarse (>125 $\mu\text{m}$ ) quartz spectrum from ASU's spectral library (Christensen et al., 2000).	60
Figure 3.24 Quartz spectra show the distinct doublet feature at 9.1 $\mu\text{m}$ (blue arrow) and transparency feature (red arrow).	60
Figure 3.25 Emissivity spectrum generated by the May storm. The arrows show the quartz and calcite features.	61
Figure 3.26 Spectrum of the July storm shows calcite features at 6.5 $\mu\text{m}$ and 11.3 $\mu\text{m}$ (highlighted by arrows).	63
Figure 3.27 Spectrum of the March storm shows a calcite feature at 11.3 $\mu\text{m}$ (highlighted by arrow).	64
Figure 3.28 Modeled spectral unmixing using all 28-end members. Despite the prominent quartz spectral feature in the May spectrum (solid line), the model did not identify quartz as an end member.	65
Figure 3.29 Modeled spectral unmixing using end members from the ASU spectral library. Despite the relatively low RMS value of 0.0106, the modeled (dashed line) spectrum is off.	66
Figure 3.30 Unmixing with C+K+Q end members produced a very poor compositional fit.	67
Figure 3.31 Unmixing with C+Q end members produced similarly poor results as unmixing with C+K+Q.	67

Figure 3.32 Unmixing July storm spectrum with all 28-end member library did not result in a good model fit.....	69
Figure 3.33 Unmixing with ASU’s spectral library had a relatively good fit in the 8-12 $\mu\text{m}$ region, whereas outside of that range the fit was poor. ....	70
Figure 3.34 Unmixing with C+K+Q end members produced a poor model fit.....	71
Figure 3.35 Unmixing with C+Q end members resulted in a poor fit and a high RMS value .....	71
Figure 3.36 Unmixing of March spectrum with all 28-end member library resulted in a low RMS value and the model retained most of the mixed spectral features, although they were slightly shifted to shorter wavelength.....	72
Figure 3.37 Unmixing with ASU’s spectral library produced a good fit in the 8.5 – 11 $\mu\text{m}$ , with high errors outside of that region. Compositional end members identified were not accurate. ..	73
Figure 3.38 Unmixing with C+K+Q end members produced a poor fit, whereas compositional results were relatively accurate and similar to XRD results. ....	74
Figure 3.39 Unmixing with C+Q end members produced a very poor fit, whereas the compositional results were similar to unmixing with C+K+Q and XRD results. ....	74
Figure 3.40 Spectral deconvolution of a calcite and quartz 50:50 mixture using only 2 end members (calcite <10, quartz 10-20). ....	76
Figure 3.41 Spectral deconvolution of a calcite and quartz 75:25 mixture using only 2 end members (calcite <10, quartz 10-20). ....	77
Figure 3.42 Spectral deconvolution of a calcite, quartz, and forsterite 31:31:38 mixture using only 3 end members (calcite <10, forsterite and quartz 10-20). ....	77

Figure 3.43 Effects of volume scattering from smaller particles can be seen in the intensification of transparency feature troughs. Arrow point to the positions of each particle size fraction, and show that the smallest particle fraction had the deepest trough..... 78

Figure 4.1 HYPSLIT back trajectory model results at different elevations starting over Syria and Southern Turkey beginning May 11, 2010 and ending 48 hours later in Kuwait (black star). Red = 500 m, blue = 2000 m, green = 3000 m..... 87

Figure 4.2 HYPSLIT back trajectory model results at different elevations starting over Turkey and Northern Africa beginning July 15, 2010 and ending 96 hours later in Kuwait (black star). Red = 500 m, blue = 2000 m, green = 3000 m. .... 88

Figure 4.3 HYPSLIT back trajectory model results at different elevations starting over Syria (2000 m), Sinai desert (2000 m), and Saudi Arabia (surface level) beginning March 23, 2011 and ending 48 hours later in Kuwait (black star). By far this is the most complex of all three models. Red = 500m, blue = 2000m, green = 3000m. .... 89

Figure 4.4 HYPSLIT forward trajectory model results at 500, 1000, and 2000 m elevations starting over hotspot in eastern Syria beginning May 11, 2010 and ending 48 hours later over Iraq, Turkey, and Russia. Red = 500 m, blue = 2000 m, green = 3000 m..... 91

Figure 4.5 HYPSLIT forward trajectory model results at 500, 1000, and 2000 m elevations starting over hotspot in eastern Syria beginning July 14, 2010 and ending 72 hours later over Iraq, Iran, and Kuwait. Red = 500 m, blue = 2000 m, green = 3000 m..... 92

Figure 4.6 HYPSLIT forward trajectory model results at 500, 1000, and 2000 m elevations starting over hotspot in eastern Syria beginning March 22, 2011 and ending 96 hours later over Iraq, Iran, Persian Gulf, and Russia. Red = 500 m, blue = 2000 m, green = 3000 m..... 93

Figure 4.7 MODIS satellite data of the region prior to and during the May 2010 dust storm shows a dust plume originating in eastern Syria and following the same trajectories outlined by the forward and backward models over Iraq before reaching Kuwait (modified from <http://modis-atmos.gsfc.gov>)..... 94

Figure 4.8 World soil map showing high concentrations of calcite and gypsum in the soils of the hotspot (modified from FAO soil map). ..... 95

Figure 4.9 Top: General area of study, blue box highlights the region where the hotspots were located. Bottom: Decorrelation stretch of a clear MODIS subset image for both hotspots showing areas of high quartz (red) carbonates (cyan, blue). R = B32, G = B31, B = 29..... 100

Figure 4.10 General map of study area highlighting the two hotspots. The first hotspot is highlighted by a blue box, the second hotspot is highlighted by a red box (modified from GoogleEarth)..... 101

Figure 4.11 11 ASTER scenes were mosaicked to create a single dataset of the first hotspot (R=B14, G=B12, B=B10)..... 102

Figure 4.12 12 ASTER scenes were mosaicked to create a single dataset of the second hotspot (R=B14, G=B12, B=B10)..... 103

Figure 4.13 Decorrelation stretch of clear ASTER data highlights differences in surface lithology (Bands 14, 12, 10)..... 105

Figure 4.14 ASTER (ASTGTM) level 2 DEM data for the second hotspot. Counter lines were overlaid on the image to highlight changes in elevation to identify topographic flats that could emit dust..... 106

Figure 4.15 A. Unmixing of a clear ASTER image along the Kuwaiti-Saudi border. Areas in red have higher quartz content, whereas green areas have higher calcite content. B. Visible image of the same area (modified from GoogleEarth). ..... 108

Figure 4.16 A. Unmixing of a clear MODIS scene that contains both hotspots (separated by the Euphrates River in blue). Areas in red have high quartz content, whereas areas in green have high calcite content. B. Visible image of the same area (modified from GoogleEarth)..... 109

Figure 4.17 Unmixing of a dusty ASTER near the Kuwaiti-Saudi border showing calcite content. Brighter pixels have the highest calcite content whereas darker pixels have the lowest. Based on  $\Delta T$  investigations, the southern half of the image was determined to be dusty, whereas the northern half was relatively clear..... 114

Figure 4.18 Kaolinite unmixing results for the same dusty ASTER scene, showing higher kaolinite content in the dusty areas (south)..... 115

Figure 4.19 Unmixing results for the same dusty ASTER scene showed no quartz in the dusty areas, whereas some surficial quartz was identified in the clear upper half of the scene. .... 116

Figure 4.20 ASTER image deconvolution RMS results. Brighter pixels indicate high RMS values, darker pixels indicate low RMS values. .... 117

Figure 4.21 Unmixing of dusty MODIS scene from the May storm did not identify the May spectra as an end member. Instead, it identified calcite 20-45  $\mu\text{m}$  (blue) and quartz <10  $\mu\text{m}$  (red). Green = cloud tops. .... 118

Figure 4.22 MODIS spectral deconvolution RMS results. Brighter pixels indicate high RMS values, darker pixels indicate low RMS values. .... 119

Figure 4.23 Quartz, andesine, and kaolinite have absorption features that overlap. .... 121



Figure 4.24 The presence of Kaolinite can result in suppressing the spectral features of quartz, and consequently misdiagnose quartz with andesine..... 121

## LIST OF EQUATIONS

Equation 1: Kirchhoff's Law .....	31
-----------------------------------	----

## PREFACE

I would like to thank my adviser, Dr. Michael Ramsey, for his support, both financially and academically, and for putting up with me. Also, thank you to my committee members who endured several changes in plans and were extremely understanding and flexible, not to mention their valuable input and recommendations. I would also like to thank Dr. Christopher Hughes, Dr. Rachel Lee, Dr. Stephen Scheidt, and Kevin Reath for their invaluable help and support throughout this process. They never hesitated to help me, and for that I will always be indebted to them. I would like to thank Dr. Amy Wolfe for undertaking the huge task of creating the mineral powders that were essential to my work.

On a personal note, I would like to thank my friends, Ibraheem Aziz and Mona Zubair, for believing in me when at times I lost faith in myself. They both saw through me and gave me the strength to continue.

And last but not least, the biggest thank you goes to my mother, Salwa Al-Abdullah. She gave up her dream of pursuing her masters and PhD so that I would have an overall better life and a chance to reach bigger and better goals. She made me her priority, and because of that, I dedicate this work to her.

## 1.0 INTRODUCTION

Dust storms can create a number of associated health, economic, and environmental effects that increase with the increasing intensity of these storms (Edgell, 2006). Dust storms occur naturally and fluctuate in severity and intensity due to changes in global sediment availability, and wind intensity related to glacial and interglacial periods (Washington et al., 2003). However, anthropogenic factors, such as desertification, destabilization of topsoil, or changes in land use can also influence storms (Goudie and Middleton, 2006).

A great deal of interest had been expressed to studying eolian processes in general and dust storms in particular. Dust storms have far reaching impacts that extend to non-arid regions, such as northern Europe and Canada (Goudie, et al., 2006). Therefore, it is important to understand the processes that initiate, transport, and sustain dust storms, in addition to identifying source areas or dust hotspots. Remote sensing offers indispensable tools that allow for observing, gathering information, and characterizing dust storms.

Most dust-related studies have focused on atmospheric aerosol content, effects of aerosol on surface albedo or temperature, or direct laboratory analysis of dust particles collected from the field. This study, however, attempted to utilize thermal infrared (TIR) tools to accurately describe the dust content (particle size and mineral composition) of storms affecting Kuwait, and potentially establishes a link to areas that may be identified as dust sources affecting that region.

The thermal infrared (TIR) region is of great importance to surficial geologic research as the amount of energy emitted from minerals and rocks can be interpreted to reveal their properties. Although the TIR region spans the 3-50  $\mu\text{m}$  wavelengths, absorption and scattering by water vapor, carbon dioxide and ozone limit the amount of information available in that region. The exception is the 8 – 12  $\mu\text{m}$  region, where there is 80-90% transmission, and where silicate minerals have unique spectral features (Ramsey et al., 1999, King et al., 2004).

Dust samples collected from Kuwait for three different dust storms (May, July 2010, March 2011) were analyzed using CCSEM and XRD to obtain particle size distribution and mineral content. Spectral libraries of fine-grained (2.7-45  $\mu\text{m}$ ) mineral end members identified in the XRD analysis and other end members were created. This is significant, as most spectral libraries were created with particle sizes  $> 60 \mu\text{m}$ . Ramsey and Christensen (1998) have concluded that using appropriate particle size end members when performing spectral deconvolution is important, particularly below 63  $\mu\text{m}$ . Therefore, this fine-grained spectral library is an important addition to TIR studies, and will contribute to studies related to fine mineral.

After creating the fine-grained mineral spectral library, spectroscopic analyses were performed on all dust samples, and their results were validated using the known XRD results. Finally, spectra obtained from all three dust storms, in addition to the newly created spectral library, were used to unmix clear and dusty ASTER and MODIS TIR satellite data, to survey how accurate TIR satellite data can be in identifying mineral content and associated particle sizes in dust plumes.

The objectives of this dissertation were A) create a fine spectral library, as such library is currently unavailable and crucial in analyzing fine particles, B) assess the validity of spectral

deconvolution or unmixing of very fine particles, and C) assess TIR satellite data capabilities in identifying mineral content of dust plumes and their associated particle sizes.

## **2.0 DUST STORMS IN THE MIDDLE EAST: FORMATION, EXTENT, AND EFFECTS**

### **2.1 INTRODUCTION AND STUDY GOALS**

According to Kutiel and Furman (2003), dust storms can be classified into blowing dust: horizontal visibility is less than 11 km, dust storm: horizontal visibility is less than 1000 m, and sever dust storm: horizontal visibility is less than 200 m.

Each dust event can produce create a number of associated health, economic, and environmental effects that are positively correlated to the intensity of these storms (Edgell, 2006). Dust storms occur naturally and fluctuate in severity and intensity due to changes in global sediment availability and wind intensity related to glacial and interglacial periods (Washington et al., 2003). However, anthropogenic factors, such as desertification, destabilization of topsoil, or changes in land use can also influence storms (Goudie and Middleton, 2006).

This chapter will closely examine the factors that combine to create dust storms, from meteorological conditions to sub-particle properties. Furthermore, dust mineralogy will be discussed and the geologic processes that lead to the presence of dust hotspots. Finally, environmental, geologic, and health impacts of dust storms will also be discussed, to illustrate

the magnitude of this phenomena. The Arabian Peninsula in general, and Kuwait in particular will be the focus of this chapter.

## **2.2 DESCRIPTION OF STUDY AREA**

### **2.2.1 Regional Climate**

The Arabian Peninsula lies in a subtropical zone where the climate is controlled by descending cool dry air. Consequently, most of Arabia has low precipitation and an average annual rainfall of less than 100 mm (Edgell, 2006). Summer temperatures average 42-45°C in central Arabia and may exceed 50°C in the interior deserts. In contrast, winter temperatures can drop below freezing at night and early morning, although daytime temperatures generally remain in the 10-20°C range (Mohammad, 2008). The northern part of Arabia receives much of its rainfall during the winter as a result of middle to high-latitude westerly depressions whose tracks are governed by the subtropical jet stream (SJT). In contrast, the southern part of Arabia receives precipitation largely from summer monsoons (Fischer, 2004). Figure 2.1 shows average maximum, minimum, and rainfall amounts for Kuwait (Al-Sulaimi et al., 1997).

Further north, temperature extremes are less evident along the Mediterranean coast, although the interior parts of that region experience less moderate conditions. Precipitation ranges from 1000 mm along the coasts of Lebanon and Syria and decreases eastward, reaching only 250 mm in northern Jordan (Edgell, 2006). Dust storms occur throughout the year, with late spring and early summer being the peak. These storms occur as a result of low-pressure



systems moving eastward, creating a pressure gradient ahead of these systems and creating dust plumes known as Haboobs. They also occur when wind velocity increases as a result of rapid warming of desert surfaces in the late morning and early afternoon hours (Goudie and Middleton, 2006).

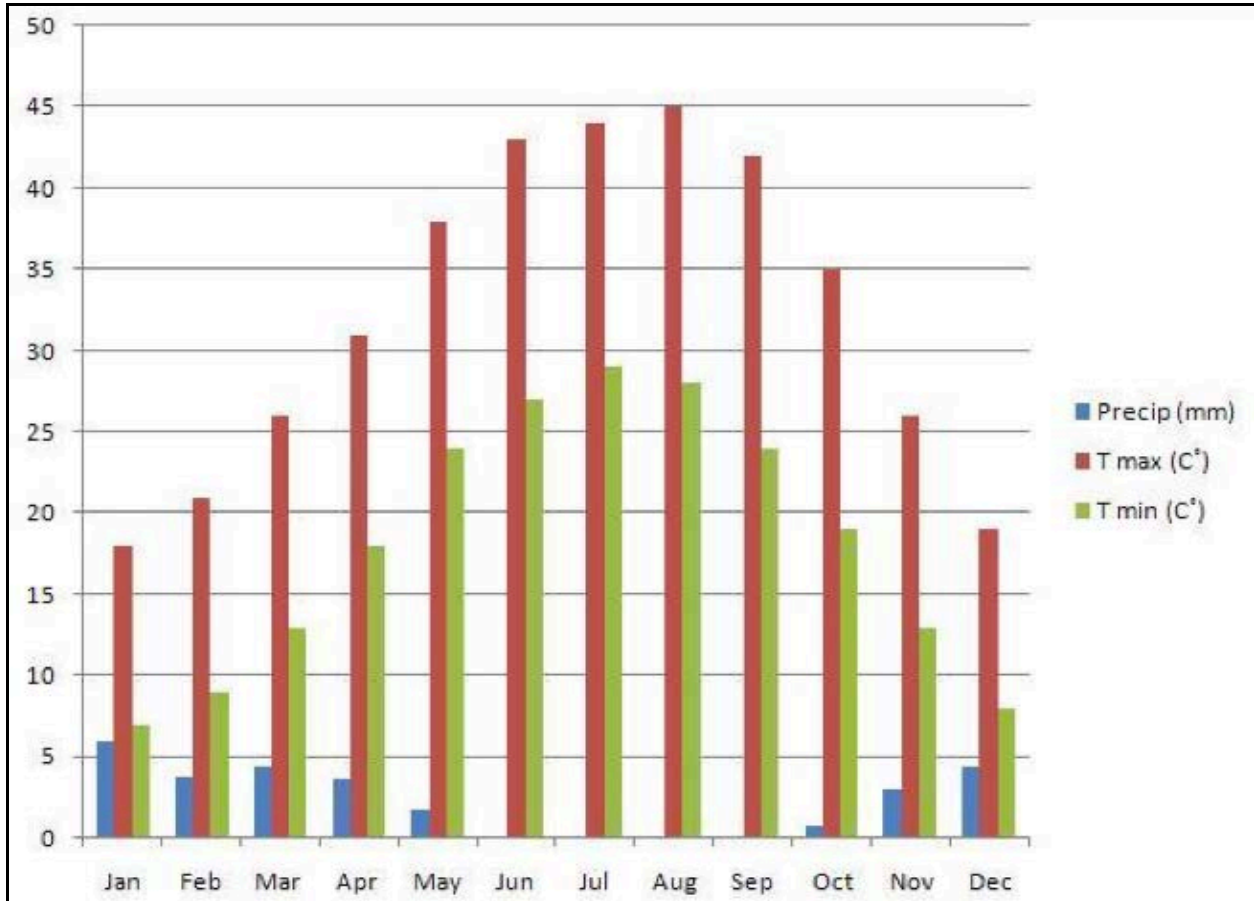


Figure 2.1 Monthly average temperature and precipitation in Kuwait (Al-Sulaimi et al., 1997).

### 2.2.2 Geology and Surface Deposits

Arabia formed during the Paleozoic, initially as a low-lying northeastern corner of Africa, with the shallow seaway of the Tethys reaching onto its northeastern margin (Edgell, 2006). Marine

sediments that were predominantly of shallow water origin were deposited in this gently subsiding seaway from Cambrian-Ordovician to the Early Tertiary, with sporadic periods of non-deposition occurring occasionally (Edgell, 2006). During the Oligocene, Arabia began to split away from Africa with great uplifts on either side of a fissure that developed into the Red Sea. Arabia then became a separate tectonic plate. Today, the Arabian Plate is moving northeast at rates now estimated from GPS measurements to be 25 mm/year for Oman or 15.7 mm/year for the southern Red Sea (Edgell, 2006). As a result of the Arabian Plate's northward movement and collision with the Eurasian Plate, the Iranian Plate has been under-ridden by the subduction of the Arabian Plate, causing the uplift of the Zagros and Taurus mountain ranges (Fig 2.2) (Edgell, 2006).

The study area covers most of the northern parts of the Arabian Peninsula, in addition to Iraq, Jordan, and Syria. This region can be divided by Dapples (1941) into four general regions: the coastal area, steppe and plateau, Euphrates valley, and the mountain and basin range of northern Iraq.

#### The Coastal Area:

Topographic highs that exceed 2100 m characterize this area. The mountains contain slightly folded strata of Jurassic, Cretaceous and lower Tertiary ages. These strata have been broken by a series of faults trending ENE. Approximately 130 km north of Damascus, few basaltic flows are exposed and broken by faulting. South and east of Damascus is a plateau region of steppes that is separated from the coastal area by a line that corresponds with the northern part of the divide between the watershed of the Euphrates River and streams of interior Arabia, with both regions forming a single plateau that rises gently 900 m to the south. This

plateau of interior drainage and saline depressions contains within it a section that is covered with basaltic flows of Pliocene and Pleistocene age. These flows extend westward to the Jordan valley, where it terminates by the faults described in the coastal area section (Dapples, 1941).

#### The Euphrates Valley:

This valley cuts through Miocene strata, where in some locations the valley is wide and in others the stream flows through narrow gorges. Along the entire width of the Euphrates numerous wadis enter as tributaries. These wadis are dry valleys throughout most of the year, except when subjected to sporadic floods caused by intense rainstorms (Dapples, 1941).

#### Upper Iraq:

The mountainous section of upper Iraq lies northeast of the Tigris River. This region has gently folded sandstones, conglomerates, and gypsum bed of Miocene and Pliocene ages. Locally basalt lavas cap the strata. Towards the east, strata of progressively older age, mainly Cretaceous and Jurassic, is exposed at the surface due to more intense folding, and the rocks are cut by numerous intrusions. The increase in folding causes a corresponding increase in relief (Dapples, 1941).

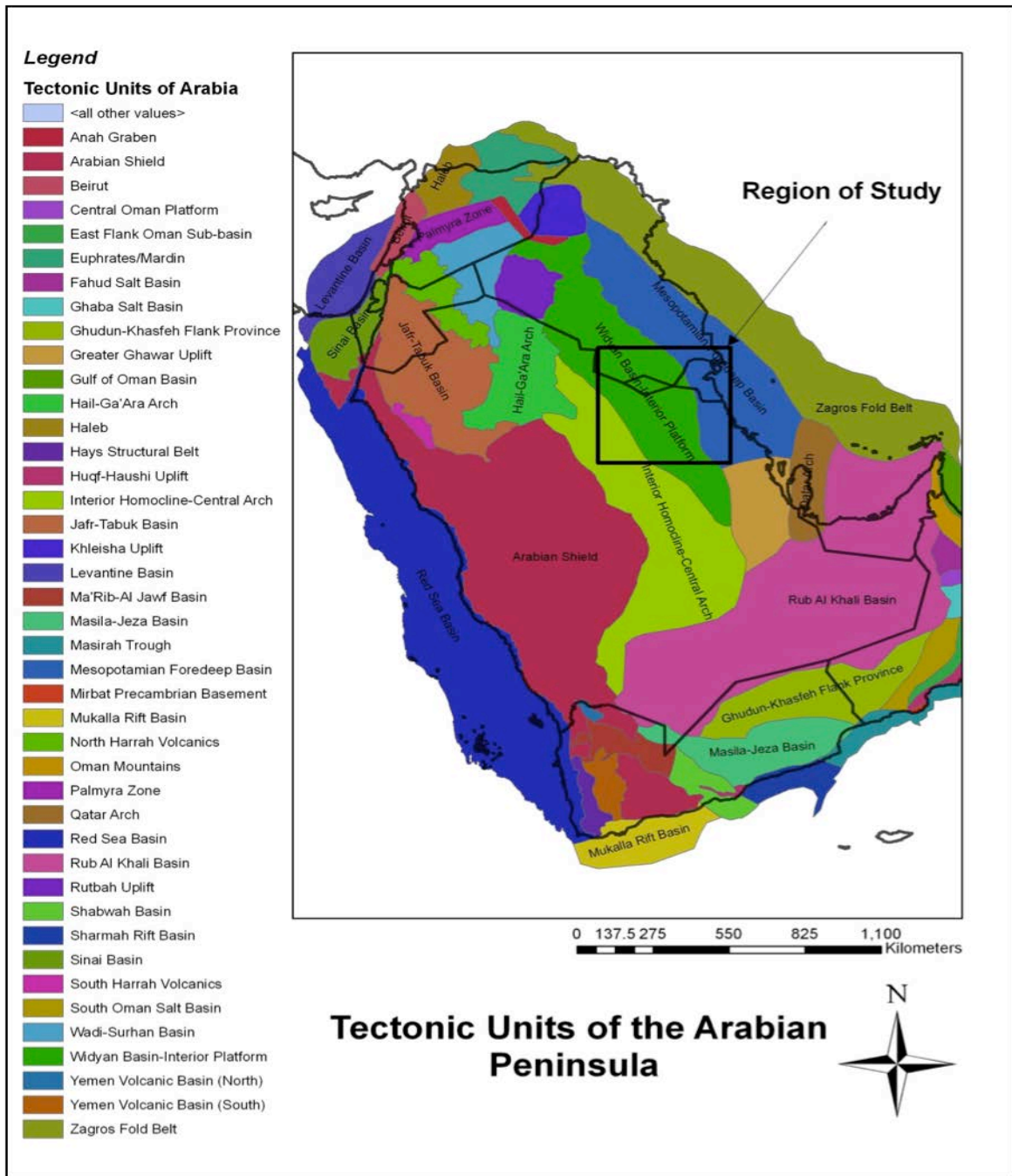


Figure 2.2 Tectonic and geologic map of the Arabian Peninsula (modified from USGS digital soils map of the world).

Dapples (1941) also classified surface deposits into six categories that include residual deposits, alluvial deposits (mainly sheet-wash deposits), residual deposits which have been

transported by running water and wind, deposits formed in evaporating basins (evaporite deposits), playa lake deposits, and eolian deposits. His classification was based on field observations and microscopic analysis.

#### Alluvial Deposits:

These widespread deposits are characterized by considerable irregularity in the state of decomposition of the rock fragments. In general, material of 0.4 mm and smaller, particularly in limestone, consists of the resistant products of decomposition, such as quartz and clay minerals. Particles of granule and coarser size consist of disintegrated rock fragments (Dapples, 1941).

#### Sheet-Wash Residual and Wind-driven Deposits:

These deposits have many of the characteristics of residual accumulations but they indicate that they have been transported and deposited in their present site by running water and resulting from sheet-wash. They contain pebbles that are angular to sub-angular in shape but the degree of angularity is less than that of residual deposits. They also contain fragments of material from different sources. The bulk of the material constituting these deposits is finely divided, and where pebbles are present, the grains of fine sand and silt dimensions are less decomposed than in the case of residual deposits. A few deposits show evidence of having been transported short distances by running water and later slightly re-sorted by wind. All samples obtained by Dapples (1941) are limestone and consist mainly of disintegrated fragments with smaller quantities of decomposed material. The pebbles present have rounded corners and edges and commonly have smooth surfaces, although some show the typical solution fluting observed in limestone pebbles of the residual deposits. None of the pebbles shows any indication of having been blasted by

wind-blown sand. The fine sizes consist of rounded or ellipsoidal-shaped grains of calcite and quartz and their surfaces are slightly pitted by sand blasting. Aggregates of quartz and calcareous clay are also abundant, but their abundance is inversely proportional to the density of the surface on the quartz grains. This is expected, as transportation increases the tendency for such aggregates to disintegrate.

#### Evaporite Deposits:

These deposits consist mainly of the residual products of limestone, which have been cemented by calcite into crusts. They appear to have formed by precipitation of salts by evaporation of standing water. The crusts have been broken up and their semi-rounded edges suggest transportation. The presence of a thick coating of calcite and the lack of clastic material on the upper surface of the crusts further supports the theory of deposition of salts from standing water. The deposits consist of finely divided quartz and clay, cemented with calcite and some selenite. The cementation is the result of the deposition of small crystals of calcite on the surfaces of particles of clastic material. The deposition of calcite appears to have formed from the top downward. This is indicated by the nature of the crusts, which consist of an upper zone of fine grained, dense travertine, 2 to 3 mm thick, which is sharply separated from the lower zone, an aggregate of clastic material embedded in clay and cemented with calcite. In the lower part, cementation is not thorough and when the crusts are wet, disintegration occurs. The clastic material consists of granules of flint, quartzite, granite, and trachyte. The fine material consists of grains of quartz and weathered feldspar. The size frequency cumulative curves of evaporite deposits are characterized by a variation in the size of the median diameter that ranges from 0.105 to 8.2 mm (Dapples, 1941).

#### Playa Lake Deposits:

These deposits consist mainly of the fine-grained detrital material, mostly quartz and feldspar with minor quantities of calcite and selenite. The individual grains are slightly rounded and moderately pitted by the sandblasting effect of winds when the playa lakes were dry. The detritus is distinguished by the fresh and undecomposed appearance of the mineral particles, especially if the deposit has been derived from crystalline rocks. Size frequency cumulative curves of playa deposits are steeply inclined and include approximately the same size groups. This is indicated by extremes in the median diameter from 0.073 to 0.35 mm, or a range from medium to very fine sand (Dapples, 1941).

#### Eolian Deposits:

These deposits are common and result from the transportation and depositional action of wind. They range from reddish to yellow-beige color. The red color is characteristic of much of the Nefud or sand area of northern Arabia. Most of the deposits were mono-mineralic. Although the general mineral is quartz, coarser sizes consist of limestone and dolomite fragments. The presence of the limonite stains and the calcite crystals suggests that the wind recently has not been an active transporting mechanism. All of the eolian deposits are uniform in the shape of the cumulative size frequency curves, which are steeply inclined and symmetrical, and closely resemble those of the playa deposits. The median diameter ranges from 0.088 to 0.31 mm and is commonly about 0.2 mm (Dapples, 1941).

Despite the diversity in the method of deposition of the sediments and the wide distribution of the localities identified by Dapples (1941), the deposits have common features. Some of these deposits may prove to have developed in a desert environment and will therefore be valuable in the recognition of ancient desert deposits. Except for the wind-transported materials, the sediments have coarse material of granule and pebble size, which consists of fresh or nearly undecomposed rock, but debris of sand grain size and smaller generally consists of clay minerals and quartz. A uniform gradation of undecomposed to completely decomposed material does not appear to exist. Instead, there is a sharp delineation between the decomposed materials of sand grain size and smaller, and the fresh rock of granule and pebble size (Dapples, 1941).

Deflation and accompanying deposition of eolian sediments are active, and wind-deposited materials are common. These deposits are found on the floors of wadis and the open desert. Some of the windblown deposits contain grains of mica, which are commonly removed either by abrasion or deflation from regions where active wind transportation prevails (Dapples, 1941, Edgell, 2006).

### **2.3 DUST STORMS**

Dust storms affect many regions in the world. They vary in extent and intensity from one region to another due to a number of variables that control dust storm formation and distance travelled. Africa and the Middle East are two of the world's largest dust aerosol emitters and experience such storms frequently (Fig. 2.3) (Washington et al., 2003). Kutiel et al. (2003) examined visibility reduction (below 11 km) spanning a period of 21 years from 1973 to 1993 to



characterize dust emission in the Middle East and North Africa. They concluded that the Arabian Peninsula and East Mediterranean regions experience considerably more dust storms than other regions, with the majority of these storms occurring during the summer months (June-Sept) and reducing visibility to less than 11 km for one-third of that season.

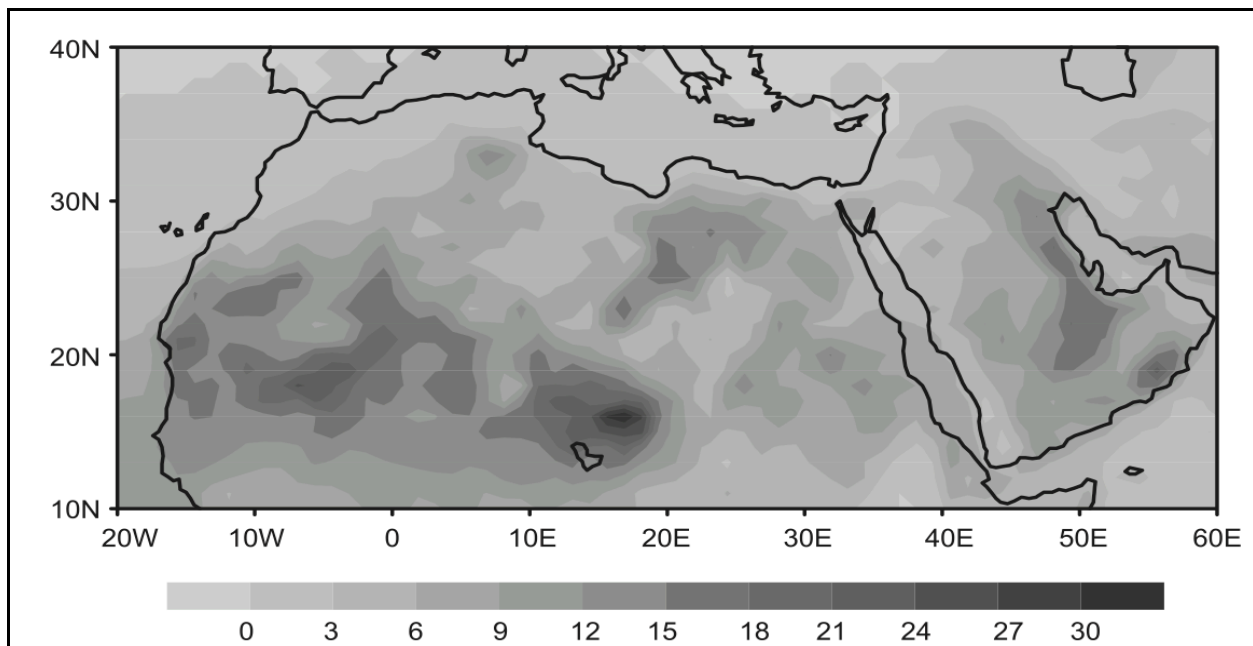


**Figure 2.3 TOMS Aerosol Index (AI) values identified Africa and the Middle East as the world's largest dust emitters (modified from Washington et al., 2003)**

Although many of the dust storms that affect the region originate locally, some can originate 100's to 1000's km away. A strong cold front that originated in the Western Sahara in March 1998 created a massive dust storm that travelled eastward and affected areas as far as Jordan within 48 hours (Goudie and Middleton, 2006). The convection associated with these cold fronts creates downdrafts or downbursts that result in a type of dust storm referred to as haboob, where dust walls can be as high as 2 km (Fig. 2.4) and lasting anywhere from 30 minutes to several hours (Miller et al., 2008).



**Figure 2.4** Haboobs form ahead of cold fronts and can reach as high as 2 km, like this storm affecting the suburb of Al-Mangaf in Kuwait on March 25, 2011 (Kuwait International Airport, [www.dgca.gov.kw](http://www.dgca.gov.kw)).

### **2.3.1 Formation of Dust Storms**

Although dust storms are frequently associated with arid and semi arid regions, almost every region on earth experiences a form of dust storm at any given time. Dust storms are also known to occur on other planets, such as Mars (Goudie and Middleton, 2006). Eolian dust accounts for most of the dust found in the atmosphere. The Sahara desert contributes 2 to  $3.3 \times 10^8$  tons/year, or roughly 40-66% of global dust (Kutiel et al, 2003). Formation of dust storms is a complex process that involves a host of geologic, environmental, and meteorological processes. The following sections discuss key elements in dust storm formation and the various mechanisms that operate within each.

### **2.3.1.1 Dust Source**

The availability of loose and fragmented material that can be dislodged by wind and carried over a distance is important in dust storm formation. Although there is a debate over the upper grain size limit that defines a dust particle, the general consensus is centered on the silt/sand boundary of smaller than 63  $\mu\text{m}$  (Goudie and Middleton, 2006; Wentworth, 1922). Thus dust can be defined as wind blown silt and clay particles that range from 2 to 50  $\mu\text{m}$  (Edgell, 2006). The availability of mobilized and erodible silt and clay particle is therefore key in dust storm formation.

Reheis (2006) argues that alluvial plains and playas are the main sources of dust in the southwestern region of the United States due to their clay and silt content. Transitional regions between wet/semi-arid and arid environments with high levels of runoff from elevated terrains (e.g. the plateau of eastern Syria) form depositional environments that act as dust sources (Gillette, 1999; Edgell, 2006). Coudé-Gaussen (1987) identified the following surfaces as dust producing surfaces in the Sahara: internally drained dried out salt lakes, floodplains of large rivers, and silt-rich wadi sediments.

One of the mechanisms for producing silt is surface abrasion, and it can be caused by particles blasting and scraping rock surfaces, causing the release of grain surface coating and further reworking those particles (Bullard et al., 2004). In the central Sahara, the erosion of diatomite, a soft and friable siliceous sedimentary deposit, has been identified as a major source for dust (Giles, 2005). Other mechanisms include frost action, salt attack, reactivation of stable sand dunes, and chemical weathering (Goudie and Middleton, 2006).

### **2.3.1.2 Threshold Velocity**

Eolian particles have three types of movement: creeping, saltation, and suspension. Large particles ( $>500\ \mu\text{m}$ ) exhibit a creeping or rolling motion due to their size. Saltation or hopping is associated with intermediate particles ( $50\text{-}500\ \mu\text{m}$ ), whereas finer particles are suspended in the atmosphere (Bagnold, 1941; Goudie and Middleton, 2006). In addition to particle size, other factors determine what type of movement a particle will exhibit. These include moisture content, surface cover, particle shape, and degree of cementation (Gillette, 1999; Zender et al., 2002). Zender et al. (2002) determined the threshold velocity; the minimum wind speed required to overcome surface friction and initiate deflation. It is also the wind speed at which erosion occurs. This value is measured in meters per second (m/s) and varies by surface properties, resulting in great uncertainty and predictability challenges (Gillette, 1999; Goudie and Middleton, 2006). An attempt to overcome this hurdle was made by Gillette et al. (1980) through the use of a special wind tunnel that can replicate field conditions and estimate the minimum threshold velocity values for each soil type. They observed an inverse relationship between threshold velocity values and the level of surface disturbance. Table 2.1 shows the different threshold values for types of surfaces found in the United States southwestern region. Similar values are shown in table 2.2 and were derived from Edgell (2006) for deserts in the Arabian Peninsula.

The effects of surface and soil disturbance were examined by Belnap et al. (1998), and they concluded that an increase in surface disturbance causes a decrease in the threshold velocity value and renders surfaces more vulnerable to wind erosion. Disturbed playas were the most susceptible to wind erosion because they lacked larger rock particles that can increase surface

roughness and decrease erosion (Gillette et al., 1988). Whereas increasing surface roughness causes an increase in threshold velocity, it can also increase drag coefficient, leading to higher wind friction and more dust emitted into the atmosphere (Gillette et al., 1988; Goudie and Middleton, 2006).

Kutiel et al. (2003) found a positive correlation between wind velocity and amount of dust suspended in the atmosphere. They also noted a negative relationship between particle size and amount of suspended dust. A similarly negative relationship exists between distance travelled and particle size, where particles travelling over a long distance have an average diameter of 5  $\mu\text{m}$  (Miller et al., 2008). Although larger particles have higher threshold velocities, very fine particles exhibit particle cohesion, making them similarly as hard to erode (Goudie and Middleton, 2006).

**Table 2.1 Difference threshold velocities for surfaces in the United States SW region (Goudie and Middleton, 2006)**

Surface type	Threshold Speed (m/s)
Disturbed soil	5.1
Sand dunes	7.8
Alluvial and eolian sand deposits	8.0
Disturbed playa soils	8.1
Playa centers	15
Desert pavement	> 16.0

**Table 2.2 Different threshold velocities for desert surfaces (Edgell, 2006)**

Surface type	Threshold Speed (m/s)
Medium to course sand	4.47-6.71
Poorly developed desert pavement	8.94
Fines, desert flats	8.94-11.17
Alluvial fans, sabkhahs	13.41-15.65
Well-developed desert pavement	17.88

### **2.3.1.3 Particle Deposition**

Deposition of dust particles from the atmosphere can either occur due to gravitational forces (dry deposition) or as a result of mixing with any form of precipitation within or below a cloud (wet deposition) (Zender et al., 2002). Dry deposition is the dominant mechanism in the study region, as the height of dust storm activity is associated with the dry summer months (Goudie and Middleton, 2006). Estimating the amount of particle deposition is easier with wet deposition, but can also be performed under dry deposition conditions through the use of numerical equations that estimate the rate of particle settling (Engelstaedter, et al., 2006).

### **2.3.2 Dust Composition**

The mineralogical composition of dust storms varies from one region to another, and is a function of the source area and the storm path. The most common component of dust globally is silica (59%), with quartz forming the majority of that component (Goudie and Middleton, 2006). Other major elements include  $\text{CaCO}_3$ ,  $\text{Al}_2\text{O}_2$ ,  $\text{Fe}_2\text{O}_3$ , and organics (Goudie and Middleton,

2006). Alastuey et al. (2005) identified three main clay minerals (palygorskite, illite, kaolinite) in dust plumes affecting the Canary Islands and concluded that they represent different source areas in Africa. The study area's (Arabian Peninsula) prevailing wind direction is north to northwesterly, and consequently, the source areas of most of the dust storms are of that direction (Al-Awadhi, 2005).

Quartz and calcite are the main minerals found in dust near Be'er Sheva, Israel, with smaller amounts of dolomite, feldspar and kaolinite (Erell et al., 1999). A study by Engelbrecht et al. (2009) examined the mineralogy of different dust samples collected throughout the Middle East on U.S. military bases. They concluded that samples collected from Kuwait and Iraq had large amounts of calcite (33-48%), followed by quartz (27-54%), and feldspar (21%). Smaller amounts of chlorite and clay minerals were also found, and these included palygorskite, illite-montmorillonite, and kaolinite (Fig. 2.5). Samples collected from areas close to Baghdad also included gypsum and mica. They concluded that the source of these storms is the salt pans and wadis along the border between Turkey and Syria.

### **2.3.3 Dust Storm Impact**

#### **2.3.3.1 Geologic Impact**

The processes of particle entrainment, transport, and deposition can affect and shape eolian environments in many ways. However, the single most important and critical process is erosion (Goudi et al., 2006). Erosion is initiated when the threshold velocity value is reached or exceeded (Goudie and Middleton, 2006), thus allowing particles to be removed and transported. In eolian environments where vegetation cover is minimal, precipitation is low, and evapotranspiration is high (Edgell, 2006), erosion is a dominant force (McFadden et al., 1987).

In addition to upward migration of gravel, erosion of fines is believed to be a main contributor to desert pavement formation (McFadden et al., 1987). Desert or stone pavement is an armor of closely packed, angular to sub rounded gravel that overlay a layer of fines (Goudie and Middleton, 2006; McFadden et al., 1987; Williams et al., 1994). The gravel moves laterally by mechanical weathering into topographic lows (McFadden et al., 1987), where clast cementation occurs using quartz-rich windblown dust (Wells et al., 1985). The continuous flux of dust supply is key to maintaining and developing desert pavement (McFadden et al., 1987). Desert pavement can act as dust traps that capture eolian material (Haff et al., 1996) or a dust source when disturbed by anthropogenic processes (William et al., 1994).

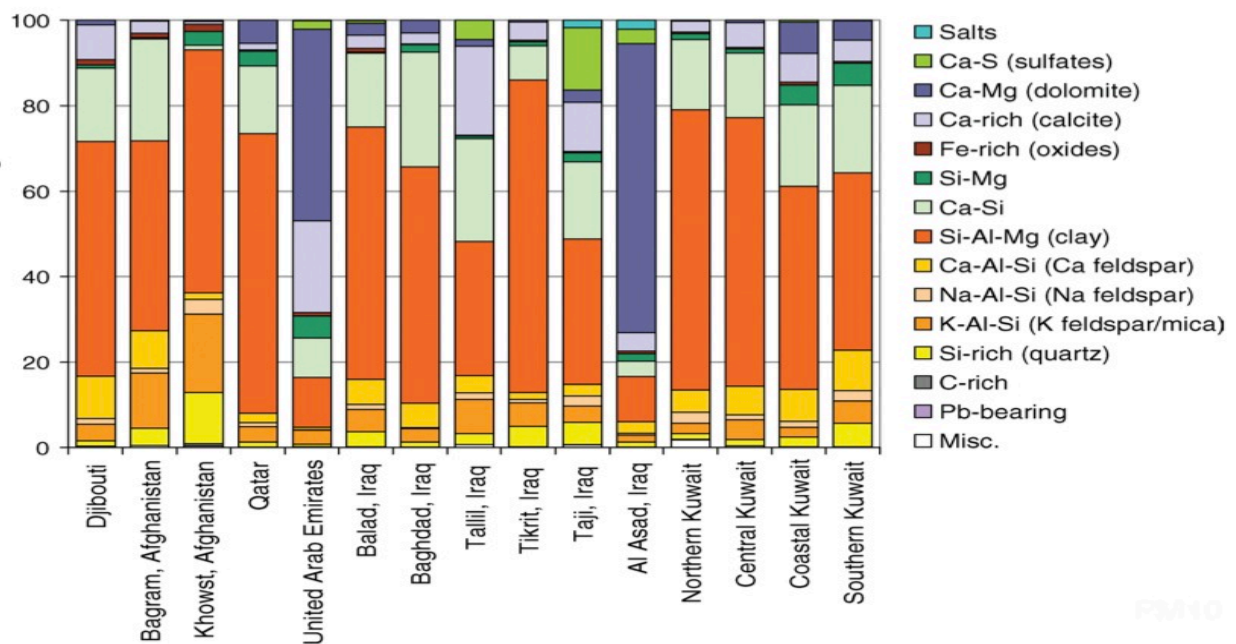


**Figure 2.5** Composition of various dust samples collected throughout the Middle East showing variation in dust content within a relatively small area like Kuwait (Engelbrecht et al., 2009). Higher levels of carbonates found in Iraq and in dust storms affecting Kuwait indicate a source near Iraq.

Although deposition of dust replenishes desert pavement, it can lead to serious consequences to source areas. The preferential removal of fine particles by dust storms leads to



gradual coarsening and loss of nutrients for topsoil, as organic matter and nutrients are held by fine particles (Goudie and Middleton, 2006). Removal of topsoil by wind erosion can result in removal of all organic carbon and creation of barren soils that cannot sustain agricultural activity (Yan et al., 2005). Yaalon et al. (1973) argued that the presence of significant amounts of quartz in soils with no quartz substrates is indicative of soil contamination by dust and that the effects of these storms are not only confined to areas adjacent to desert margins.

In addition to changing the properties of soils, dust storms can also shape the landscape. Wind abrasion by suspended sand on ridges of cohesive material can create yardangs, where sharp edges are oriented parallel to prevailing wind direction (Edgell, 2006). Yardangs can range in height from few centimeters to tens of meters (Goudie and Middleton, 2006). In northern Saudi Arabia, 40 m high yardangs have formed in the Cambrian Sandstones as a result of wind erosion (Goudie and Middleton, 2006). The island Kingdom of Bahrain has smaller yardangs that range from 4 to 6 m in height and are also believed to have been created by wind erosion. Yardangs are also common in the western desert of Egypt, southeastern Iran, eastern Syria, and the western Sahara (Edgell, 2006).

### **2.3.3.2 Environmental Impact**

Not only do dust storms play a major role in the global movement of sediment, but also transport several key elements that are essential for oceanic ecosystems. The availability of soluble ferric iron is critical for phytoplankton production (Jickells et al., 2005), and many areas such as the Mediterranean Sea (Antoine et al., 2006) and the Caribbean Sea depend on dust storms to supply and fertilize the upper layers of oceans (Donaghay et al., 1991). Jickells et al. (2005) examined the role dust plays in supplying oceans with soluble iron. They concluded that sustaining phytoplanktonic primary production and CO<sub>2</sub> uptake in oceans identified as having high nutrient

and low chlorophyll, such as the Southern Ocean and the northwestern subarctic Pacific, depends on atmospheric input of soluble iron from dust storms. And whereas changes in iron supply affect primary production and species composition in these areas, they concluded that similar changes in tropical and subtropical regions would only result in changes in nitrogen fixation. Areas such as the North and South Atlantic and the Mediterranean rely on Saharan dust storms to supply iron and phosphorous, two key elements in promoting nitrogen fixation and oceanic productivity (Goudie and Middleton, 2006, Mills et al., 2004). Dust storms from other areas, such as Arabia, supply the Persian Gulf with essential micronutrients (Subba Row et al., 1999) and may also initiate algal bloom (red tides) events (Banzon et al., 2004).

The effects of the Saharan dust are more evident in the Central Amazon Basin (CAB), where nutrient supply by rivers is limited. Swap et al. (1992) examined the effects of Saharan dust storms on the CAB and concluded that synoptic scale weather systems that coincide with Saharan dust plumes inject dust into the CAB by means of disturbing conditions in the 850 to 700 mb atmospheric layer where Saharan dust is transported across the Atlantic Ocean. Others noted that higher dissolved iron concentrations ( $> 1$  nM) were detected in oceanic areas below dust plumes (Maher et al., 2010, Sarthou et al., 2003).

In addition to supplying oceanic systems with vital nutrients, dust storms can disrupt the radiation budget's balance and consequently influence climate through a phenomena known as radiative forcing (Goudie and Middleton, 2006, Scheidt, 2009). Atmospheric dust can scatter and absorb both incoming short wave and outgoing long wave solar radiation. Absorption results in atmospheric warming, whereas scattering produces cooling beneath the dust plume (Maher et al., 2010). The relationship between dust plumes and radiative forcing is a complex and not very well understood one. However, optical properties (particle size, shape and mineral

composition) are key factors in influencing absorption or scattering (Maher et al., 2010). Darker particles tend to favor absorption whereas brighter particles favor scattering (Goudie and Middleton, 2006). The presence of iron oxides, either as free particles or as coatings on quartz grains or iron oxide-clay aggregates, may result in an increase in absorbing potential at shorter wavelengths (Maher et al., 2010, Sokolik et al., 1999). Changes in radiative forcing not only influence temperature but also cloud formation through promotion or suppression of nucleation of precipitation particles within clouds (Kim et al., 2004), and that can also influence the moisture content and consequently the albedo of the underlying surface (Nicholson, 2000).

### **2.3.3.3 Health Impact**

The barren nature of deserts is misleading and conceals the fact that desert soils are abound with different species of bacteria, fungi, and viruses (Griffin, 2007). Dust storms act as carriers, where microorganisms attached to aerosol particles can be transported and later deposited hundreds to thousands of kilometers away from their source. Fungi have an advantage over other microorganisms due to their ability to produce spores, as spores enhance survival during transport. There is not sufficient scientific data related to long range viral transmission (Griffin, 2007, Dufrene, 2000).

A study by Lyles et al. (2005) on U.S. military personnel in Kuwait identified 147 bacterial colony forming units (CFU) through chromatographic analysis of fatty acid methyl esters and 16s rRNA gene sequencing in settled dust (Table 2.3). Their findings included five viable isolates of *Neisseria meningitidis*, the primary meningitis-causing bacteria. Other studies related to deployed military personnel in the Middle East have reported found respiratory-related

illnesses in 69.1% of personnel. These included pneumonia and respiratory stress (Griffin, 2007, Sanders et al., 2005).

**Table 2.3 Lyles et al. (2005) identified 147 bacterial colony forming units (CFU) on military personnel in Kuwait.**

Bacterial genus/ genera	Fungal genera	Location
Arthrobacter, Bacillus,	Alternaria, Cryptococcus,	Kuwait, Middle East
Cryptococcus, Flavimonas,	Mortierella, Penicillium,	
Kurthia, Neisseria,	Phoma, Rhodotorula,	
Paenibacillus, Pseudomonas,	Stemphylium	
Ralstonia, Staphylococcus		

The outbreaks of foot-and-mouth disease in Korea and Japan are believed to have occurred following Gobi/Takla dust events (Griffin, 2007, Joo et al., 2002), whereas Griffin et al. (2001) hypothesized that similar outbreaks of the disease in Europe may have been the result of long-range transmission of the virus with African dust over the Mediterranean and into Europe.

Other health impacts include abrasion of lung tissue caused by prolonged inhalation of dust particles. This can cause an increase in asthma and allergy prevalence (Griffin et al., 2004), and may lead to cellular membrane and DNA damage (Athar et al., 1998).

## 2.4 MEASUREING DUST

### 2.4.1 Total Ozone Mapping Spectrometer (TOMS)

The Total Ozone Mapping Spectrometer (TOMS) is an instrument that flew on board the Nimbus satellite from 1978 to 1994, and later flew on the Russian satellite Meteor-3 from 1994 to 2000 (Engelstaedter et al., 2007, Chiapello et al., 2005). It measured global ozone using changes in albedo derived from incoming solar radiation vs. backscattered ultraviolet (UV) radiation received at the sensor (Goudie and Middleton, 2006, Engelstaedter et al., 2007). Similarly, TOMS was able to measure global atmospheric aerosols using the spectral difference between two UV channels (340 nm and 380 nm), resulting in a semi-quantitative numeric Aerosol Index (AI) denoting the amount of suspended aerosols in a given area (Goudie, 2008, Engelstaedter et al., 2007). Areas with a long-term mean AI value equal to or higher than 0.5 were defined as a hotspot (Engelstaedter et al., 2007). A world map of annual mean AI values from TOMS observations (Fig 2.6) identified the Sahara region as having the highest AI values and therefore the highest atmospheric aerosol content, followed by the southern Arabian Peninsula, southwest Asia, and the Taklamakan Desert in China (Washington et al., 2003).

The AI observations are in general agreement with most ground-based aerosol observations (Washington et al., 2003). However, discrepancies between the two exist in a number of regions. The TOMS data assigns the southeastern area of Saudi Arabia an AI value higher than 2.1, making it the second most intense dust source in the world (Washington et al., 2003), whereas it does not highlight Kuwait or Iraq as being equally as important as dust emitters, despite ground observation data that indicate both areas have a higher annual mean number of dusty days compared to southeastern Saudi Arabia (Goudi et al., 2006, Washington et

al., 2003). Similar discrepancies can be found for the Great Plains region in the United States, where TOMS data did not highlight that region as a hotspot despite ground observation and meteorological data that indicate the contrary. Washington et al. (2003) suggests that this discrepancy may have been the result of dust storms occurring at low levels that may not be detected by TOMS, especially during events that cause convective modification of the boundary layer and creates strong wind at lower levels.

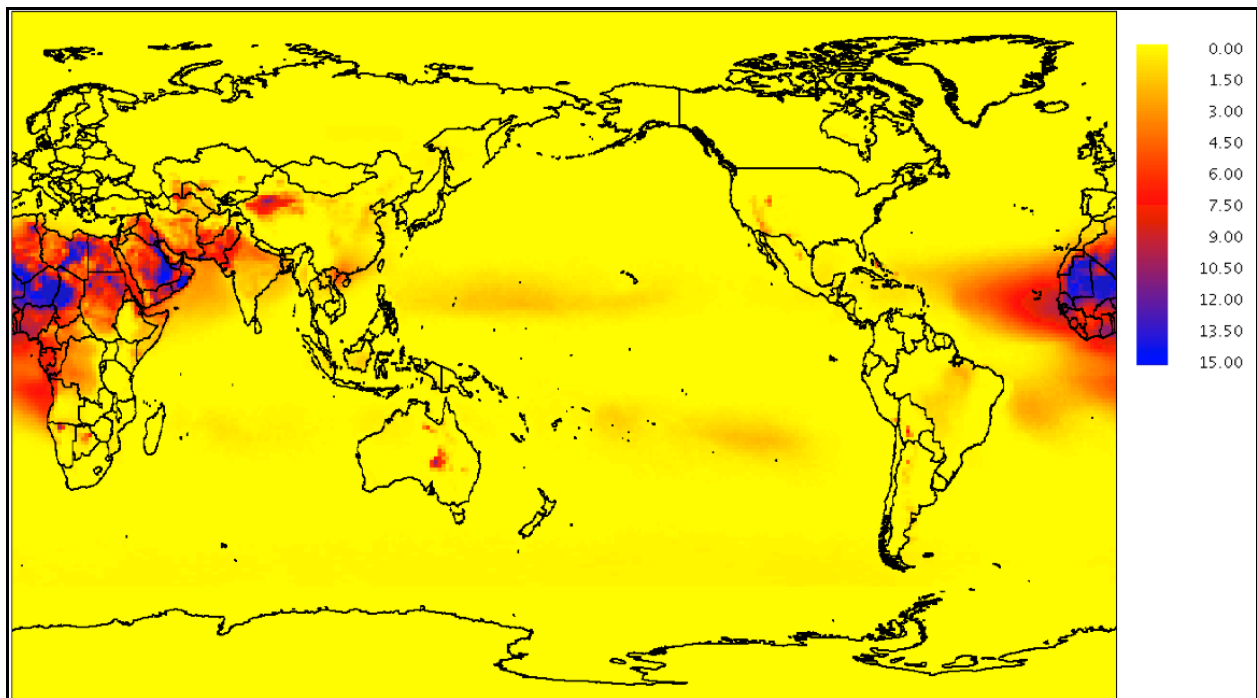


**Figure 2.6 Annual mean AI map based on TOMS observations. Much of the Middle East and Northern Africa have values higher than 1.50, indicating higher levels of aerosols (Engelstaedter et al., 2007).**

### **2.4.2 Atmospheric Infrared Sounder (AIRS)**

The Atmospheric Infrared Sounder (AIRS) is an atmospheric satellite sounder instrument launched in 2002 by the National Aeronautics and Space Administration (NASA) onboard the Aqua satellite. AIRS measures terrestrial and atmospheric upwelling radiance with 2378 channels that range from 3.8 to 15.3  $\mu\text{m}$  (Strow et al., 2003, Bhattacharjee et al., 2007), and its primary mission is to measure sea surface temperature, land surface emissivity, and abundance of minor gases for meteorological purposes (Strow et al., 2003). AIRS has the ability to detect infrared signatures of silicate aerosols in the 9-11  $\mu\text{m}$  region (Chahine et al., 2006).

Attempts to utilize AIRS in aerosol dust studies have been made with varying degrees of success. Pierangelo et al. (2004) were able to retrieve the optical depth and altitude of mineral dust by performing a sensitivity study and using a high-resolution radiative transfer code. AIRS uses water vapor, ozone and temperature profiles, in addition to other surface parameters to compute radiance under dusty conditions. Because the sea surface emissivity is well characterized and will not cause errors arising from dust absorption being confused with surface emissivity features (DeSouza et al., 2006), AIRS can only accurately study dust plumes over oceans, resulting in a major drawback and excluding major dust hotspots, such as the Sahara, from being studied.

## **2.5 SUMMARY**

The Middle East region is prone to the geologic, environmental, health, and economic effects of dust storms. Elements necessary for dust storm formation include a source area, overcoming

threshold velocity, and dust deposition. Although silicates dominate global dust content, dust storms affecting Kuwait have higher calcite to silica ratio. This is attributed to their source areas in eastern Syria and western Iraq. Current models that measure dust content only examine aerosol thickness and height and do not provide information about dust composition or mineralogy.



### 3.0 THERMAL INFRARED SPECTROSCOPY OF SILICATE DUST

#### 3.1 INTRODUCTION

The thermal infrared (TIR) region is of great importance to surficial geologic research as the amount of energy emitted from minerals and rocks can be interpreted to reveal their properties. Although the TIR region spans the 3-50  $\mu\text{m}$  wavelengths, absorption and scattering by water vapor, carbon dioxide and ozone limit the amount of information available in that region (Fig. 3.1). The exception is the 8 – 12  $\mu\text{m}$  region, where there is 80-90% transmission, and where silicate minerals have unique spectral features (Ramsey et al., 1999, King et al., 2004).

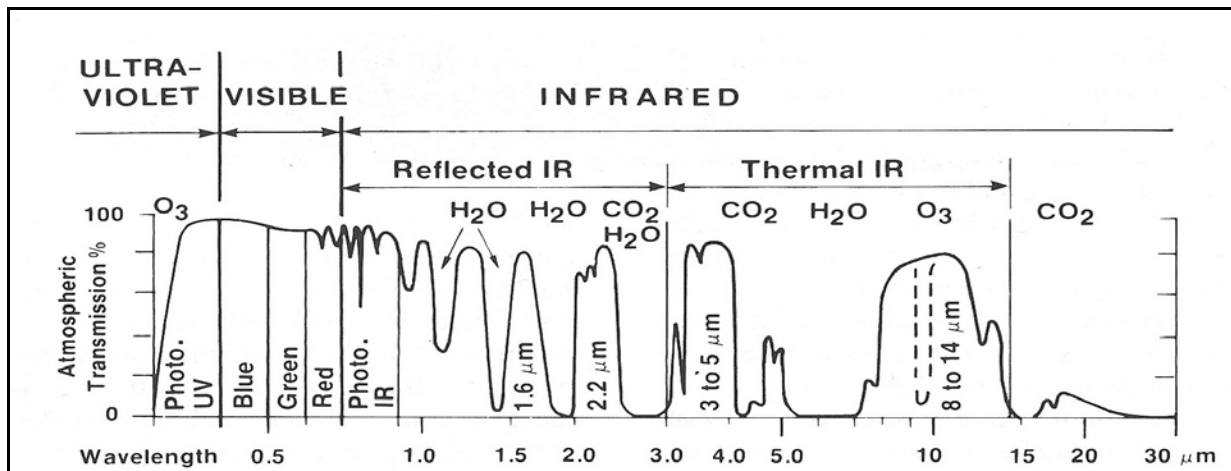


Figure 3.1 Much of the TIR region is obscured due to the presence of carbon dioxide, water, and ozone gases, thus limiting the usable window to the 8-12  $\mu\text{m}$  region (modified from Sabins, 1997).

Emittance from a surface is a function of temperature and emissivity, and therefore, the temperature of the surface must be known to determine its emissivity (Thomson et al., 1993). However, emissivity is also related to reflectance, as explained by Kirchhoff's law:

$$E = 1 - R,$$

**Equation 1: Kirchhoff's Law**

where  $E$  = emissivity and  $R$  = reflectance (Salisbury et al., 1992). This assumption holds true only under isothermal conditions (Salisbury et al., 1992, King et al., 2004).

In TIR spectroscopy, energy emitted from a surface and reaching a detector is assumed to contain information that can be interpreted to predict the mineralogy of that surface, and multi-mineral surfaces produce an emitted energy that is the sum of their combined energies relative to their relative abundances (Ramsey and Christensen, 1998, Thomson et al., 1993). Spectral deconvolution utilizes this theory and uses a least square linear fit to unmix spectral features and produce a model that closely resembles the mineral end members present in the spectrum (Ramsey and Christensen., 1998, King et al., 2004).

### **3.2 SILICATE THERMAL EMISSION SPECTRA**

Positive and negative vibrating ions that have a regular and repeating pattern form the building blocks of crystalline solids. These vibrating ions have quantized frequencies, and when they move out of phase with respect to one another, it is possible for energy to become absorbed at the wavelength corresponding to the motion's vibrational frequency (Hamilton, 2000). These absorption bands vary from one mineral to another, thus giving each mineral a unique spectral signature that can be used for mineral identification purposes (Fig 3.2). In silicate minerals, the

stretching and bending motions in the Si-O anions cause prominent absorption bands in thermal emission between 8 and 12  $\mu\text{m}$  (Ramsey et al., 1999). The structural arrangement of the anions and the location and composition of the cations determine radii, relative masses, distances, and angles between atoms and their bond strengths. These factors influence the frequencies, shapes, intensities, and number of features identified in a mineral's spectrum (Hamilton, 2000).

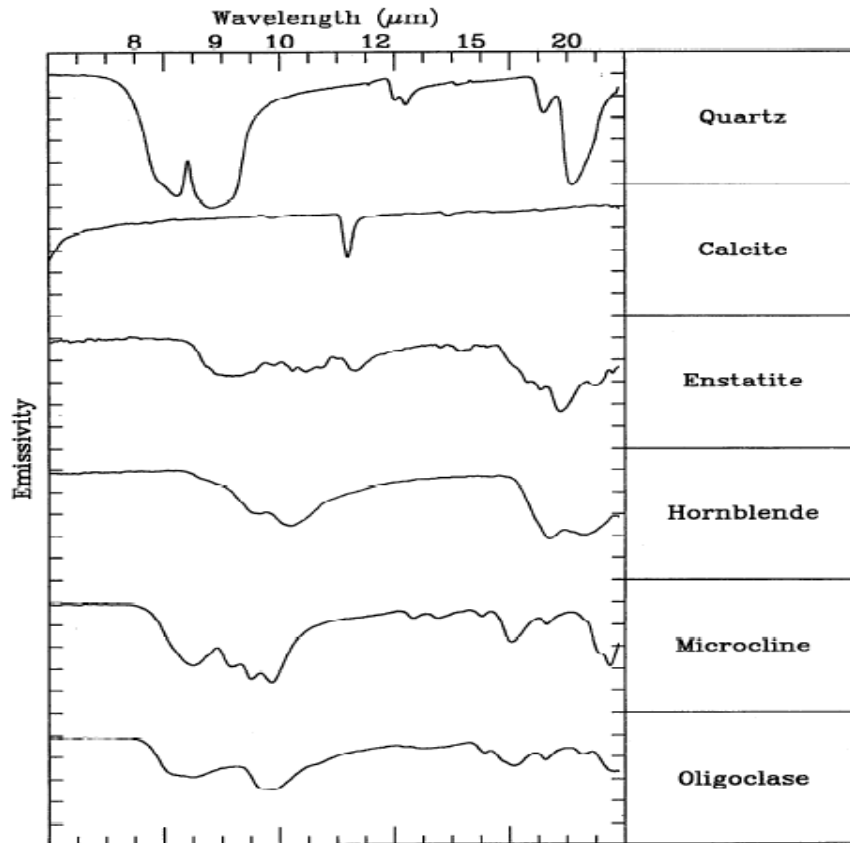


**Figure 3.2 Minerals have unique spectral features or signatures in the TIR region (modified from Ramsey and Christensen, 1998).**

### 3.3 PARTICLE SIZE EFFECT

Emission peaks and troughs, also referred to as maxima and minima, are the result of matter interaction with energy, causing reflection, transmission, or scattering of incident energy (Vincent et al., 1968, Salisbury et al., 1991). Reststrahlen peaks and transparency features are expressed as reflectance maxima (or emissivity minima), whereas Christiansen features are expressed as minima (or emissivity maxima) (Le Bras and Erard, 2003). The shape, intensity, and location of these features are determined by surface scattering and volume scattering (Le Bras et al., 2003, Kirkland et al., 2002). Smoother surfaces and large particles typically have high absorption and reflection coefficients, resulting in surface scattering being the dominant process and generating strong reststrahlen peaks. At longer wavelengths, a decrease in particle size causes an increase in scattering, resulting in volume scattering being the dominant process (Kirkland et al., 2002, Salisbury et al., 1991, Ramsey and Christensen, 1998). Whereas particle size decrease is the main contributor to volume scattering, an associated increase in porosity, also known as the cavity effect, is a secondary cause but to a lesser degree (Salisbury et al., 1991, Ramsey and Fink, 1999, Kirkland et al., 2002, Le Bras et al., 2003).

The prominence of reststrahlen peaks begins to decrease as volume scattering becomes more dominant as a result of particle size decreasing, resulting in reflection spectral peaks losing their spectral contrast whereas maintaining their general spectral features (Fig 3.3) (Le Bras et al., 2003). At longer wavelengths, a second set of reflectance peaks (Fig 3.4) called transparency features forms in the spectra of fine particles ( $< 75 \mu\text{m}$  in silicates) as a result of volume scattering (Le Bras et al., 2003).

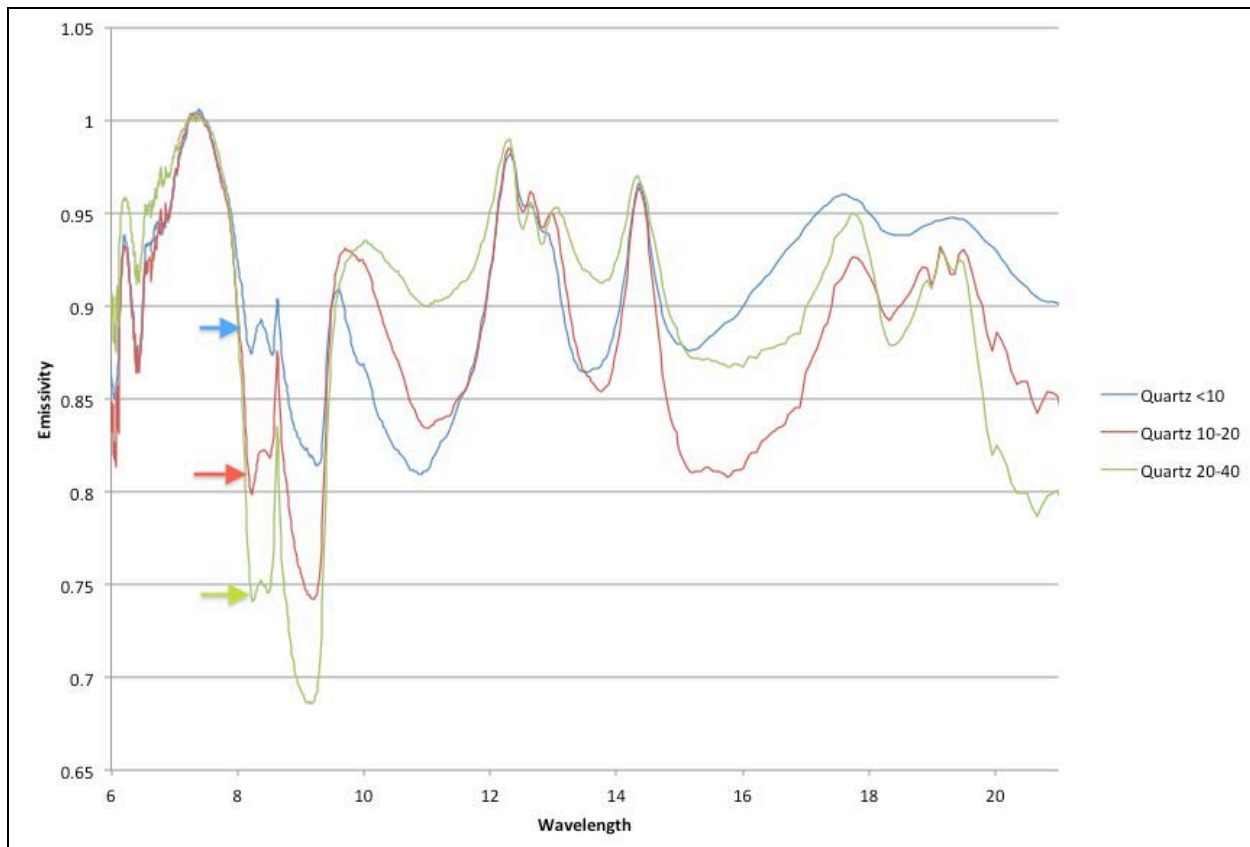


**Figure 3.3** Volume scattering dominates as particle size decreases, resulting in spectral features losing their contrast whereas maintaining their general shape. Arrows point to different quartz grain sizes and show the decrease in spectral contrast with decreasing particle size.

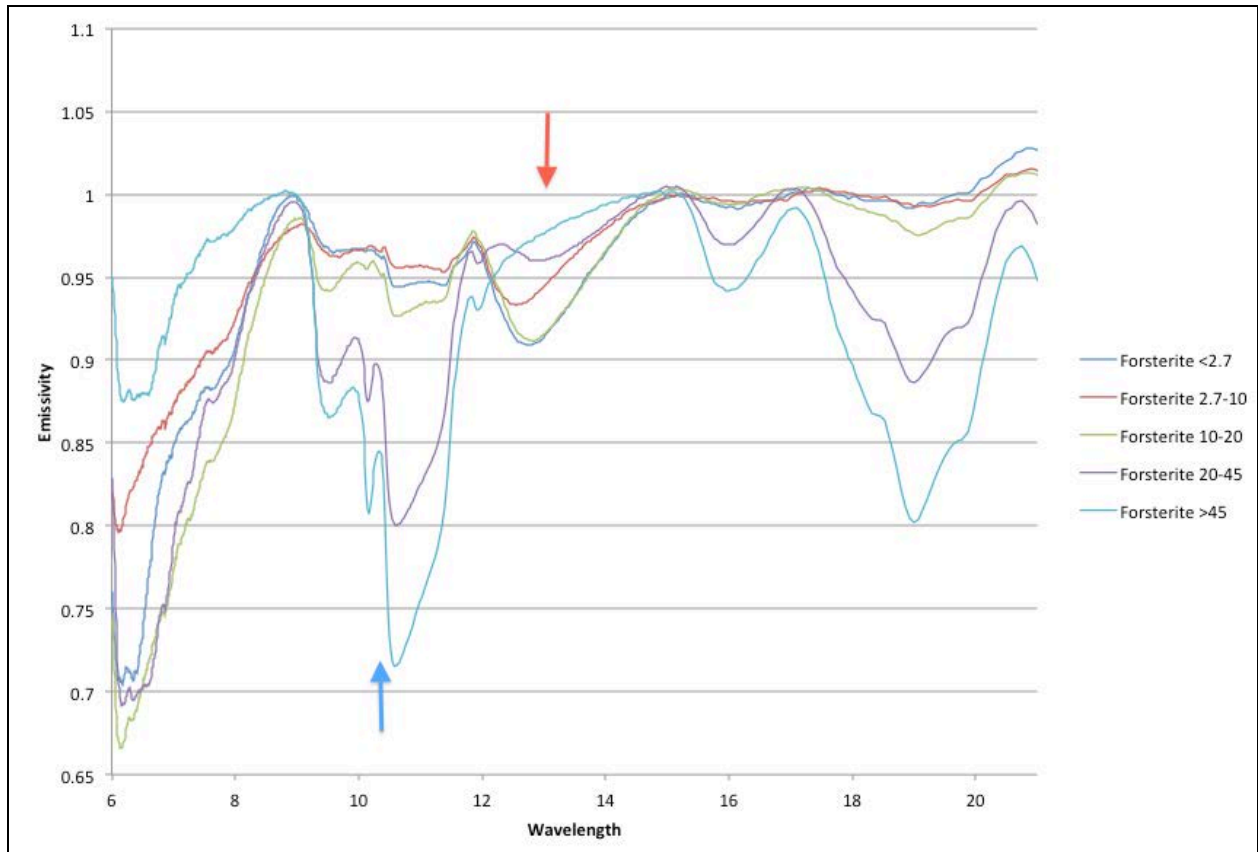


**Figure 3.4 Forsterite has emissivity lows (reststrahlen bands) at 10  $\mu\text{m}$  (red arrow). At longer wavelengths, a second set of emissivity lows, called transparency features, forms with finer particle sizes (blue arrow).**

Silicate particles that are smaller than 5  $\mu\text{m}$  become optically thin in the TIR region due to volume scattering, and therefore, a special spectral library of similar particle size must be used for mineral identification or linear unmixing (Salisbury et al., 1991, Ramsey and Christensen, 1998).

## 3.4 METHODOLOGY

### 3.4.1 Dust Collection

Goossens et al. (2008) examined five dust collection techniques that are commonly used to measure dry eolian deposits in arid and humid environments. These included the Marble Dust Collector (MDCO), Frisbee Method, Optical Counting on Glass Plates, Soil Surface Method, and the Capteur Pyramidal (CAPYR) Method.

The MDCO and Frisbee methods are best suited for humid climates, where rainfall causes dust deposits on the extremely smooth marbles to percolate and settle into the collection tray (Goossens et al. 2008). These methods are not suitable for the study area due to its extreme aridity and lack of precipitation.

The Optical Counting method uses a set of six 7.5 cm by 2.5 cm glass plates that are placed horizontally, allowing dust to settle on the plates. Once deposition is complete, each glass plate is covered by an identical clean plate, creating a thin section that is analyzed using a microscope (Goossens et al. 2008). Although fitting for microscopic analyses, the amount of collected dust is not sizable for analysis by a spectrometer or X-ray Diffraction (XRD), as these are the instruments of choice for analysis in this research.

The Soil Surface method measures dust directly at ground level and by taking samples of the sandy topsoil (Goossens et al. 2008). This presents a problem for this study, as one of the main objectives of this study is to examine individual dust storm events by collecting different uncontaminated samples from each storm. Measuring at ground level will introduce contamination by older deposits that are being resuspended and redeposited by wind. The same problem arises when taking topsoil samples, as they will contain particles from previous storms.

The final method is the CAPYR method. It uses a funnel-shaped sampler that is 40 cm high and has a 50 cm by 50 cm horizontal inlet opening. The sediment collected by the sampler is rinsed and stored in a flask. The weight of the dust and its deposition flux are both calculated by evaporating the water solution (Goossens et al. 2008). Due to time and resource constraints, a similar method was improvised using standard cone-styled No. 4 white paper filters. A standard plastic filter holder was mounted on a PVC pipe on the roof of a residential building in the Kuwait City suburb of Rumaithiya at an elevation of 13 m (Fig 3.5). The opening of the filter holder was positioned towards the northwest, as this is the prevailing direction of wind and sandstorms generally occur when gusty wind blows from the north-northwest. New filters were used for each storm, with collection periods ranging from 24 to 48 hours per filter at a rate of 1 filter per storm. Initial attempts to extract dust from the paper filters by tapping on the filters produced minuet amounts of dust ( $< 10$  mg). Removal of dust using water was not an option, as water molecules would interact with any clay minerals and consequently change the composition of the dust. Therefore, additional dust was collected by placing a clear glass cup on the building's rooftop near the filters, thus allowing suspended dust particles to settle and be collected and overcoming entrapment of dust particles within paper fibers. Each used filter was wrapped in aluminum sheets and placed in a plastic bag and transported to the United States for analysis. A total of three dust storm samples were collected. Table 3.1 lists and storms and their corresponding dates.





**Figure 3.5 A simplified version of the CAPYR method for collecting dust was used. A. General location of the filter, and B. close up of filter, showing a coating of dust.**

Additional mineral dust was created using mineral hand specimens. These included quartz, calcite, muscovite, forsterite, fayalite, andesine, and dolomite. Mineral hand specimens were ordered through Ward's Science, and it was crucial to order samples with no impurities in them, as this would eliminate the need for separating impurities from the pure mineral particles, resulting in time and resources savings. The process was carried out by Dr. Amy Wolfe at the US Environmental Protection Agency's (EPA) Ground Water and Ecosystems Restoration Division. It included crushing, milling and wet sieving each mineral sample to a particle size less than 10  $\mu\text{m}$  as outlined by Wolfe et al. (2007) (see Appendix A). A special 10  $\mu\text{m}$  stainless steel sieve was ordered from Precision Eforming. Quartz and andesine mineral dust samples with particle size less than 10  $\mu\text{m}$  were obtained from the Image Visualization and Infrared

Spectroscopy (IVIS) laboratory at the Department of Geology and Planetary Science. These IVIS dust samples were created by Dr. Michael Ramsey at Arizona State University (Ramsey and Christensen, 1998). Additional size fractions created included 20  $\mu\text{m}$ , 40  $\mu\text{m}$  and  $>45 \mu\text{m}$ .

**Table 3.1 Dates and times of dust storm samples collected for analysis.**

Date	Time of acquisition (UTM)	Time of acquisition (Local)
May 14 – May 16, 2010	12:00 – 13:00	15:00 – 16:00
July 19 – July 20, 2010	13:15 – 14:30	16:15 – 17:30
March 25 – March 26, 2011	14:00 – 20:00	17:00 – 23:00

### **3.4.2 XRD and SEM Analyses**

Prior to performing any TIR-related analysis on the dust storm samples and the mineral dust, it was essential that certain parameters be known. These included elemental composition and abundance, mineral composition and abundance, and particle size distribution. Scanning Electron Microscope (SEM) and X-ray Diffraction (XRD) are generally used to identify these parameters and were therefore performed at the University of Pittsburgh’s Swanson School of Engineering’s Material Micro-Characterization Laboratory (MMCL). The MMCL is equipped with two Philips X’pert diffractometers and a Philips XL-30 field emission SEM. Due to the author’s inexperience with the X’pert software used in the MMCL, and the relocation of the MMCL to a different floor during the analyses, the results of both analyses were deemed inconclusive and further verification was required.

The samples were referred to R J Lee Group, where Computer Controlled SEM (CCSEM) and XRD analyses were performed. The Group uses CCSEM and it has an advantage over conventional SEM whereby the process is automated, resulting in faster and more accurate results (Fig. 3.6). Quantitative XRD was performed on a portion of each unknown sample using the internal standard method. This method involves obtaining and x-raying a series of pure mineral standards of various known concentrations, each mixed with a known quantity of an internal standard (calcium fluoride in this case). From the XRD patterns obtained from this exercise, an analyst is able to plot a calibration curve of intensities versus concentration for each reflection associated with that particular phase. A series of calibration constants are calculated from the slope of each calibration curve. After obtaining k factors for the mineral phase to be quantified, the unknown specimen can be x-rayed under the same conditions. The resulting unknown pattern is then compared to the ICDD database to identify the crystalline phases present. The peaks of interest are located and peak area intensities are measured. The k factors are then used to calculate the percentage of the particular mineral component in the unknown sample. The use of several k factors associated with several peaks for a particular phase is optimal to obtain good quality results (See Appendix B). If two or more phases have peaks that overlap, underestimation of other phases or trace elements can occur, causing final results to not add up to 100%.

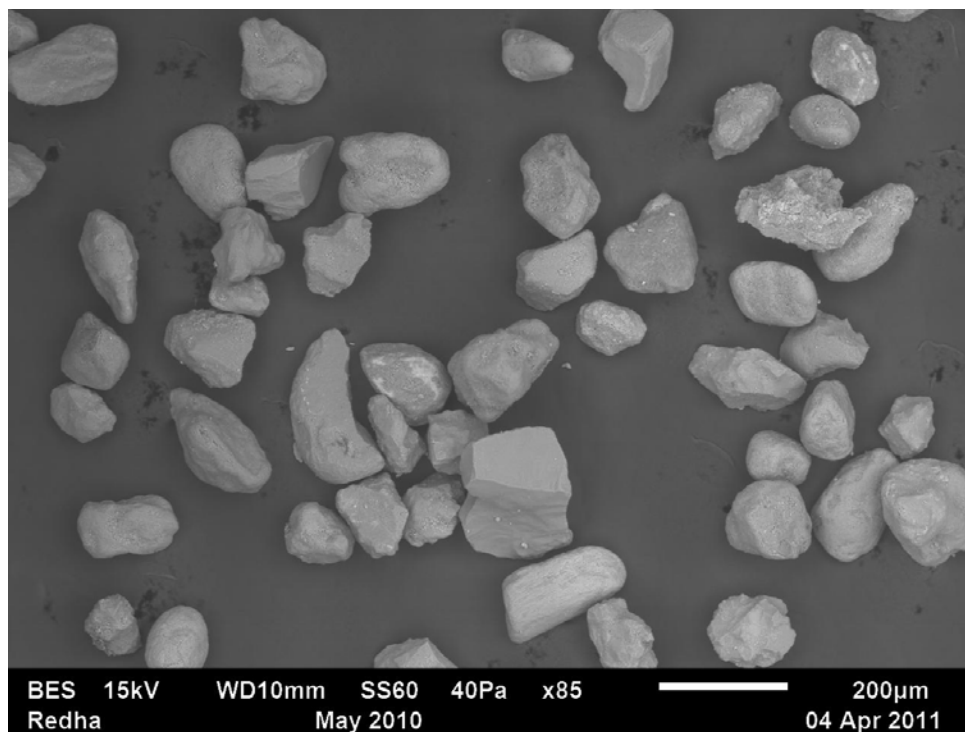


**Figure 3.6 SEM image showing individual dust particles under 500X magnification.**

### **3.4.3 Spectroscopic Analysis**

The second phase of analysis included collecting thermal emission spectra for all samples. For the dust storm samples, collected spectra would be used to identify mineralogical composition, as well as mineral abundance for each storm. The results would be verified by comparing them to both XRD and CCSEM results previously obtained. The spectra of pure mineral dust samples is essential for building a fine grained (less than 63 µm) spectral library that will be used as a reference for analyzing both the dust storm samples and future fine grained samples.

Although the mineral spectral library contained only seven different mineral end members, different size fractions within the same mineral were treated as a separate end member, as changes in particle size at such fine scale become crucial when analyzing spectra. The

different size fractions of the seven different end members resulted in a total of 28 different end members, in addition to the three dust storm spectra.

A Nexus 870 spectrometer was used to collect thermal emission spectra at the Department of Geology and Planetary Science Image Visualization and Infrared Spectroscopy (IVIS) laboratory. This spectrometer has an extended range potassium bromide (XT-KBr) beam splitter and a mercury cadmium telluride (MCT-A) detector, with a spectral range of 5.0 – 25.0  $\mu\text{m}$  (Lee, 2011). Each sample was placed in a copper sample cup painted with high emissivity black paint and placed in an oven and heated to 80°C for 24 hours. Samples from the first 2 storms amounted to less than a gram each, whereas other samples were large enough to provide 2 grams per cup. Prior to running the samples through the spectrometer, two blackbody measurements were taken at 70°C and 100°C. Sample spectra were acquired at 4  $\text{cm}^{-1}$  resolution and 1024 scans per sample to reduce the effect of noise. Raw data was converted to emissivity following the methods outlined by Ruff et al. (1997), and the data was saved in tab delimited text (.txt) file format.

#### **3.4.4 Creation of Dust Spectral Library**

ITT's Environment for Visualizing Images (ENVI) software was used to create a spectral library file for each dust storm and mineral end member using the spectral library builder function. This function allows for specification of wavelength units (micrometers), and gives the user the ability to define each end member by a unique label. Mineral names and their corresponding fraction size were chosen to label each end member (e.g. Quartz 10-20). The .txt spectra files were converted to spectral library format. A spectral range of 5 to 25  $\mu\text{m}$  was used for each end member, allowing for versatility with future types of analyses that can be performed. However,

because of the poor detector sensitivity at wavelengths greater than 20  $\mu\text{m}$ , greater uncertainty (i.e., emissivity values greater than 1) commonly result (e.g. Fig 3.12, 3.14). As this study is focused on mineral identification in the TIR, the 7 to 14  $\mu\text{m}$  range will be the focus, as this corresponds to the wavelength region where most minerals related to eolian environments can be identified.

In addition to the pure end members created, three mixtures were created for validation purposes. These mixtures included mixing calcite and quartz at a ratio of 50:50 and 75:25 respectively. The third mixture consisted of calcite, quartz, and forsterite at 31:31:38 respectively. Due to restrictions on the amount of available mineral dust, the 10-20  $\mu\text{m}$  size range was used for quartz and forsterite, whereas calcite was  $<10 \mu\text{m}$ . A list of the different libraries created is presented in Table 3.2.

**Table 3.2 Different combinations of spectral libraries created for this analysis.**

File Name	Description
Quartz	Spectra of pure quartz in 3 different particle size fractions: $<10 \mu\text{m}$ , 10-20 $\mu\text{m}$ , 20-40 $\mu\text{m}$
Calcite	Spectra of pure calcite in 3 different particle size fractions: $<10 \mu\text{m}$ , 20-45 $\mu\text{m}$ , $> 45 \mu\text{m}$
Andesine	Spectra of pure andesine in 3 different particle size fractions: $<10 \mu\text{m}$ , 10-20 $\mu\text{m}$ , 20-40 $\mu\text{m}$
Dolomite	Spectra of dolomite in 5 different particle size fractions: $< 2.7 \mu\text{m}$ , 2.7-10 $\mu\text{m}$ , 10-20 $\mu\text{m}$ , 20- 45 $\mu\text{m}$ , $> 45 \mu\text{m}$
Forsterite	Spectra of pure forsterite in 5 different particle size

	fractions: < 2.7 $\mu\text{m}$ , 2.7-10 $\mu\text{m}$ , 10-20 $\mu\text{m}$ , 20- 45 $\mu\text{m}$ , > 45 $\mu\text{m}$
Fayalite	Spectra of a fayalite and other unidentified matrix mix in 4 different particle size fractions: < 2.7 $\mu\text{m}$ , 2.7-10 $\mu\text{m}$ , 10-20 $\mu\text{m}$ , 20- 45 $\mu\text{m}$
Muscovite	Spectra of pure muscovite in 4 different particle size fractions: 2.7-10 $\mu\text{m}$ , 10-20 $\mu\text{m}$ , 20- 45 $\mu\text{m}$ , > 45 $\mu\text{m}$
Kaolinite (ASU library)	Spectra of fine (< 2 $\mu\text{m}$ ) obtained from the Arizona State University's spectral library
Fines <10	Spectra of quartz, calcite, dolomite, andesine, fayalite, forsterite and muscovite in the < 10 $\mu\text{m}$ size fraction
Fines 10-20	Spectra of quartz, dolomite, andesine, fayalite, forsterite and muscovite in the 10-20 $\mu\text{m}$ size fraction
Fines 20-45	Spectra of quartz, calcite, dolomite, andesine, fayalite, forsterite and muscovite in the 20-45 $\mu\text{m}$ size fraction
AllSpectra	All above spectra, including kaolinite
MaySpectra	Spectrum collected from the May 2010 dust storm
JulySpectra	Spectrum collected from the July 2010 dust storm

MarchSpectra	Spectrum collected from the March 2011 dust storm
July_March_Spectra	Combined spectra of both the July and March storms. May storm was excluded due to difference in number of scans.
C + K + Q	Spectra of calcite (< 10, 20-45), kaolinite, and quartz (< 10, 10-20).
C + Q	Spectra of calcite (< 10, 20-45, >45), and quartz (< 10, 10-20, 20-40).
Mix C + Q	50:50 mixture of calcite (<10) and quartz (10-20).
Mix C + Q	75:25 mixture of calcite (<10) and quartz (10-20).
Mix C + Q + Forsterite	31:31:38 mixture of calcite (<10), quartz (10-20) and forsterite (10-20).

---

## 3.5 RESULTS

### 3.5.1 XRD and CCSEM

The particle size range for the three dust storm samples identified by CCSEM illustrated a very fine (< 60  $\mu\text{m}$ ) particle size distribution ranging from 1 to 42  $\mu\text{m}$ , with roughly 60% of the dust particles having a 1-4  $\mu\text{m}$  size (Fig 3.8 a, b, c). XRD results showed calcite being the dominant mineral in all three samples, followed by quartz, feldspar, dolomite, and other trace minerals (Table. 3.3). The sum of the mineral phases does not equal 100, indicating the presence of other



trace or minor elements that were not identified by XRD due to either instrument limitations or phases peak overlap.

The size distribution and mineral composition findings of both CCSEM and XRD analyses are in agreement with scientific literature related to the general nature of dust storms and their characteristics in the study area. A study by Engelbrecht et al. (2009) analyzed top soil collected from U.S. military bases in the Middle East, and concluded that surface deposits in Kuwait are dominated by silicates, whereas surface deposits in neighboring Iraq were dominated by calcite and dolomite (Fig. 3.7). As the three dust samples exhibit slightly higher concentrations of calcite in comparison to silicates, this is an indication of possible long-range transportation and a dust source near Iraq and Syria.

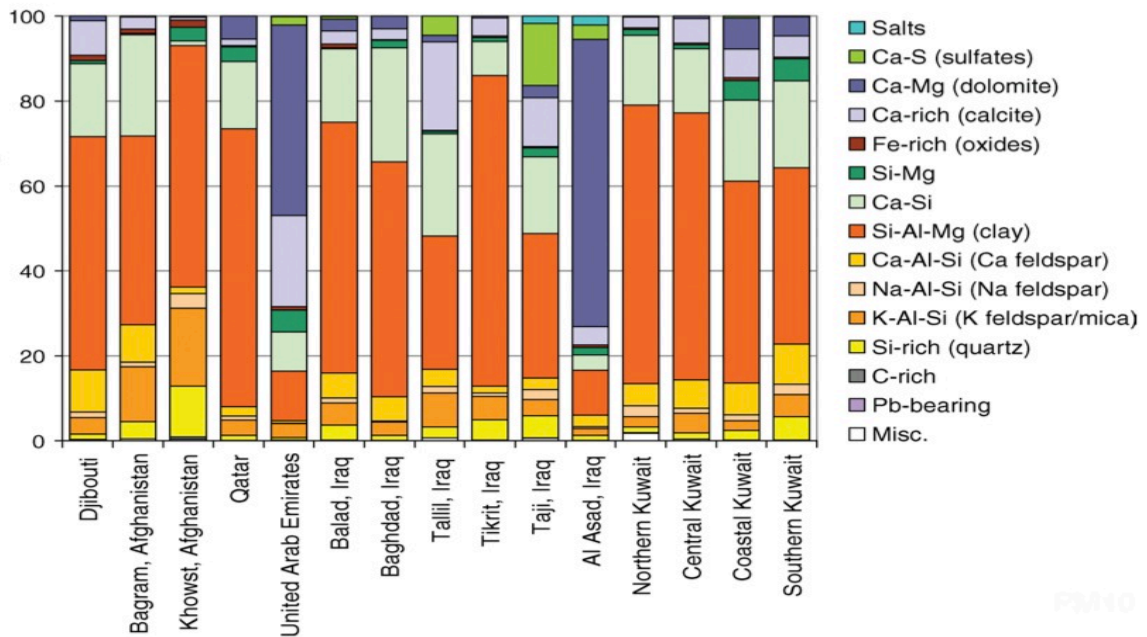


**Figure 3.7** Composition of various dust samples collected throughout the Middle East, showing variation in dust content (Engelbrecht et al., 2009). Higher levels of carbonates found in Iraq and in dust storms affecting Kuwait indicate a source near Iraq.

**Table 3.3 XRD results outlining major minerals found in the dust samples.**

May 2010	Phase	Composition	Concentration
	Calcite	Ca(CO <sub>3</sub> )	14-19
	Quartz	SiO <sub>2</sub>	8-13
	Feldspar	(K,Na, Al) Si <sub>3</sub> O <sub>8</sub>	3-8
	Dolomite	CaMg(CO <sub>3</sub> ) <sub>2</sub>	1-5
	Mica	KAl <sub>2</sub> (AlSi <sub>3</sub> O <sub>10</sub> )(F,OH) <sub>2</sub>	1-5
	Chlorite/Serpentine	(Mg,Al) <sub>6</sub> (Si,Al) <sub>4</sub> O <sub>10</sub> (OH) <sub>8</sub>	< 2
July 2010	Calcite	Ca(CO <sub>3</sub> )	26-31
	Quartz	SiO <sub>2</sub>	25-30
	Feldspar	(K,Na, Al) Si <sub>3</sub> O <sub>8</sub>	6-11
	Dolomite	CaMg(CO <sub>3</sub> ) <sub>2</sub>	2-7
	Mica	KAl <sub>2</sub> (AlSi <sub>3</sub> O <sub>10</sub> )(F,OH) <sub>2</sub>	1-5
	Chlorite/Serpentine	(Mg,Al) <sub>6</sub> (Si,Al) <sub>4</sub> O <sub>10</sub> (OH) <sub>8</sub>	<2
March 2011	Calcite	Ca(CO <sub>3</sub> )	26-31
	Quartz	SiO <sub>2</sub>	25-30
	Feldspar	(K,Na, Al) Si <sub>3</sub> O <sub>8</sub>	6-11
	Dolomite	CaMg(CO <sub>3</sub> ) <sub>2</sub>	2-7
	Mica	KAl <sub>2</sub> (AlSi <sub>3</sub> O <sub>10</sub> )(F,OH) <sub>2</sub>	1-5
	Gypsum	CaSO <sub>4</sub> * 2H <sub>2</sub> O	1-5

### 3.5.2 Fine Particles Library

#### Andesine

The andesine spectra representative of the three particle size groups show emissivity lows at 9.2  $\mu\text{m}$ , with the largest particles (20-40  $\mu\text{m}$ ) having the lowest emissivity value at 0.95, whereas the smallest particles (<10  $\mu\text{m}$ ) had the highest emissivity value at 0.97. Transparency features associated with fine particles appear at 11.8  $\mu\text{m}$  and show a linear behavior with changing particle size (Fig 3.9, Fig 3.10).

#### Calcite

The calcite spectra representative of the three particle size groups show emissivity lows at 6.5  $\mu\text{m}$ , typical of calcite and outside of the typical 8-12  $\mu\text{m}$  window used in mineral identification. A second emissivity low appears at 11.3  $\mu\text{m}$ , whereas transparency features appear at 8  $\mu\text{m}$  and 11.7  $\mu\text{m}$  respectively (Fig 3.11, Fig 3.12).

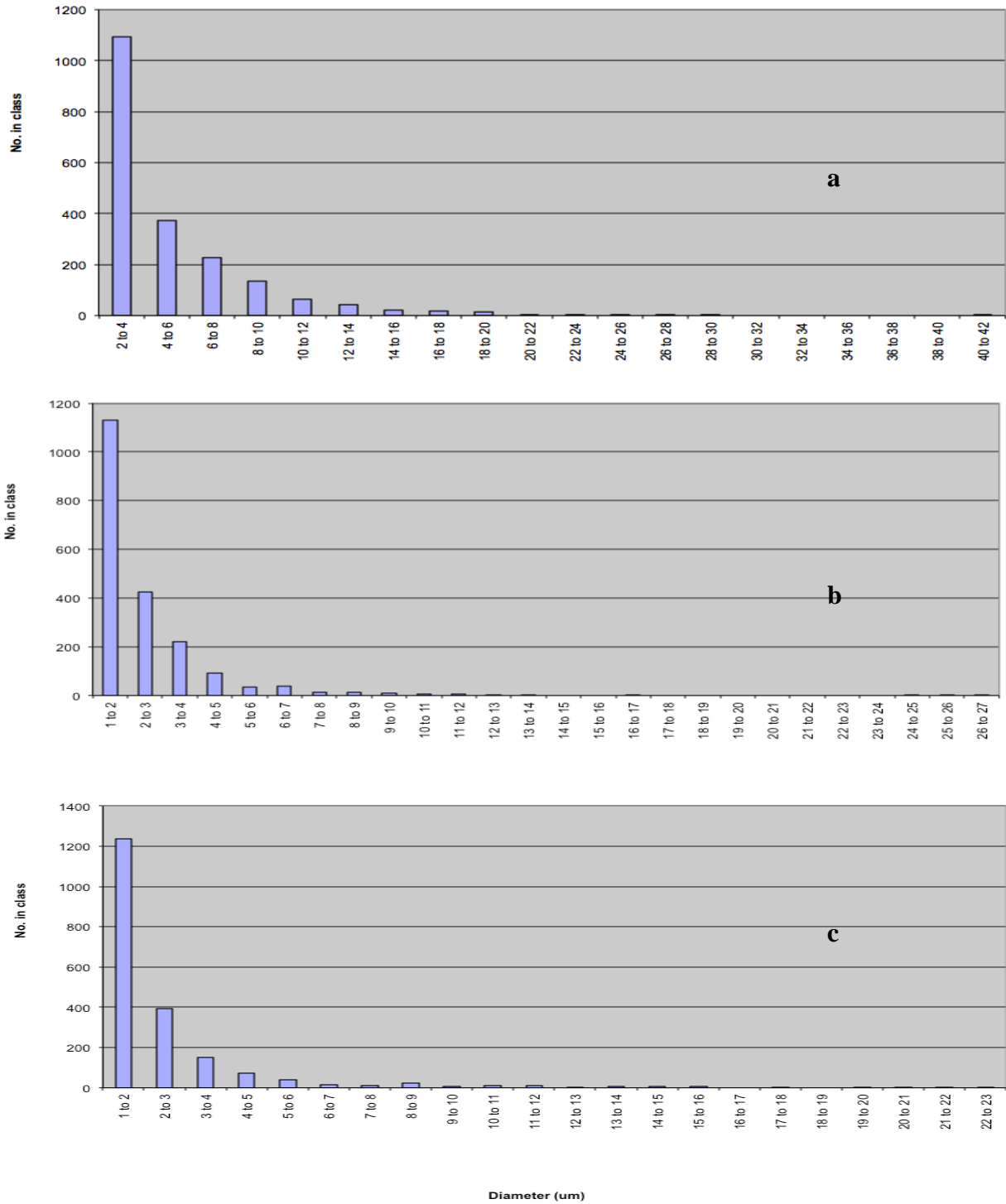


**Figure 3.8** Particle size distribution identified by CCSEM for the three dust storm samples (a = May 2010, b = July 2010, c = March 2011) shows 60% of particles were in the 1-4  $\mu\text{m}$  size range.

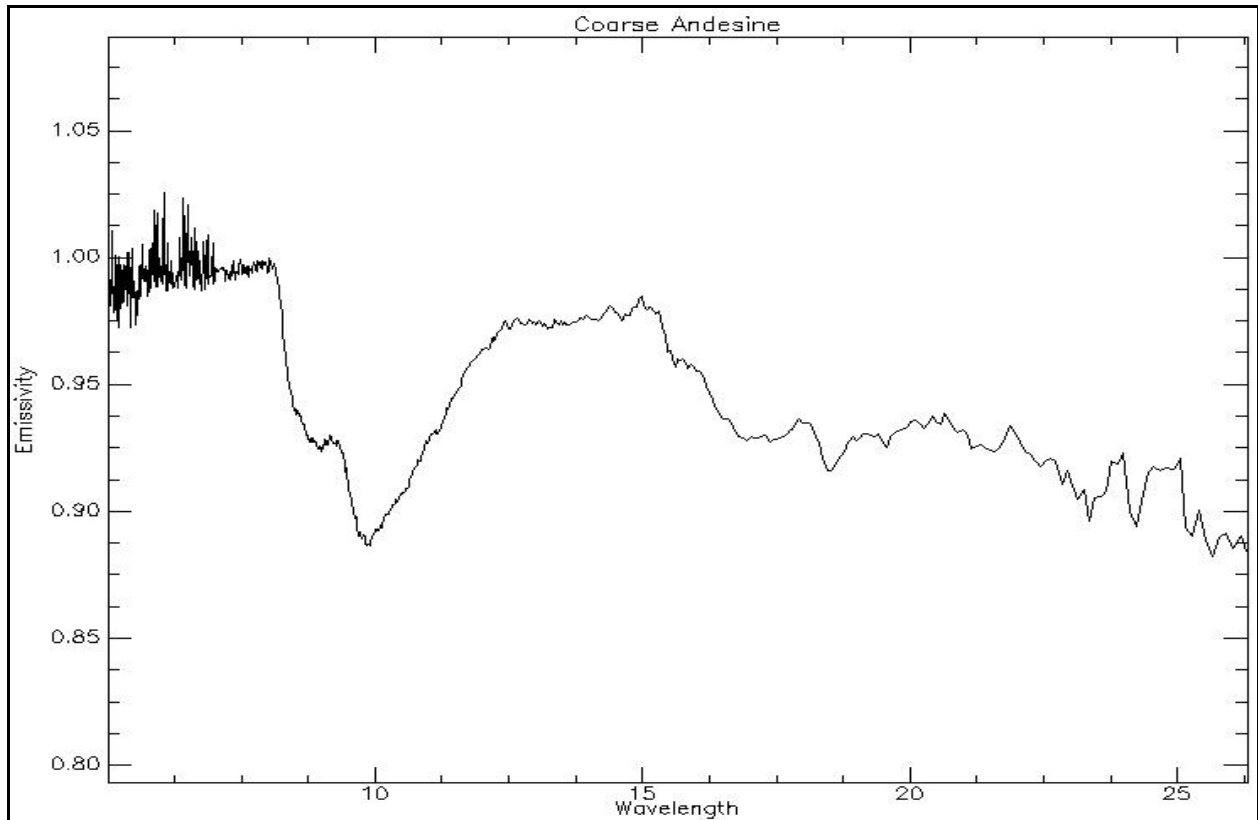
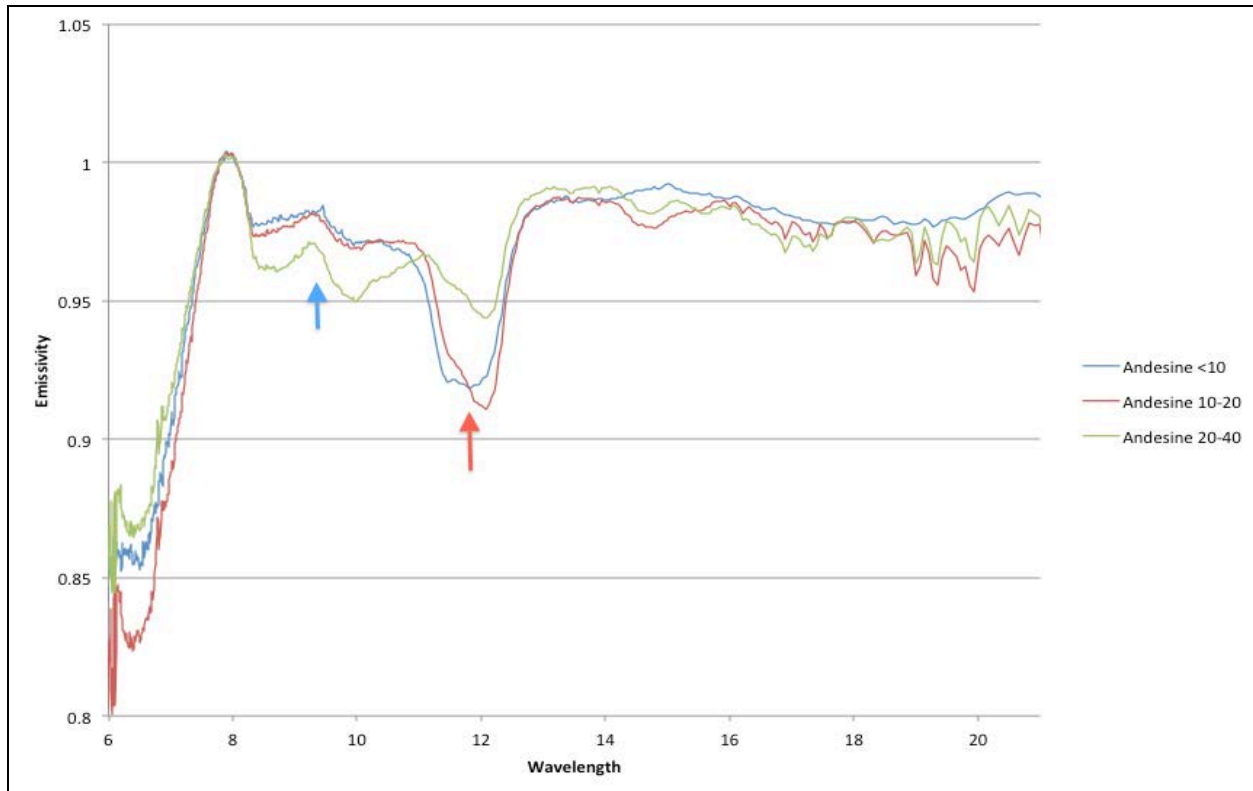


Figure 3.9 Coarse (>125  $\mu\text{m}$ ) andesine spectrum from ASU's spectral library (Chrsitensen et al., 2000)



**Figure 3.10 Andesine spectral library showing a reflectance feature at 9.2  $\mu\text{m}$  (blue arrow) and a transparency feature at 11.8  $\mu\text{m}$  (red arrow).**

### Dolomite

The Dolomite spectra representative of the five particle size groups show emissivity lows at 6.4  $\mu\text{m}$ , outside of the 8-12  $\mu\text{m}$  TIR window. A second set of emissivity lows form at 10.8  $\mu\text{m}$ , whereas one transparency feature forms at 10.3  $\mu\text{m}$  (Fig 3.13, Fig 3.14).

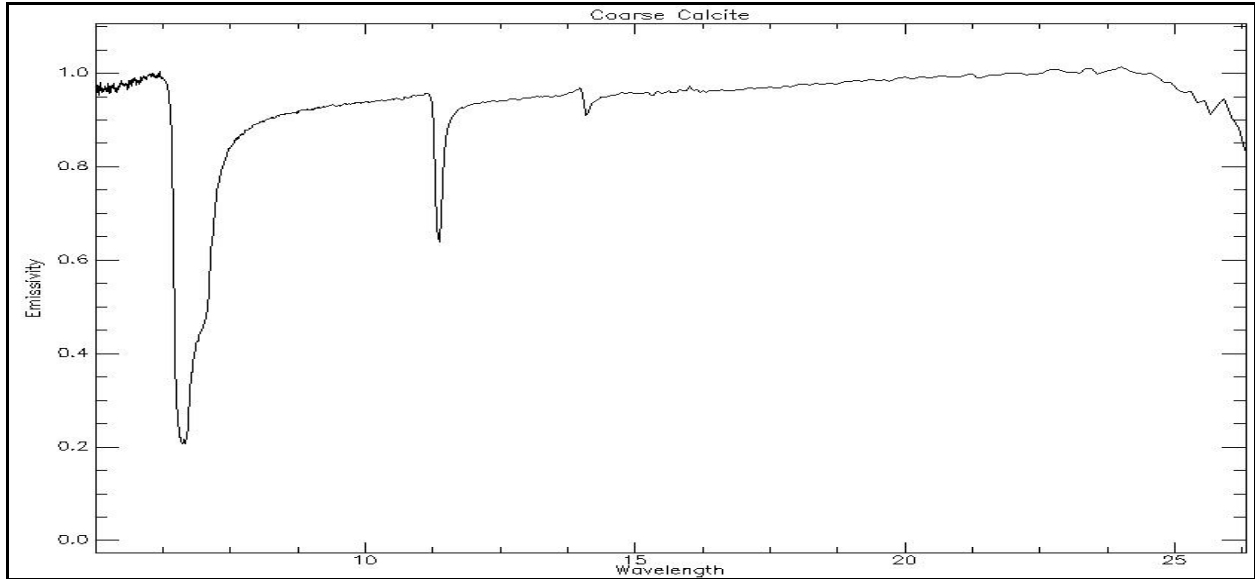


Figure 3.11 Coarse (>125  $\mu\text{m}$ ) calcite spectrum from ASU's spectral library (Christensen et al., 2000).

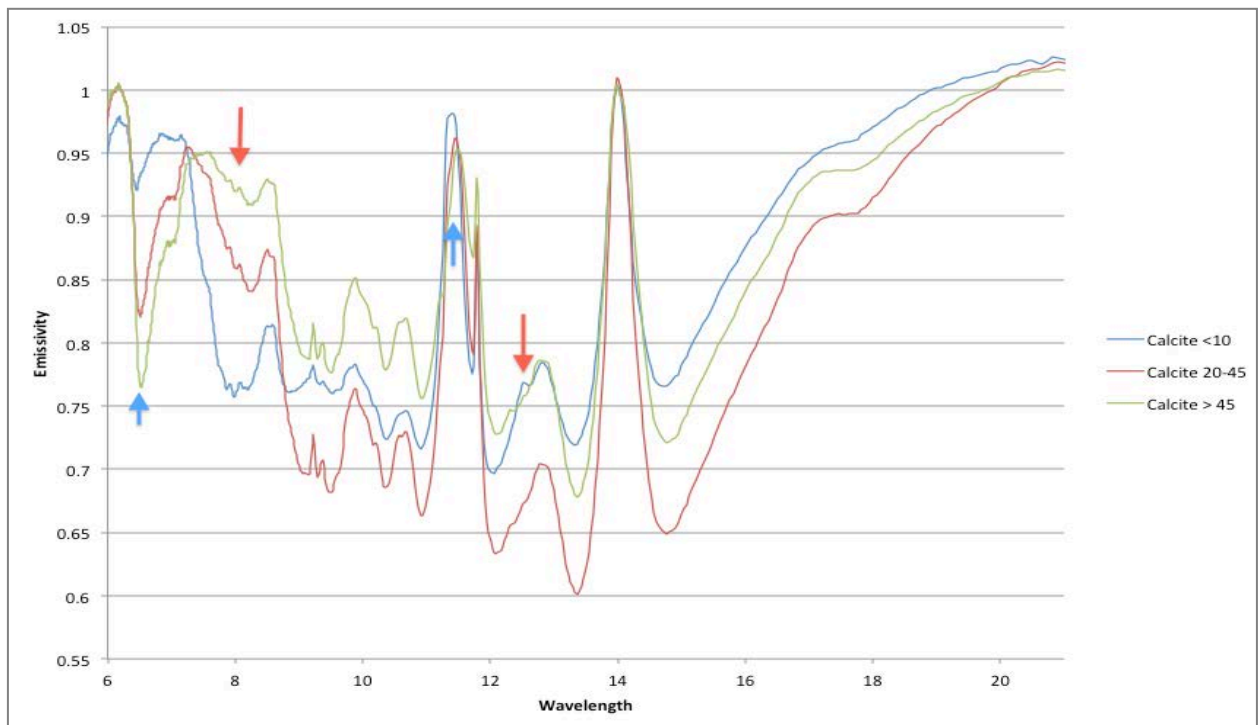
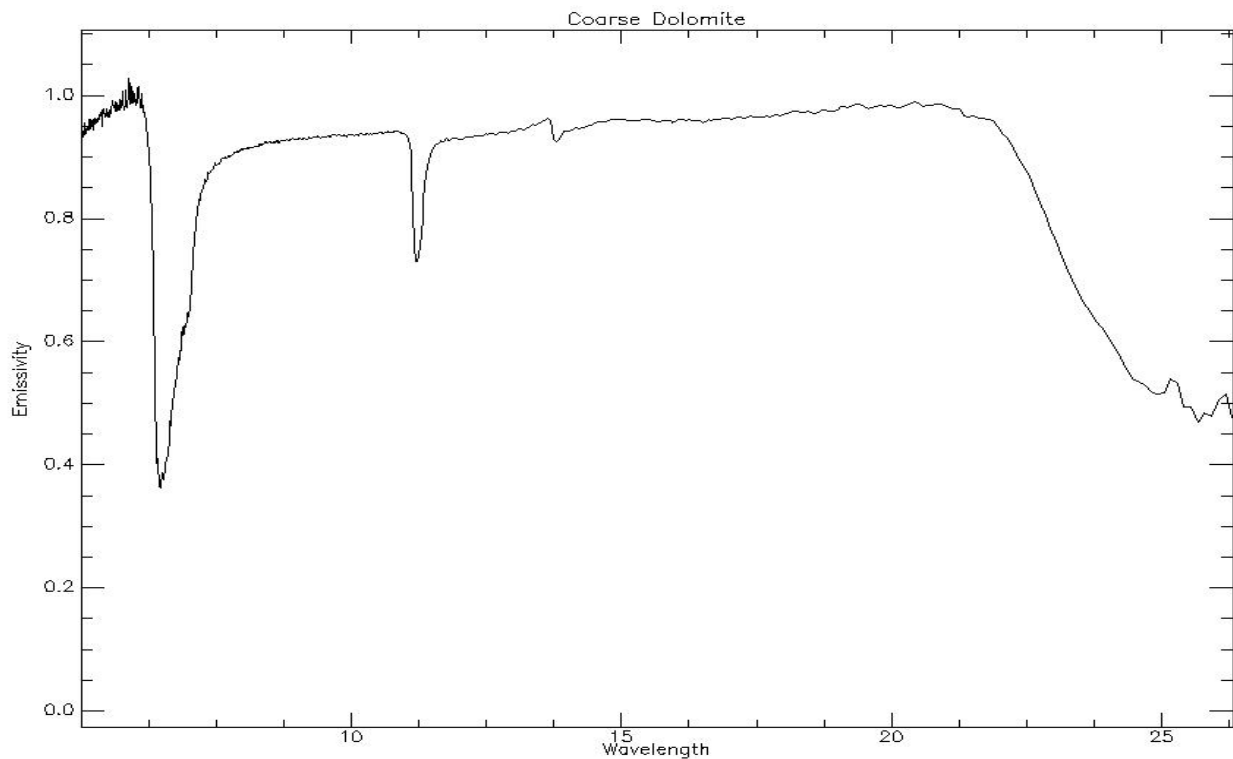


Figure 3.12 Calcite spectral library showing emissivity lows at 6.5  $\mu\text{m}$  and 11.3  $\mu\text{m}$  (blue arrows) and transparency features (red arrows).

## Fayalite

Pure fayalite typically has emissivity lows at 11.5  $\mu\text{m}$ . However, the study's fayalite spectra had emissivity lows at 9  $\mu\text{m}$ , whereas the transparency feature was observed at 11.5  $\mu\text{m}$ . The discrepancy between the typical behavior of fayalite and this study's results is attributed to the presence of an unknown matrix that was not separated from the fayalite particles at the time of powder preparation, and therefore, these results clearly indicate the presence of other minerals that have affected the position of both the emissivity lows and the transparency feature (Fig 3.15. Fig 3.16).



**Figure 3.13** Coarse (>125  $\mu\text{m}$ ) dolomite spectrum from ASU's spectral library (Christensen et al., 2000).



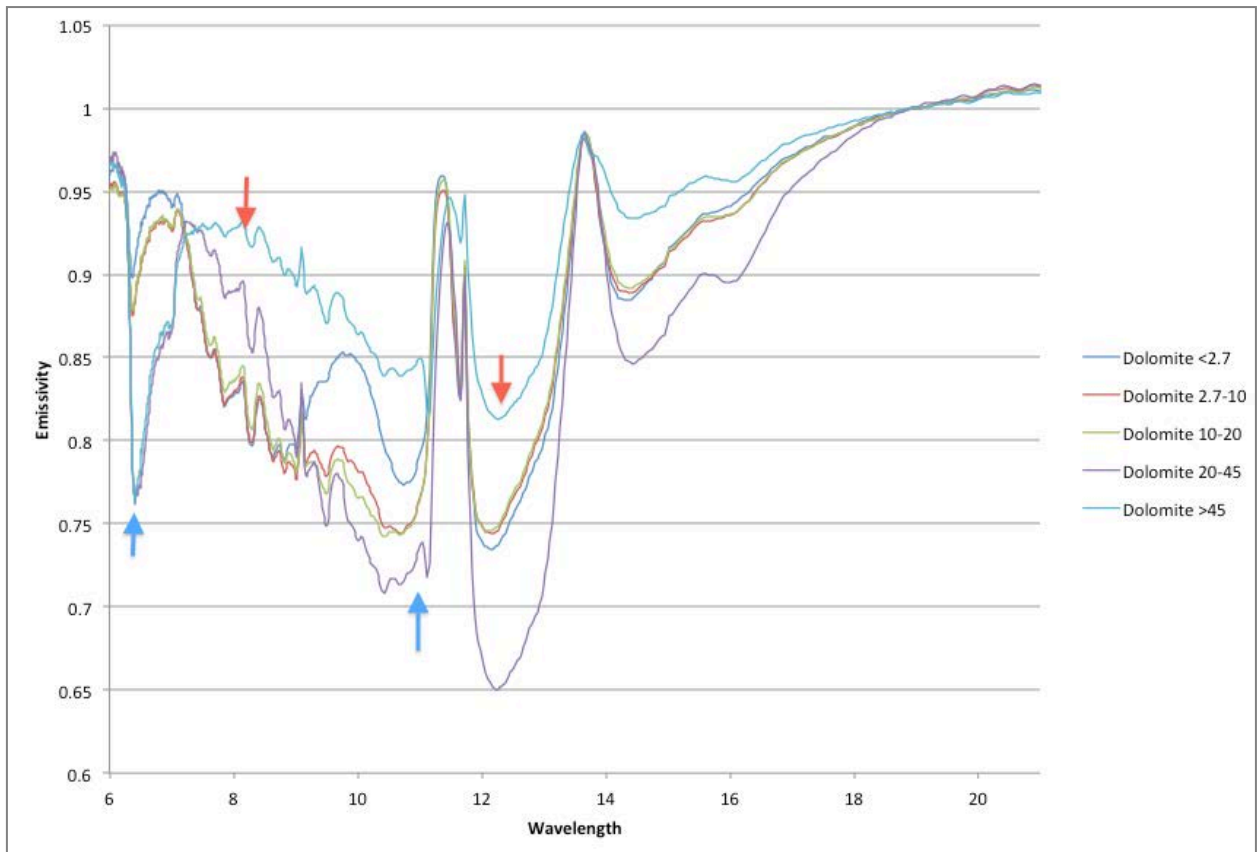


**Figure 3.14 Dolomite spectral library showing emissivity lows at 6.4  $\mu\text{m}$  and 10.8  $\mu\text{m}$  (blue arrows) and transparency features (red arrows).**

### Forsterite

The forsterite spectra representative of the five particle size groups show emissivity lows at 10.4  $\mu\text{m}$ , whereas a transparency feature forms at 13  $\mu\text{m}$  and exhibits the linear behavior typical of very fine grains (Fig 3.17, Fig 3.18).

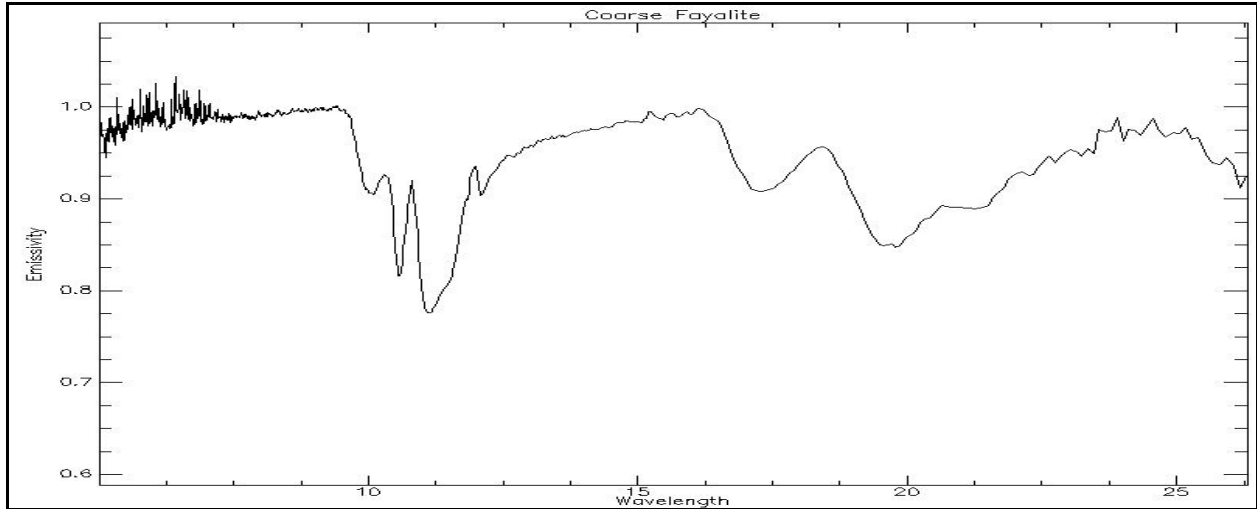


Figure 3.15 Coarse (>125  $\mu\text{m}$ ) fayalite spectrum from ASU's spectral library (Christensen et al., 2000).

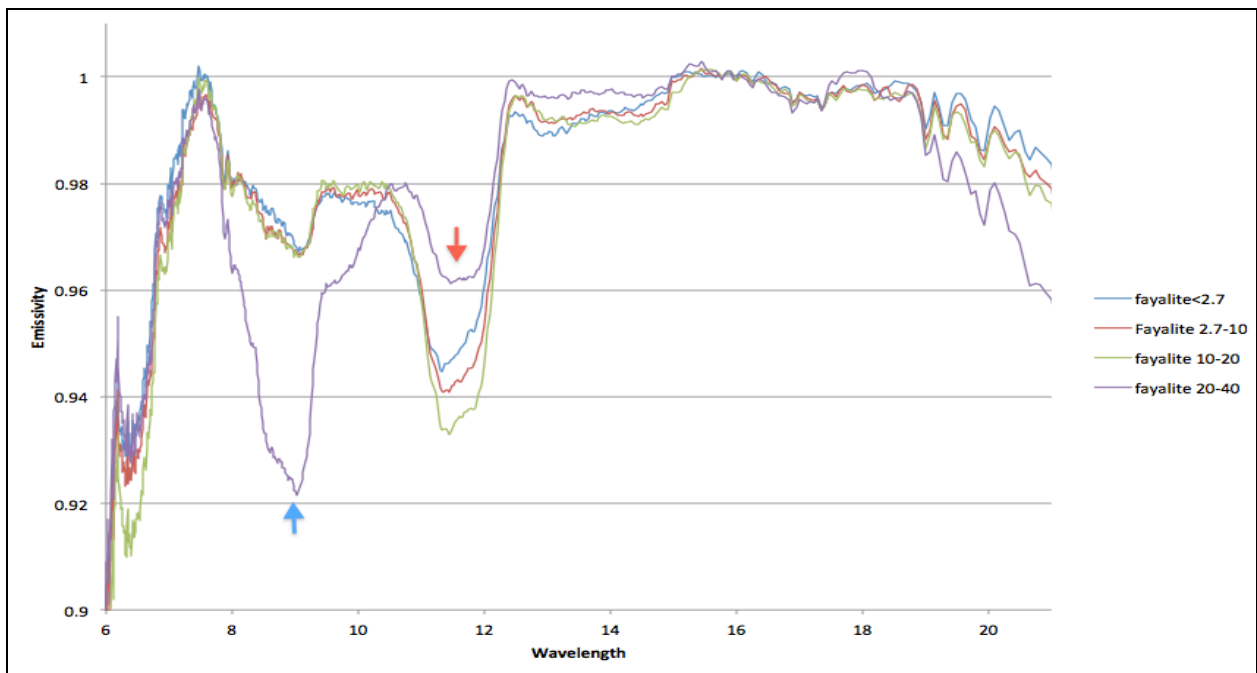
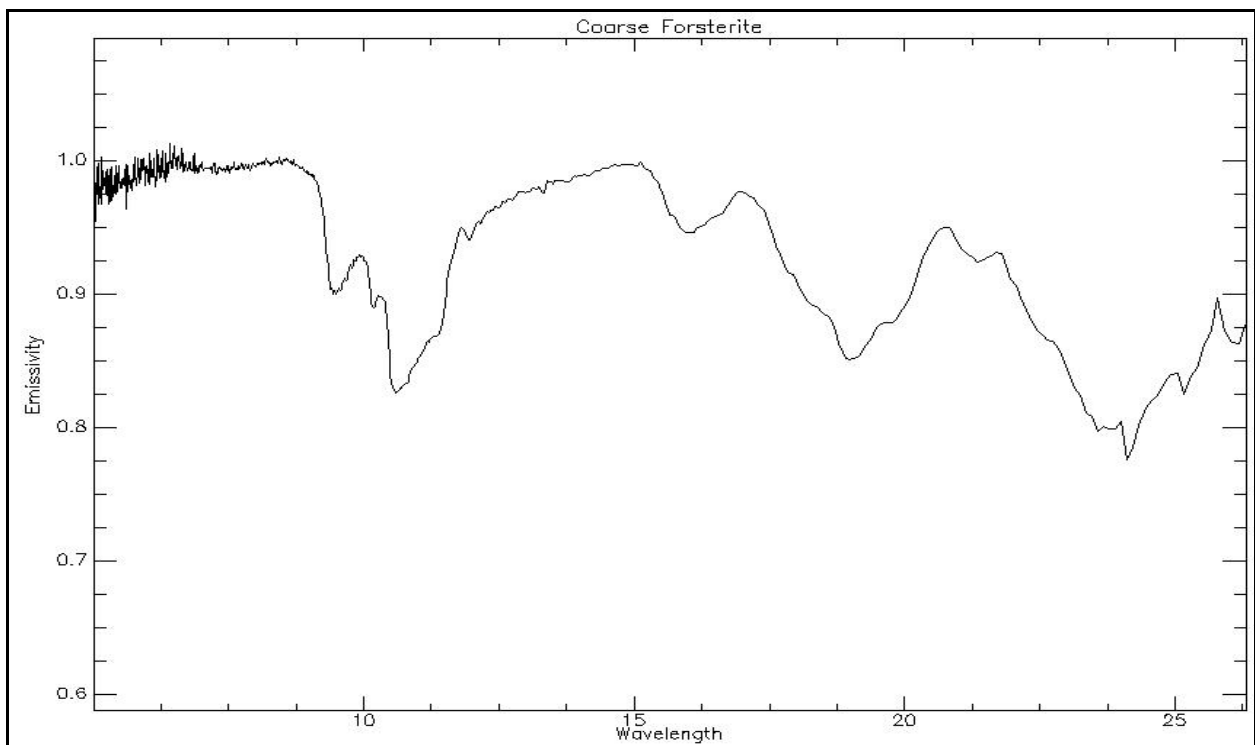


Figure 3.16 Spectra of the fayalite mixture showed an emissivity low at 9  $\mu\text{m}$ , indicating the presence of other minerals in the mixture, whereas pure fayalite has an emissivity low at 11.5  $\mu\text{m}$ .

## Kaolinite

The emissivity spectrum for kaolinite was generated using data from ASU's online spectral library collection. It contained one size fraction of 2  $\mu\text{m}$ , and was relatively noisy (Fig 3.19, Fig 3.20). An emissivity low at 9.2  $\mu\text{m}$  can be seen, whereas the lack of other size fractions for comparison did not allow for an accurate assessment for the present or the location of a transparency feature (Christensen et al., 2000).



**Figure 3.17** Coarse ( $>125 \mu\text{m}$ ) forsterite spectrum from ASU's spectral library (Christensen et al., 2000).

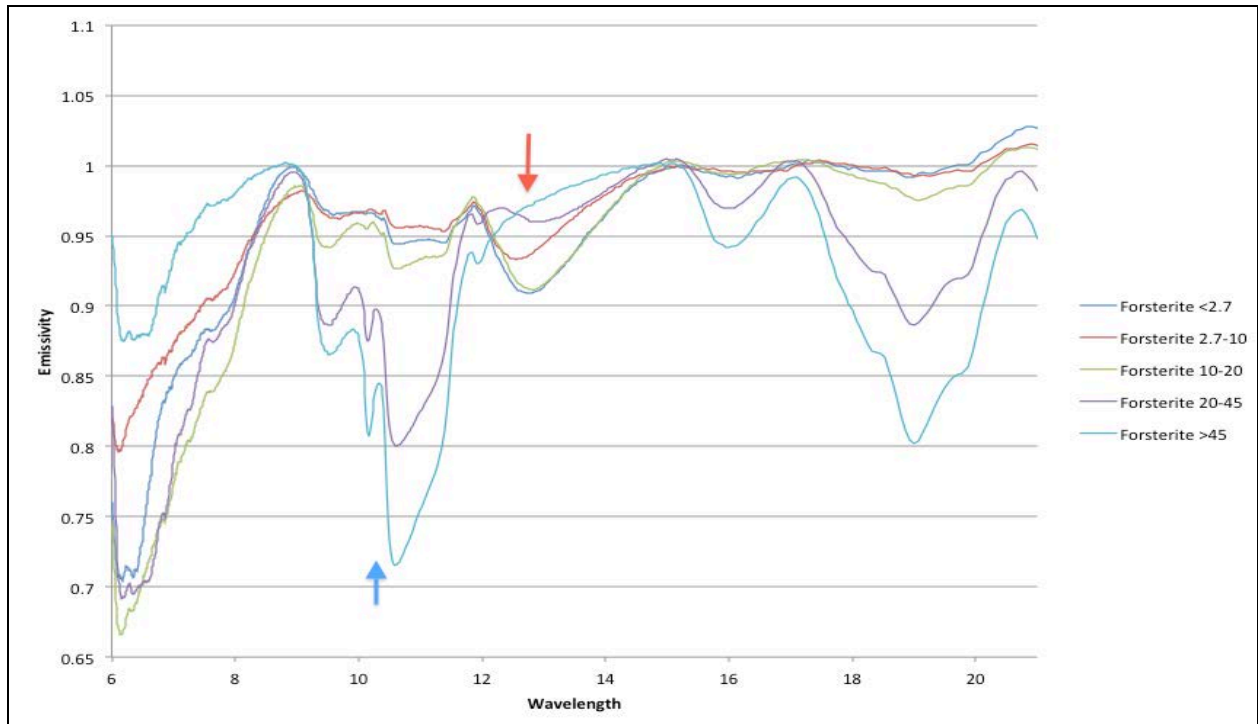


**Figure 3.18 Forsterite spectral library showing an emissivity low at 10.4  $\mu\text{m}$  (blue arrow) and a transparency feature (red arrow).**

### Muscovite

The muscovite spectra representative of the four particle size groups show emissivity lows at 9.6  $\mu\text{m}$ , whereas no transparency features were observed (Fig 3.21, Fig 3.22).

### Quartz

The quartz spectra representative of the three particle size groups clearly show a distinctive quartz-doublet emissivity low at 9.1  $\mu\text{m}$ , with emissivity values increasing with decreasing particle size (Fig 3.23, Fig 3.24). A very distinct transparency feature forms at 11  $\mu\text{m}$ , and exhibits the linear behavior typical of very fine grains.

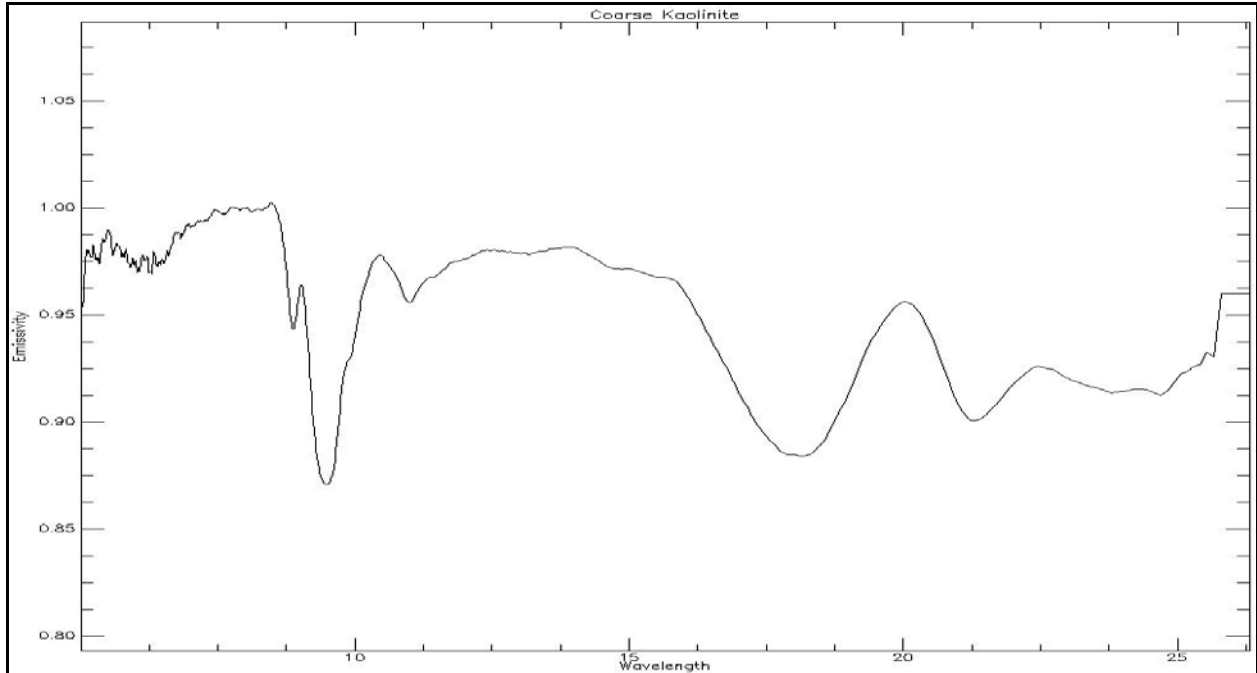


Figure 3.19 Coarse (>125  $\mu\text{m}$ ) kaolinite spectrum from ASU's spectral library (Christensen et al., 2000).

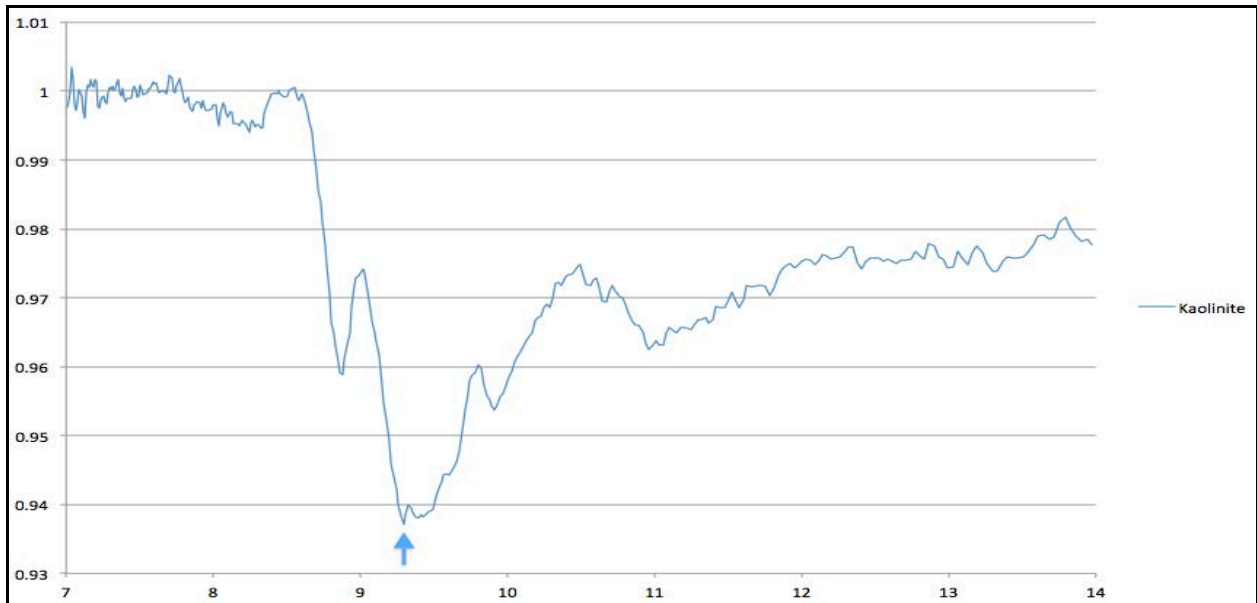


Figure 3.20 Spectral data obtained from ASU's spectral library was used to plot a single size fraction spectrum of kaolinite. It has an emissivity low at 9.2  $\mu\text{m}$  (blue arrow).

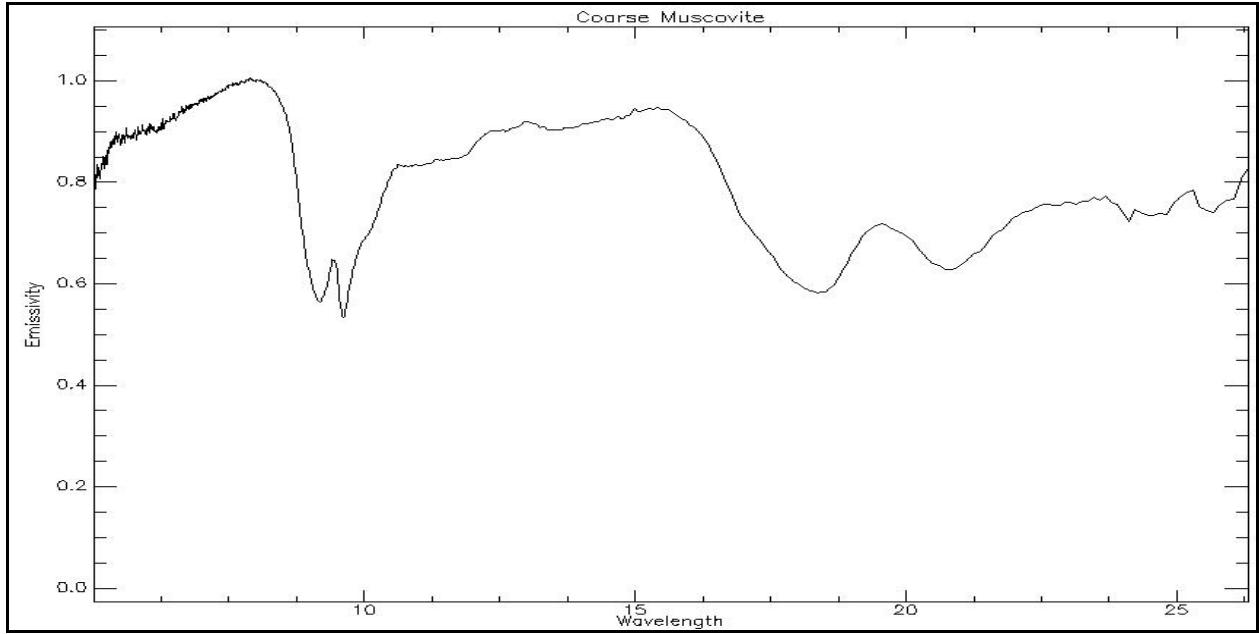


Figure 3.21 Coarse (>125  $\mu\text{m}$ ) muscovite spectrum from ASU's spectral library (Christensen et al., 2000).

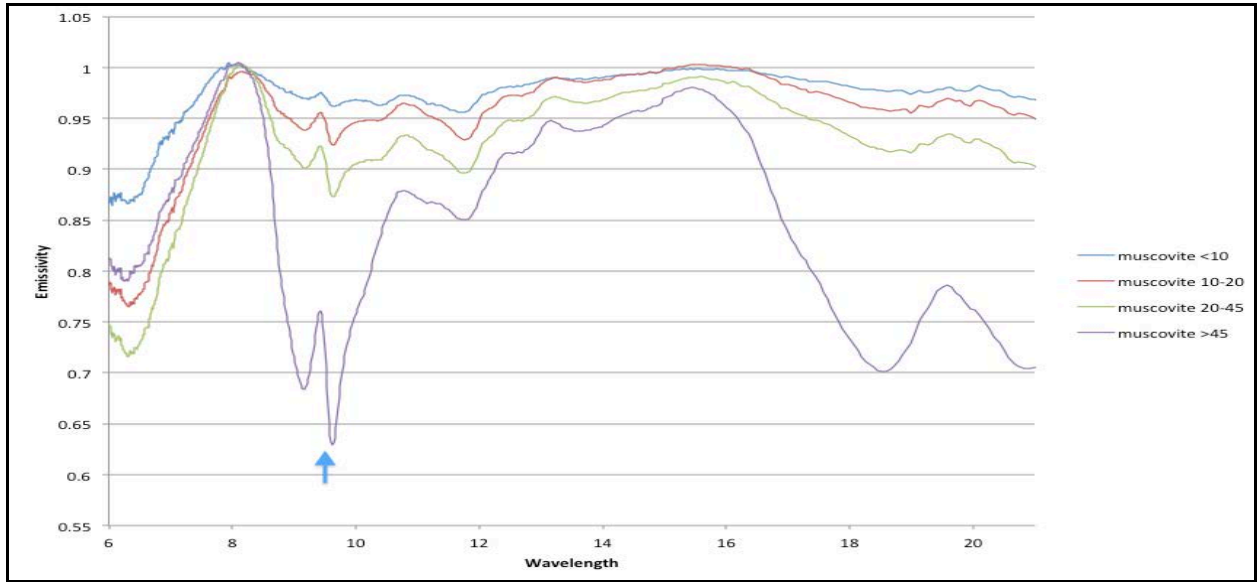


Figure 3.22 Muscovite spectra show an emissivity feature at 9.6  $\mu\text{m}$  (blue arrow) and no transparency feature.

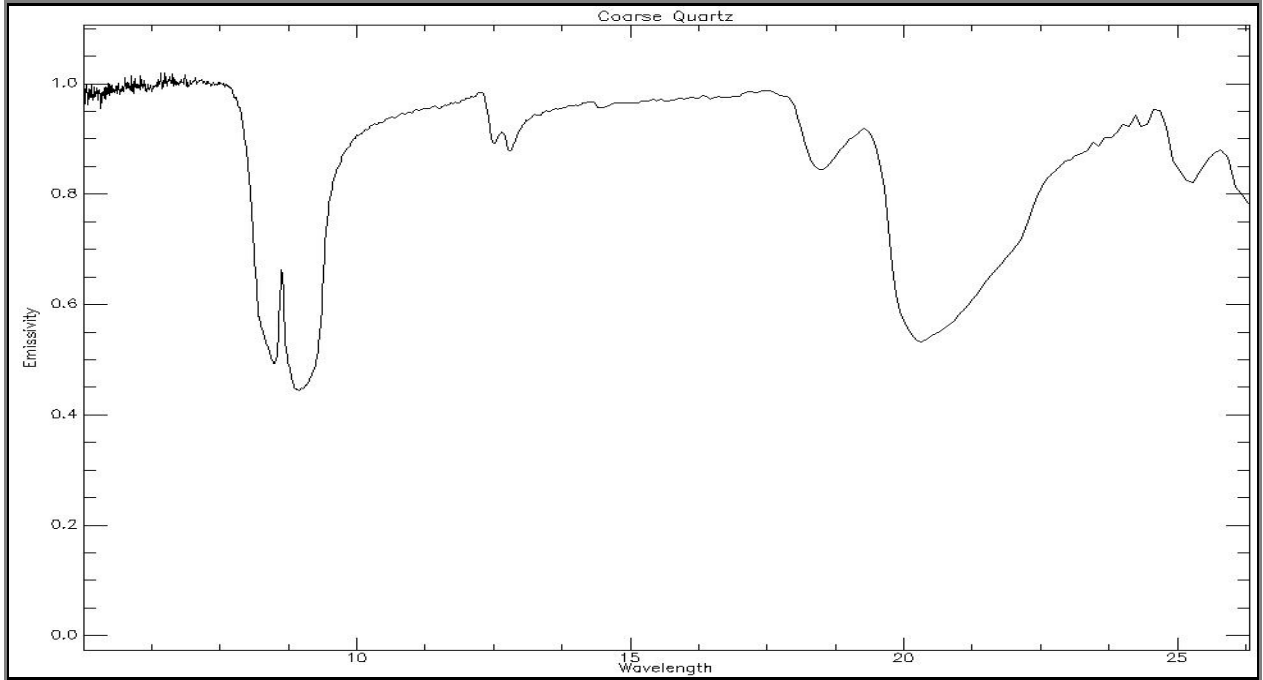


Figure 3.23 Coarse (>125  $\mu\text{m}$ ) quartz spectrum from ASU's spectral library (Christensen et al., 2000).

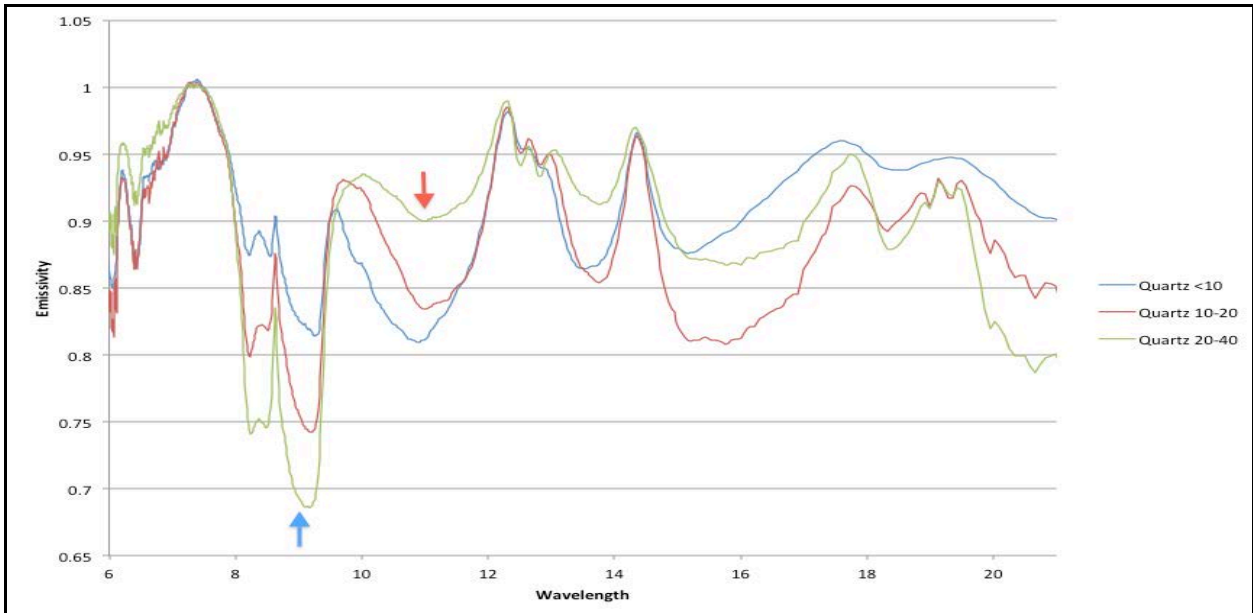


Figure 3.24 Quartz spectra show the distinct doublet feature at 9.1  $\mu\text{m}$  (blue arrow) and transparency feature (red arrow).

### 3.5.3 Dust Spectroscopic Analysis

Initial evaluation of the dust spectra revealed that emissivity values were confined to the 0.94-1.0 region, indicative of fine particles that are strong emitters in the TIR region (Salisbury et al., 1991). Visual interpretation of the spectra denoted the presence of clear quartz spectral features, particularly in the May dust sample, where the quartz doublet feature can be easily identified (Fig. 3.25). Further interpretation showed calcite spectral features, although few were outside of the 8-12  $\mu\text{m}$  window. However, second calcite spectral features at 11.3  $\mu\text{m}$  are present in all three spectra (Figures 3.25, 3.26, 3.27). Additional mineral spectra identified included feldspar, kaolinite, dolomite, and possibly a fayalite spectral feature.

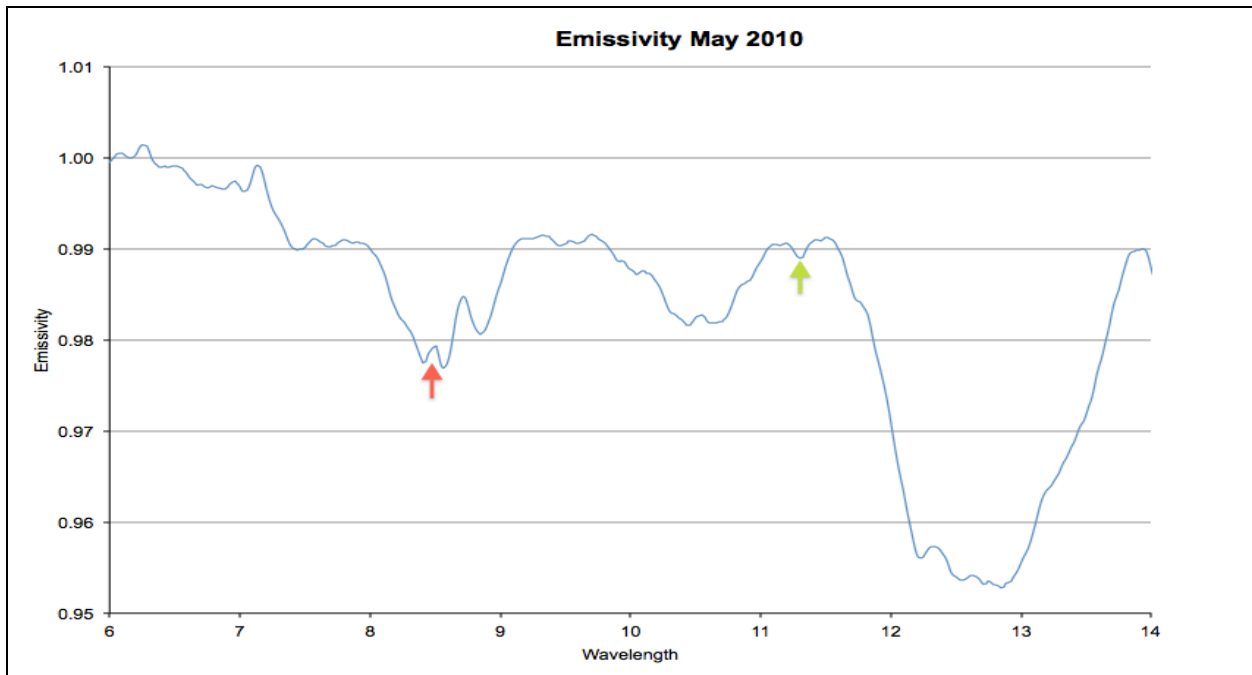


Figure 3.25 Emissivity spectrum generated by the May storm. The arrows show the quartz and calcite features.



The second step included unmixing of the dust spectra using the spectral libraries outlined in section 3.4.3, in addition to a pre-installed spectral library created by ASU that included over 100 known end members and minerals. The model used for spectral deconvolution or unmixing was developed by Ramsey and Christensen (1998) and uses a constrained, least squares linear retrieval algorithm, where a simple statistical determination of the best fit end member percentages can be determined for a given mixture. This model differs from previous models in that it can be applied to high-resolution laboratory data and it uses emissivity rather than radiance (Ramsey and Christensen, 1998). Two constraints must be placed when running the model to eliminate negative values. The success of unmixing is measured by how well the modeled spectra fit the unmixed spectra, and by the root mean square (RMS) error that is calculated for each unmixing process. The RMS error is a value that denotes residual errors or absorption features that were not included in the modeling due to an end member not being present in the library or the presence of atmospheric noise (Ramsey and Christensen, 1998). Lower RMS values indicate a good fit and higher values indicate a poor fit. The unmixing algorithm used here uses an RMS value of 0.01 as a cutoff point, where higher values indicate a poor fit and lower values indicate a good fit.

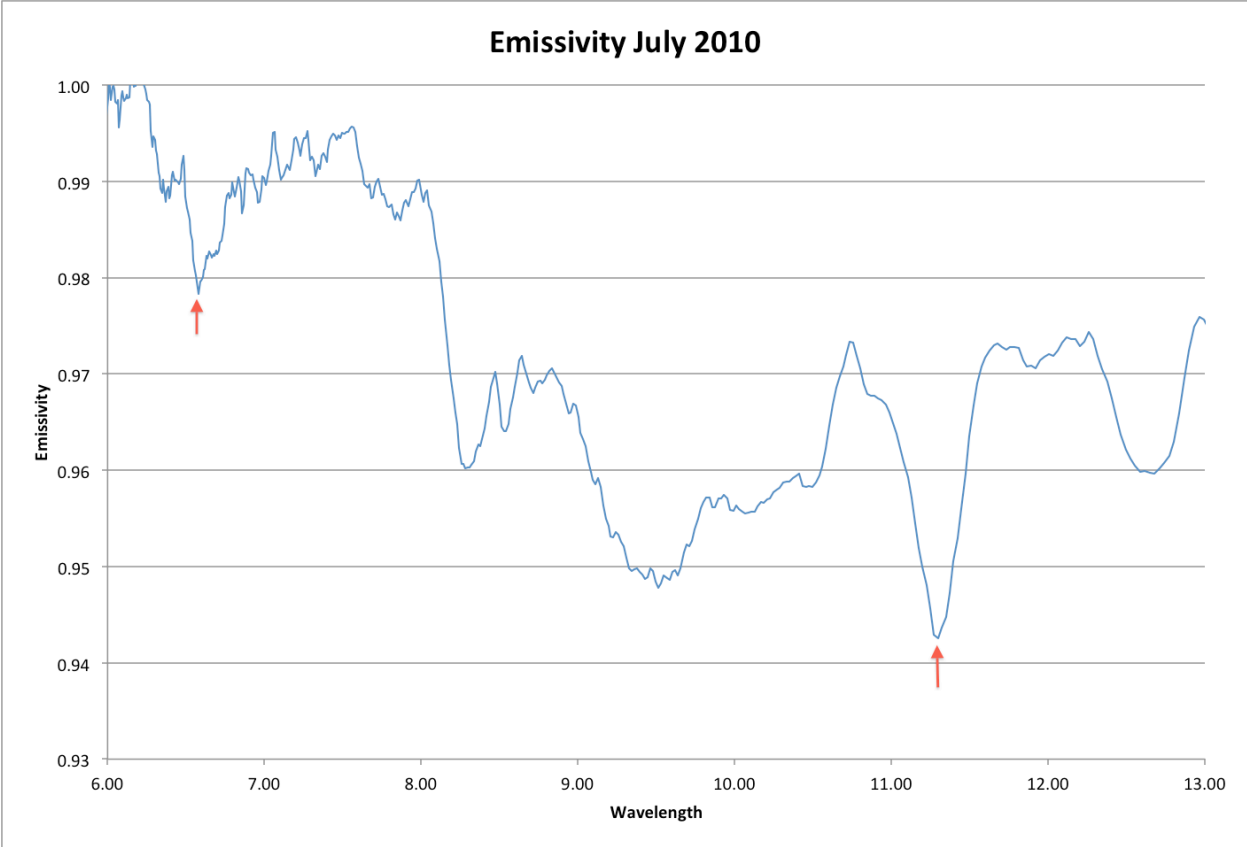
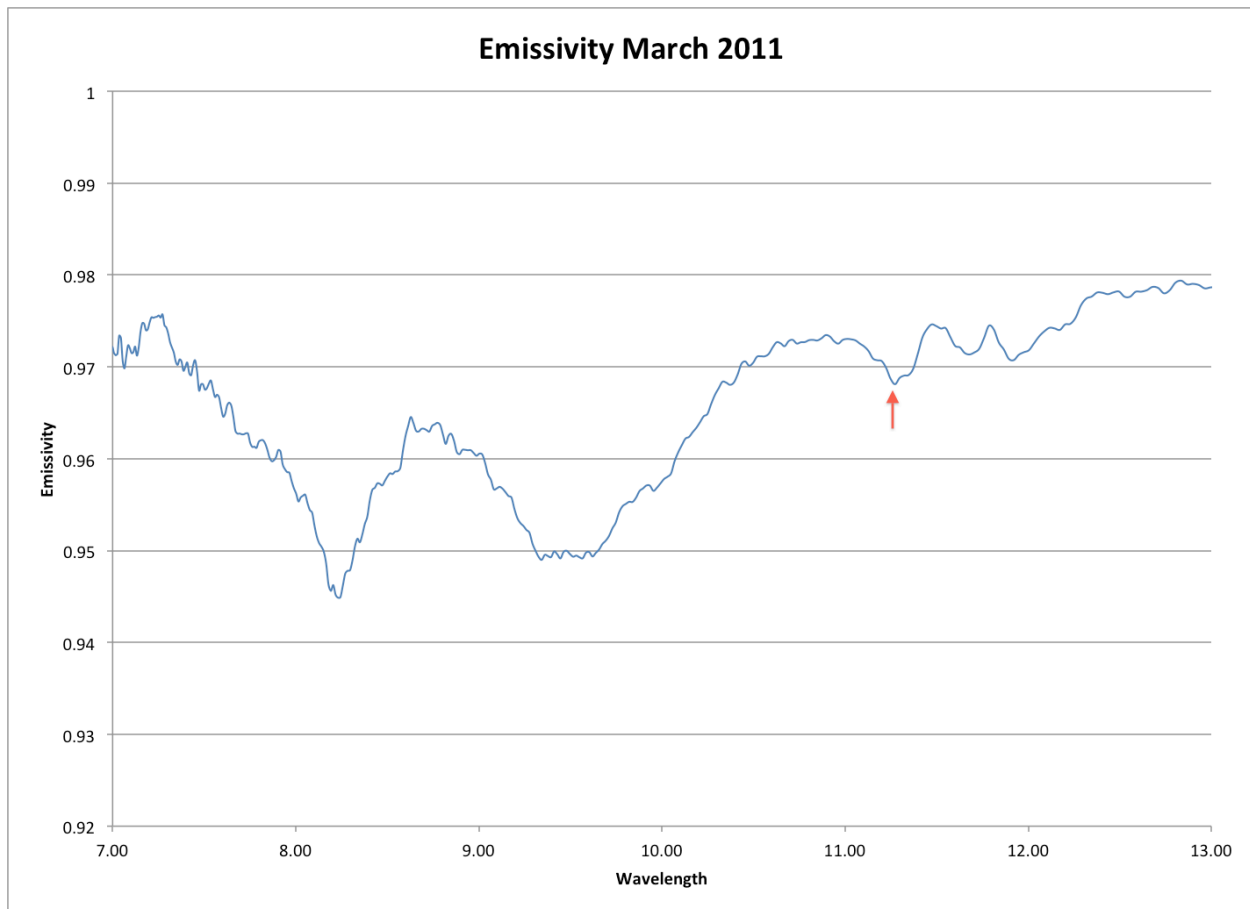


Figure 3.26 Spectrum of the July storm shows calcite features at 6.5 μm and 11.3 μm (highlighted by arrows).



**Figure 3.27** Spectrum of the March storm shows a calcite feature at 11.3  $\mu\text{m}$  (highlighted by arrow).

### May Spectrum

Running the unmixing using all 28 end members (see section 3.4.4) resulted in an RMS value = 0.0191, and a composition estimation of 71.24% Andesine (<10  $\mu\text{m}$ ) and 28.75% calcite (<10  $\mu\text{m}$ ). Figure 3.28 shows the modeled fit, and despite the prominent quartz doublet feature that can be seen in the dust spectra, the model failed to identify quartz. Using the entire ASU library produced an RMS value = 0.0106. However, the identified end members were 93.05% magnetite, 6.67% calcite, and 1.40% gypsum. Despite the relatively lower RMS value, the model fit was off (Fig. 3.29). A third unmixing attempt was made using the C+K+Q (calcite,

kaolinite, quartz) spectral library, and that generated an  $RMS = 0.0111$ , and a composition estimation of 100% calcite (20-45  $\mu\text{m}$ ), with a model that failed to identify the prominent quartz feature (Fig. 3.30). The same RMS value and composition results were obtained when using the C+Q (calcite, quartz) spectral library, with a similar model fit (Fig. 3.31).

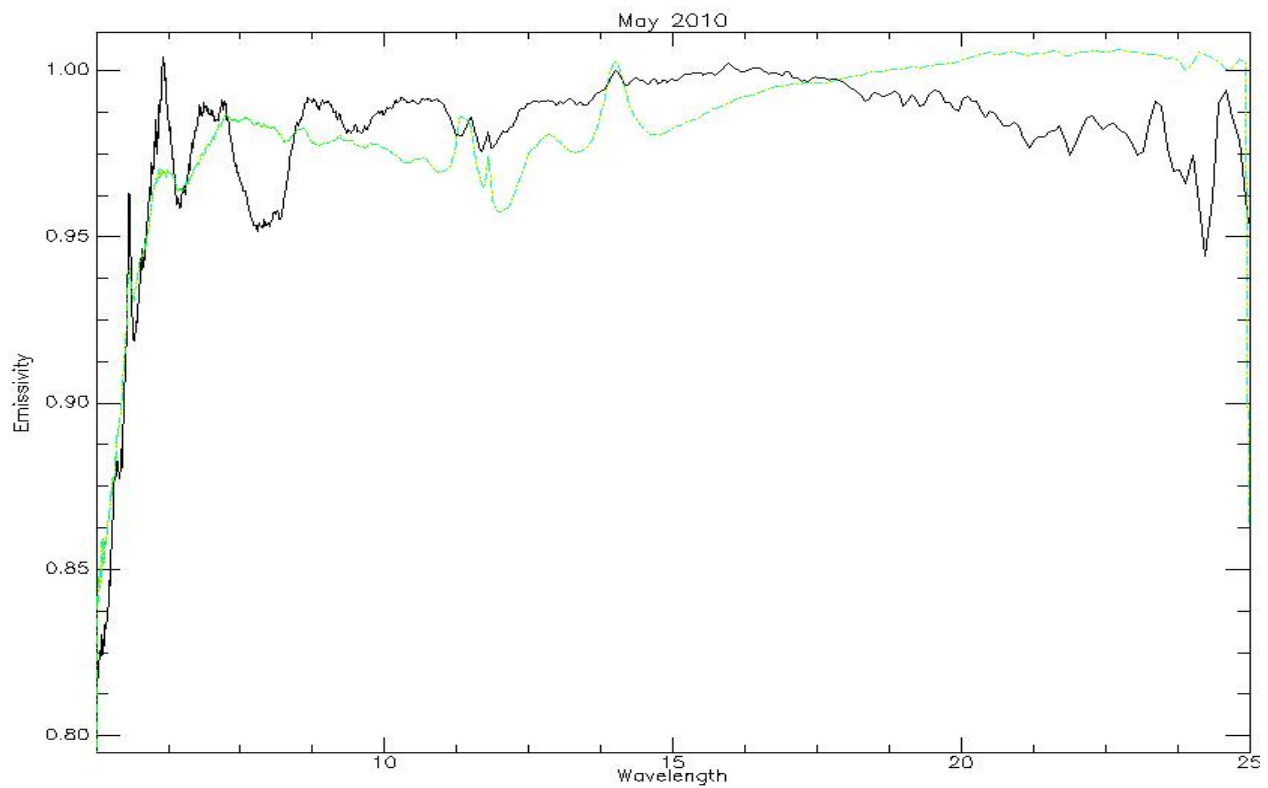


**Figure 3.28 Modeled spectral unmixing using all 28-end members. Despite the prominent quartz spectral feature in the May spectrum (solid line), the model did not identify quartz as an end member.**

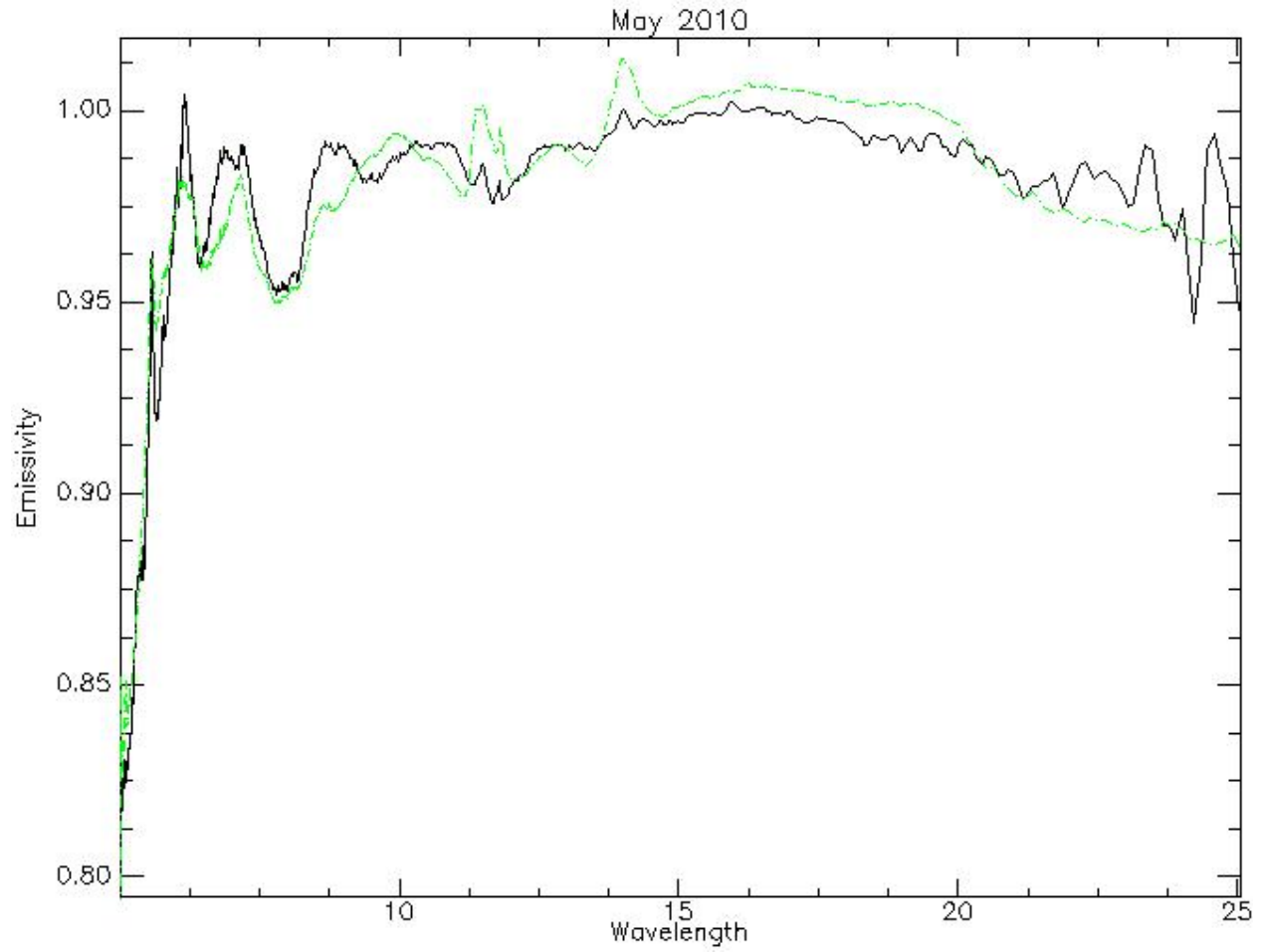


**Figure 3.29 Modeled spectral unmixing using end members from the ASU spectral library. Despite the relatively low RMS value of 0.0106, the modeled (dashed line) spectrum is off.**

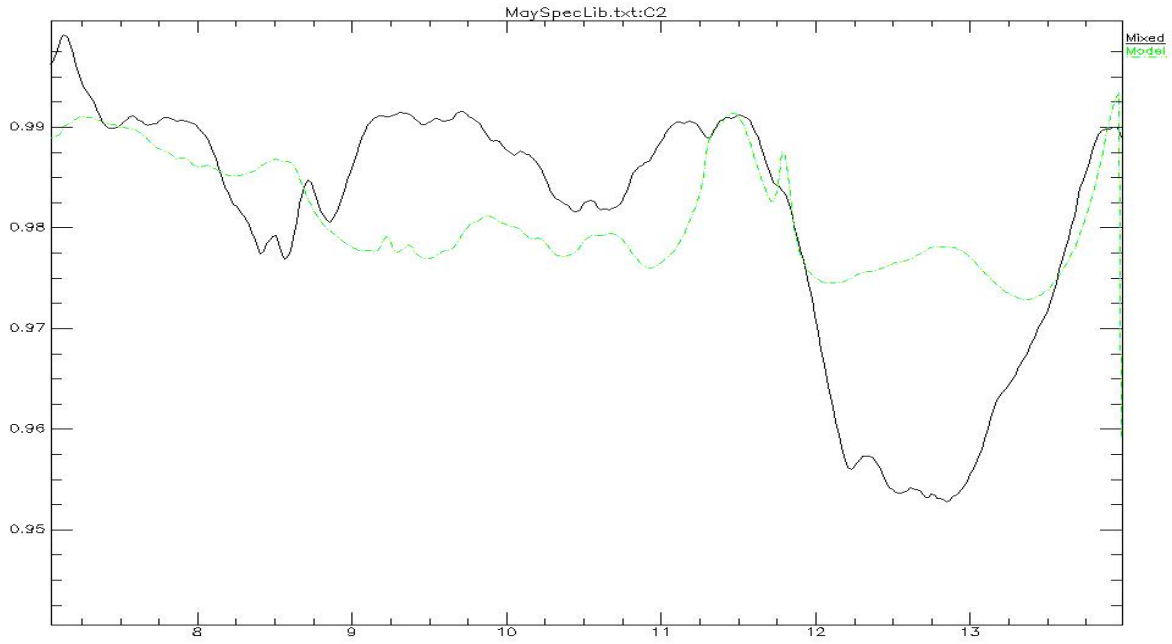


**Figure 3.30 Unmixing with C+K+Q end members produced a very poor compositional fit.**

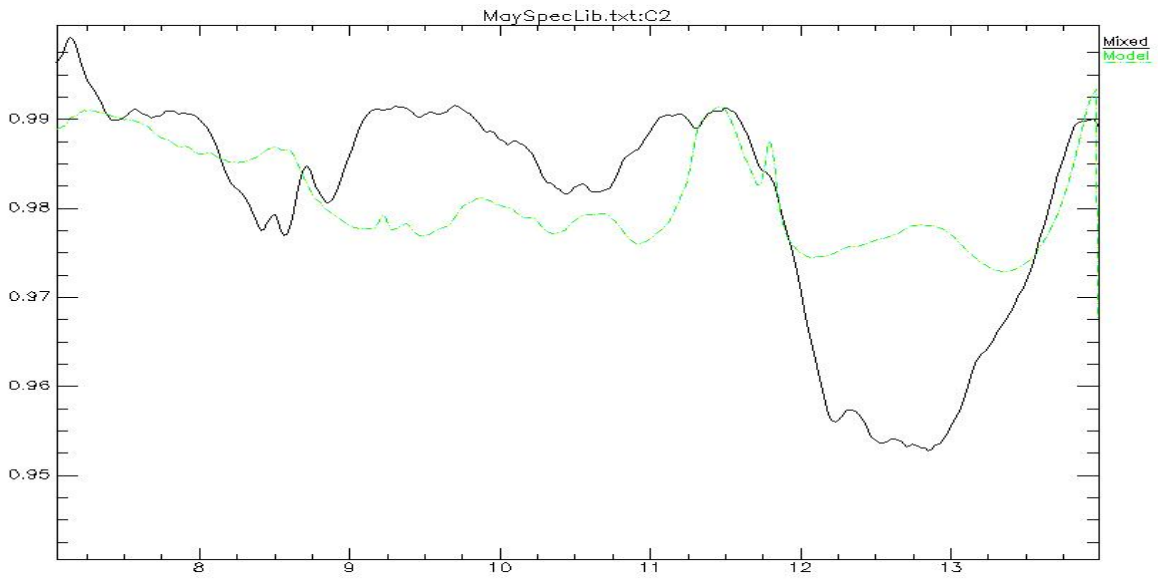


**Figure 3.31 Unmixing with C+Q end members produced similarly poor results as unmixing with C+K+Q.**

## July Spectrum

Running the unmixing using all 28 end members generated an RMS = 0.0164 and a composition estimation of 89.24% calcite (>45  $\mu\text{m}$ ) and 10.75% quartz (<10  $\mu\text{m}$ ). The modeled spectrum had an error of 1-3% (Fig. 3.32). Unmixing with the ASU spectral library produced an RMS = 0.0051, and a slightly better model fit in the 8-12  $\mu\text{m}$  wavelength region (Fig. 3.33). The composition unmixing results included 70.30% ilmenite, 19.39% magnesite, and 4.64% calcite. The third unmixing attempt used the C+K+Q spectral library, and yielded an RMS = 0.0244 and a composition of 65.25% kaolinite, 17.97% quartz (<10  $\mu\text{m}$ ), 11.29% calcite (<10  $\mu\text{m}$ ), and 5.47% quartz (10-20  $\mu\text{m}$ ). The model fit had 1- 4% error, and a high RMS value (Fig. 3.34). The final unmixing was performed with the C+Q spectral library, resulting in an RMS = 0.037 and a model fit with an error range of 2-5%, the highest range of all models (Fig. 3.35). Modeled composition included 58.58% quartz (<10  $\mu\text{m}$ ), 28.08% calcite (>45  $\mu\text{m}$ ), 11.58% quartz (20-40  $\mu\text{m}$ ), and 1.74% calcite (<10  $\mu\text{m}$ ).

## March Spectrum

Running the unmixing using all 28 end members generated an RMS = 0.0153, and a composition estimate of 67.93% dolomite (10-20  $\mu\text{m}$ ), 17.98% quartz (20-40  $\mu\text{m}$ ) and 14.07% forsterite (<2.7 $\mu\text{m}$ ). The modeled spectrum retained the general shape of the unmixed spectrum, although the major features of the spectrum had shifted by  $\sim 0.5$   $\mu\text{m}$  towards shorter wavelengths (Fig. 3.36). Unmixing with the ASU spectral library produced an RMS = 0.0018 and a composition of 61.18% ilmenite, 36.31 dolomite, and 1.84% apatite. The modeled spectrum had

a good fit between 8.5 and 11  $\mu\text{m}$ , with a decrease in the quality of the fit towards the edges of the spectrum (Fig. 3.37). A third unmixing attempt was made using the C+K+Q spectral library, resulting in an RMS = 0.0292 and a composition estimate of 68.67% kaolinite, 15.67% calcite (<10  $\mu\text{m}$ ), and 15.64% quartz (10-20  $\mu\text{m}$ ). With the exception of the quartz feature near 8.5  $\mu\text{m}$ , the model had an error range of 1-4% (Fig. 3.38). Finally, unmixing with the C+Q spectral library resulted in an RMS = 0.042 and a composition of 47.86% quartz (<10  $\mu\text{m}$ ), 25.57% calcite (<10  $\mu\text{m}$ ), 20.41% quartz (20-40  $\mu\text{m}$ ), and 6.14% calcite (>45  $\mu\text{m}$ ). As was the case with the modeled spectrum in the C+K+Q unmixing, the shallow quartz feature was the only good fit in the modeled spectrum, whereas the rest of the model had errors in the 2-8% range (Fig. 3.39).

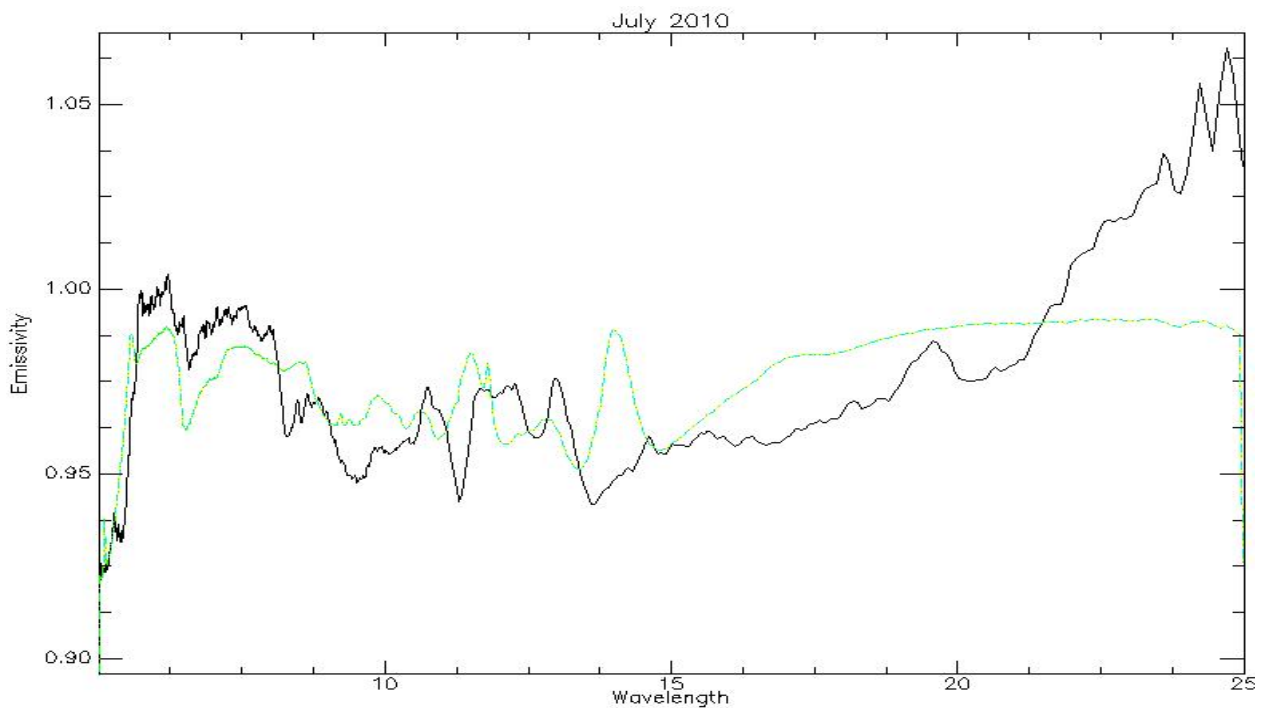


**Figure 3.32 Unmixing July storm spectrum with all 28-end member library did not result in a good model fit.**



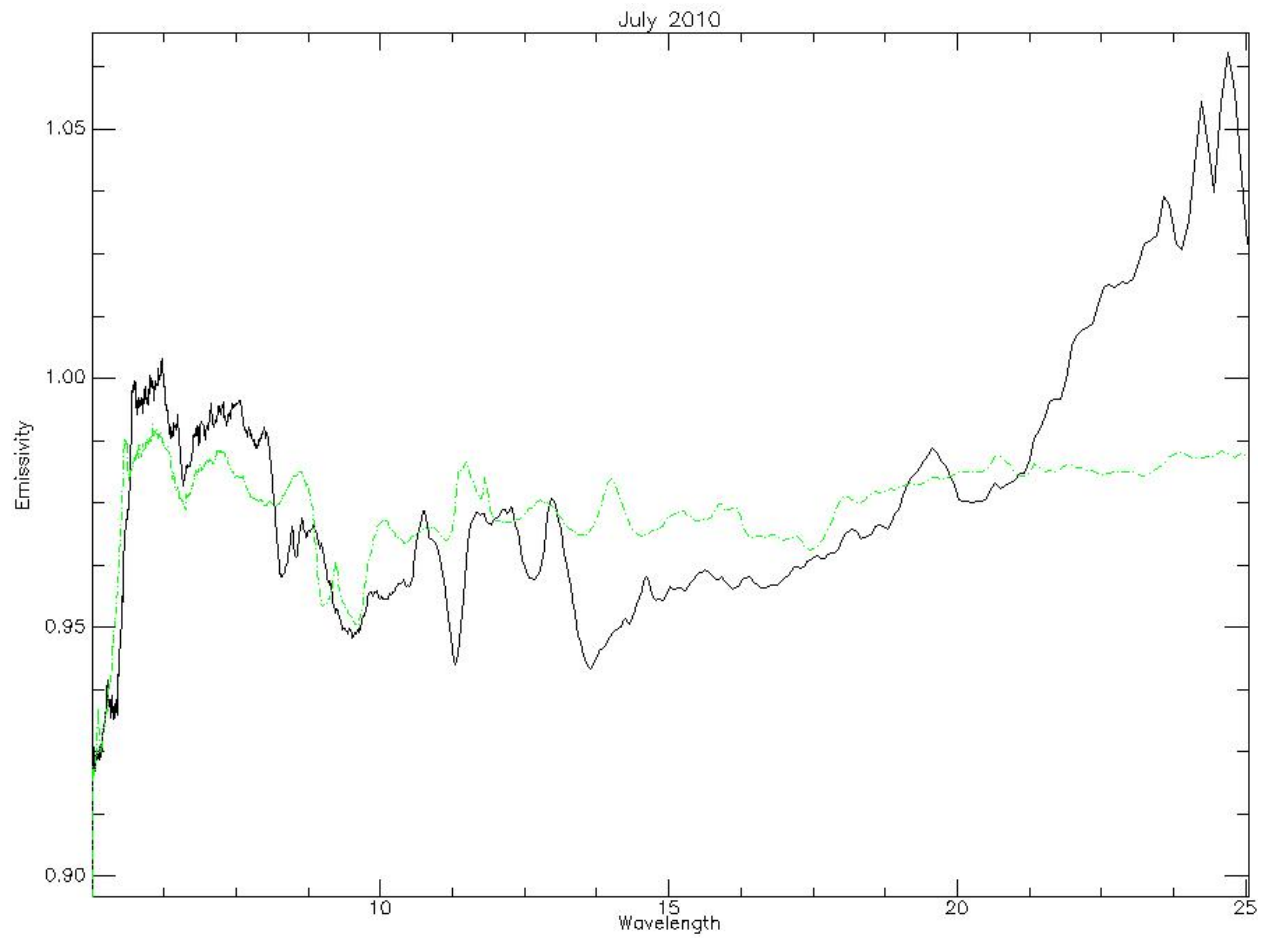


**Figure 3.33 Unmixing with ASU's spectral library had a relatively good fit in the 8-12  $\mu\text{m}$  region, whereas outside of that range the fit was poor.**

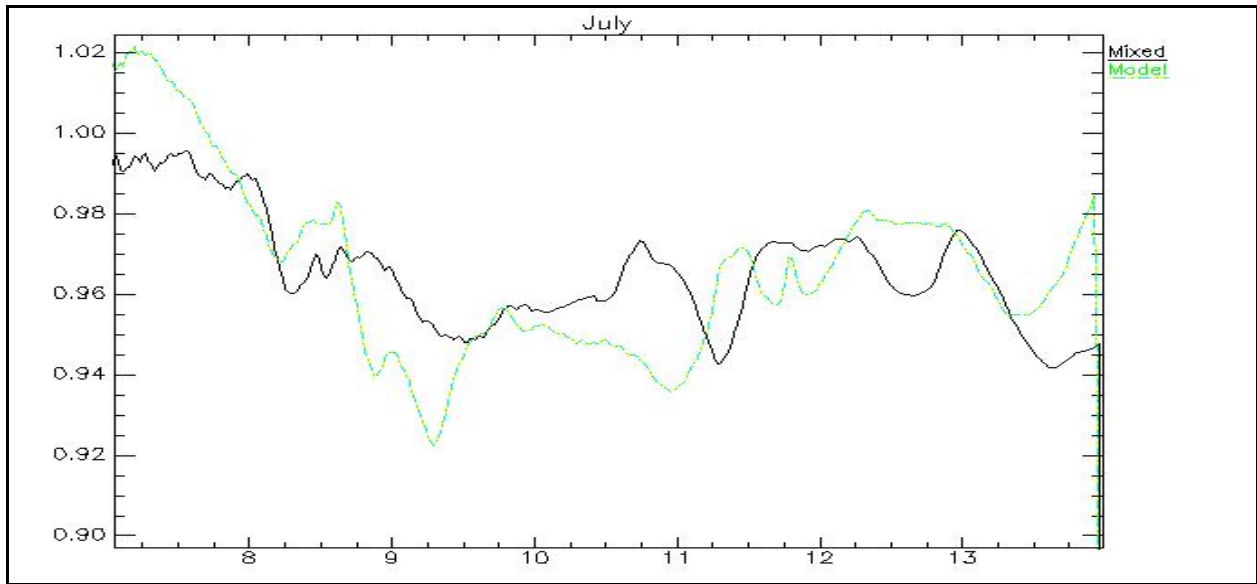


**Figure 3.34 Unmixing with C+K+Q end members produced a poor model fit.**

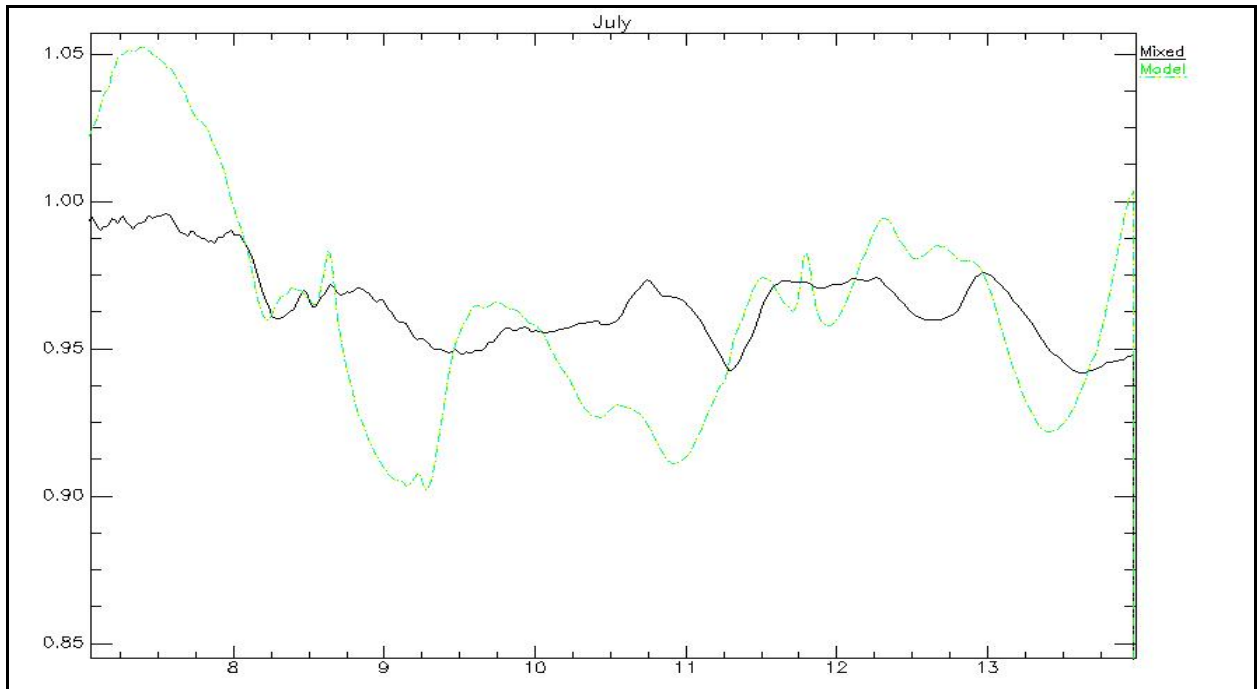


**Figure 3.35 Unmixing with C+Q end members resulted in a poor fit and a high RMS value**

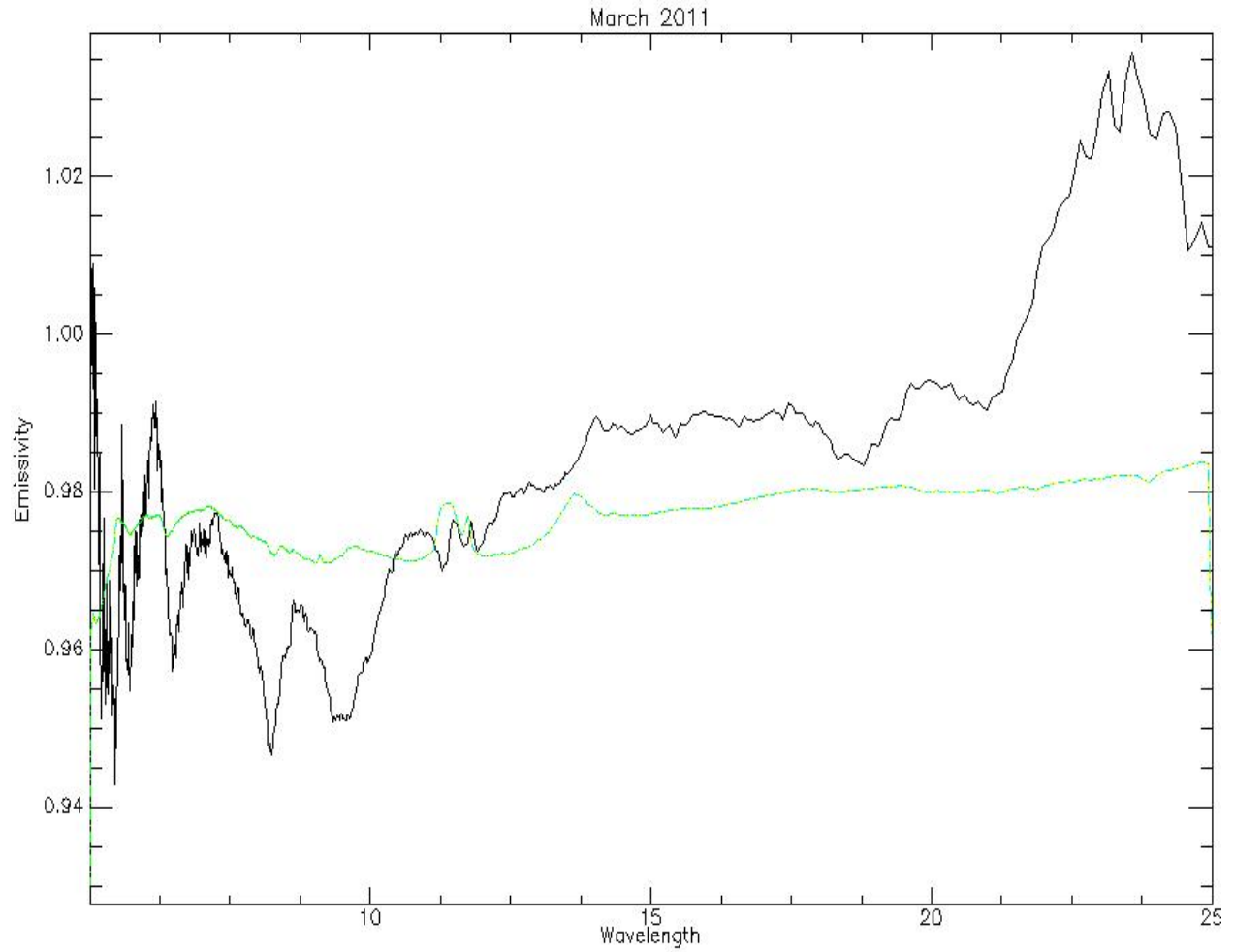


**Figure 3.36 Unmixing of March spectrum with all 28-end member library resulted in a low RMS value and the model retained most of the mixed spectral features, although they were slightly shifted to shorter wavelength.**

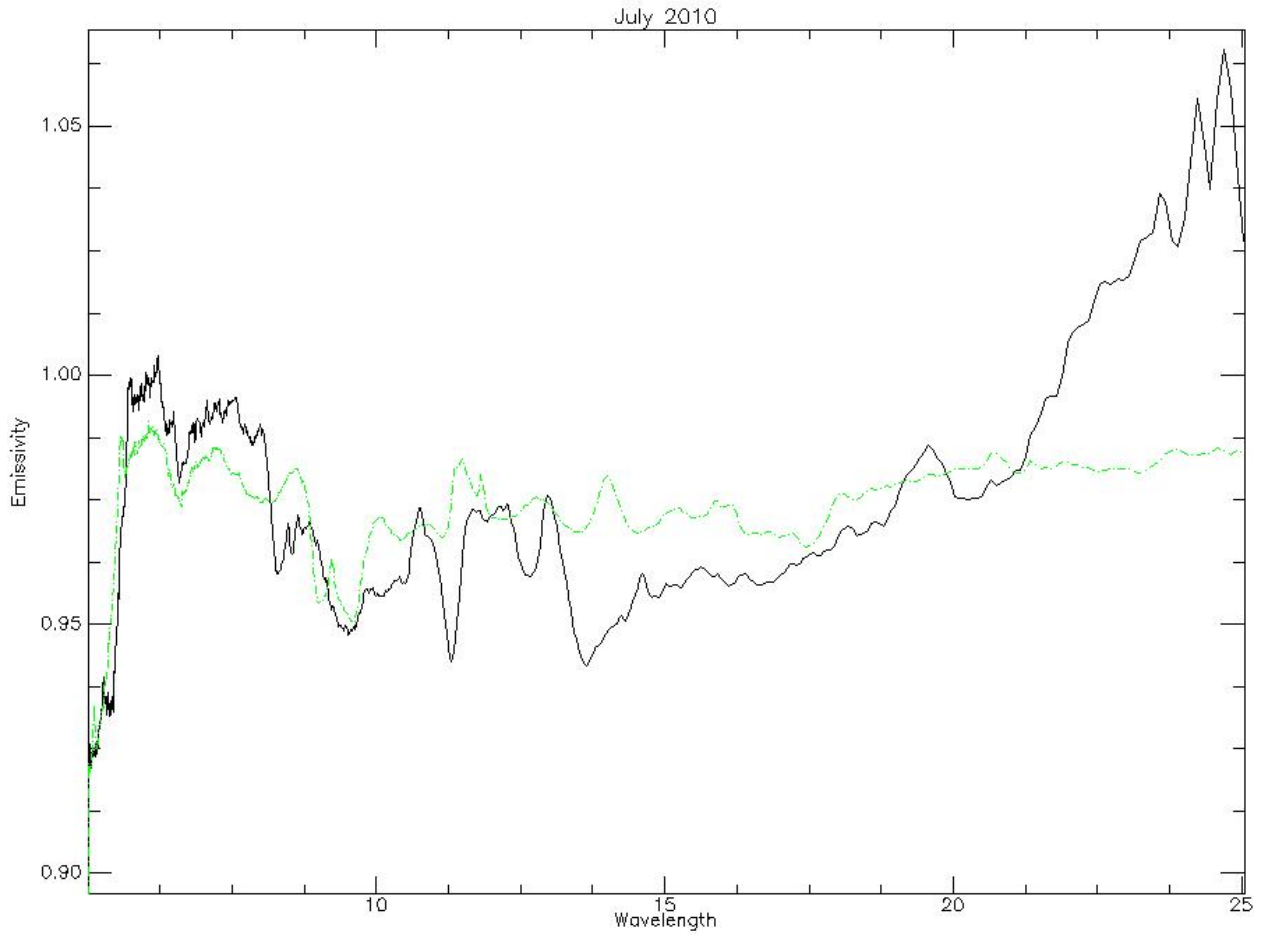


**Figure 3.37 Unmixing with ASU’s spectral library produced a good fit in the 8.5 – 11  $\mu\text{m}$ , with high errors outside of that region. Compositional end members identified were not accurate.**

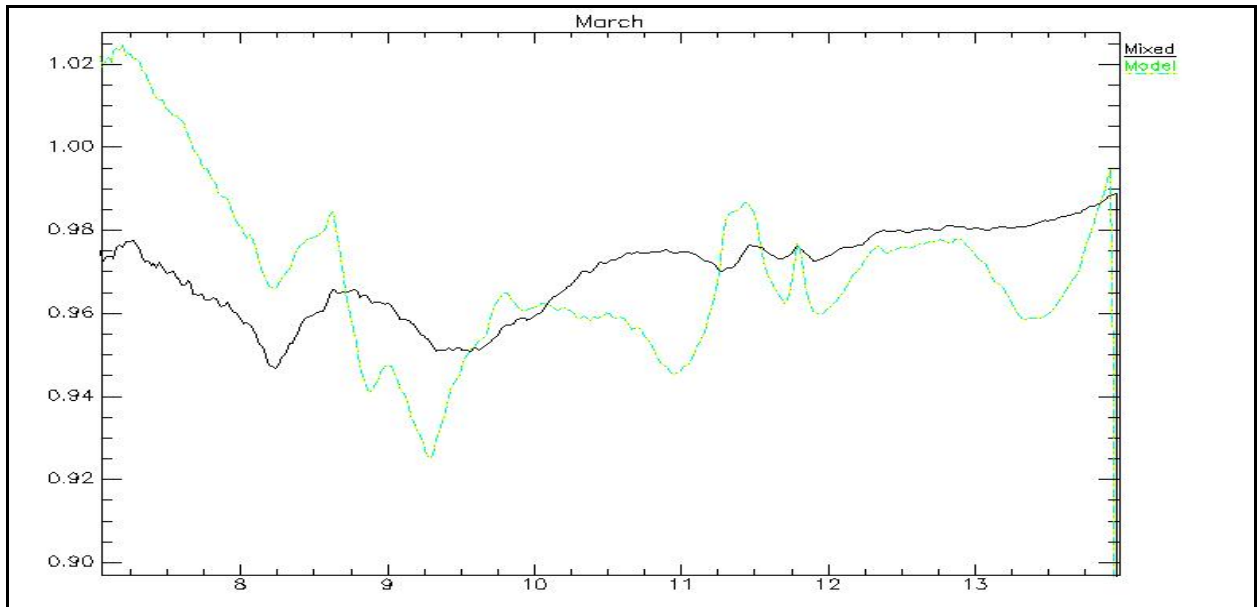


**Figure 3.38 Unmixing with C+K+Q end members produced a poor fit, whereas compositional results were relatively accurate and similar to XRD results.**

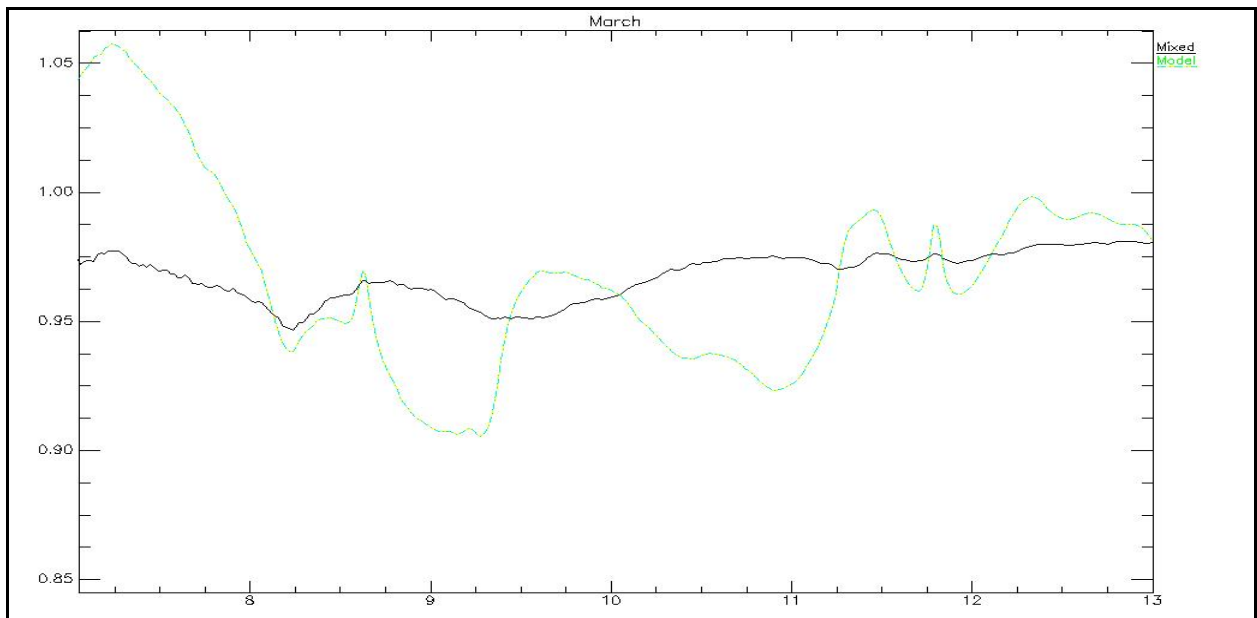


**Figure 3.39 Unmixing with C+Q end members produced a very poor fit, whereas the compositional results were similar to unmixing with C+K+Q and XRD results.**

Mixture Spectra:

As the dust spectral deconvolution results did not match the XRD and SEM findings, the spectral deconvolution results of known mixtures were crucial in assessing the validity of the model. Initial unmixing was performed using different particle sizes for calcite, forsterite, and quartz, resulting in 12 end members. This was followed by a second unmixing, where end members were restricted to minerals present in the mixtures and their associated particle sizes (calcite <10  $\mu\text{m}$ , forsterite and quartz 10-20  $\mu\text{m}$ ). The results of unmixing of spectral mixtures are in Table 3.4, figures 3.40-3.42 and Appendix C.

**Table 3.4 Spectral deconvolution results for calcite, quartz, and forsterite mixtures.**

<b>Mixture</b>	<b>No. of end members used</b>	<b>End members identified</b>	<b>Percentage %</b>	<b>RMS</b>
Calcite + quartz	12	Quartz (10-20 $\mu\text{m}$ )	67.03%	0.037
50:50		Calcite (20-45 $\mu\text{m}$ )	32.96%	
	2	Quartz (10-20 $\mu\text{m}$ )	66.58%	0.039
		Calcite (<10 $\mu\text{m}$ )	33.41%	
calcite + quartz	12	Calcite (20-45 $\mu\text{m}$ )	64.27%	0.038
75:25		Quartz (10-20 $\mu\text{m}$ )	35.72%	
	2	Calcite (<10 $\mu\text{m}$ )	64.93%	0.043
		Quartz (10-20 $\mu\text{m}$ )	35.06%	
Calcite + quartz	12	Quartz (20-40 $\mu\text{m}$ )	40.27%	0.039
+ forsterite		Calcite (<10 $\mu\text{m}$ )	24.45%	
31:31:38		Forsterite (10-20 $\mu\text{m}$ )	27.03%	

	Quartz (10-20 $\mu\text{m}$ )	10.75%	
	Calcite (<45 $\mu\text{m}$ )	7.47%	
3	Quartz (10-20 $\mu\text{m}$ )	54.40%	0.040
	Calcite (<10 $\mu\text{m}$ )	32.89%	
	Forsterite (10-20 $\mu\text{m}$ )	12.69%	

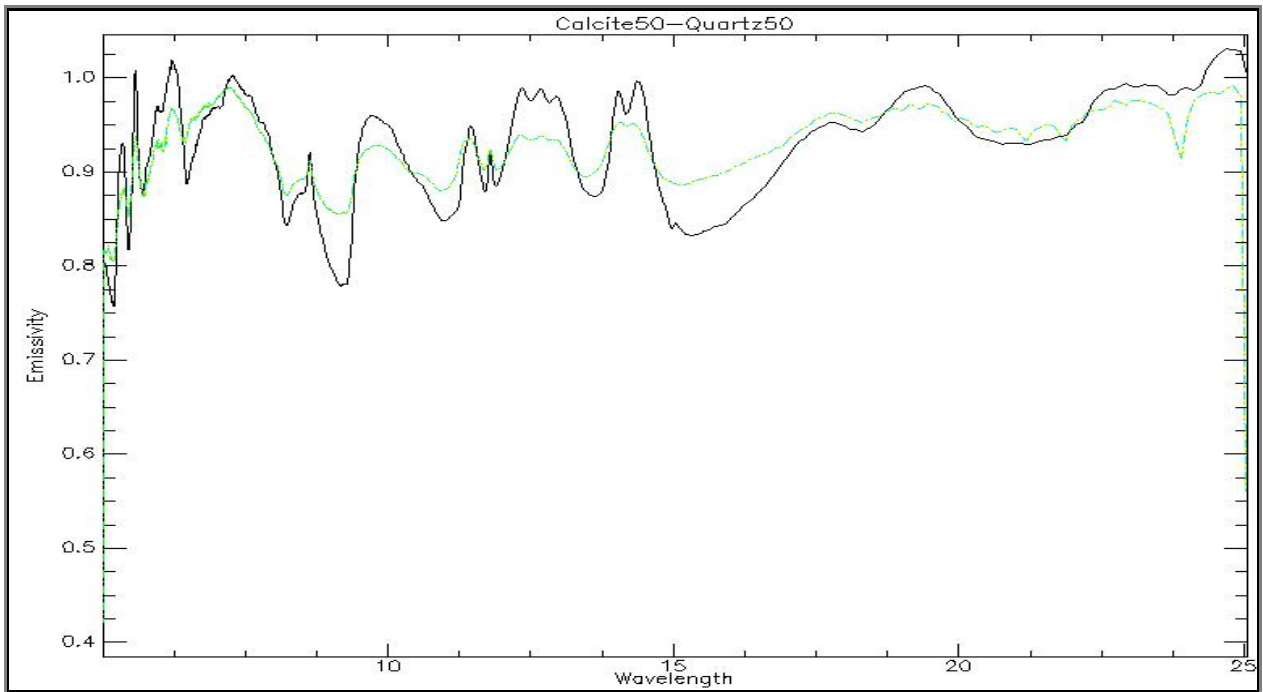


**Figure 3.40 Spectral deconvolution of a calcite and quartz 50:50 mixture using only 2 end members (calcite <10, quartz 10-20).**

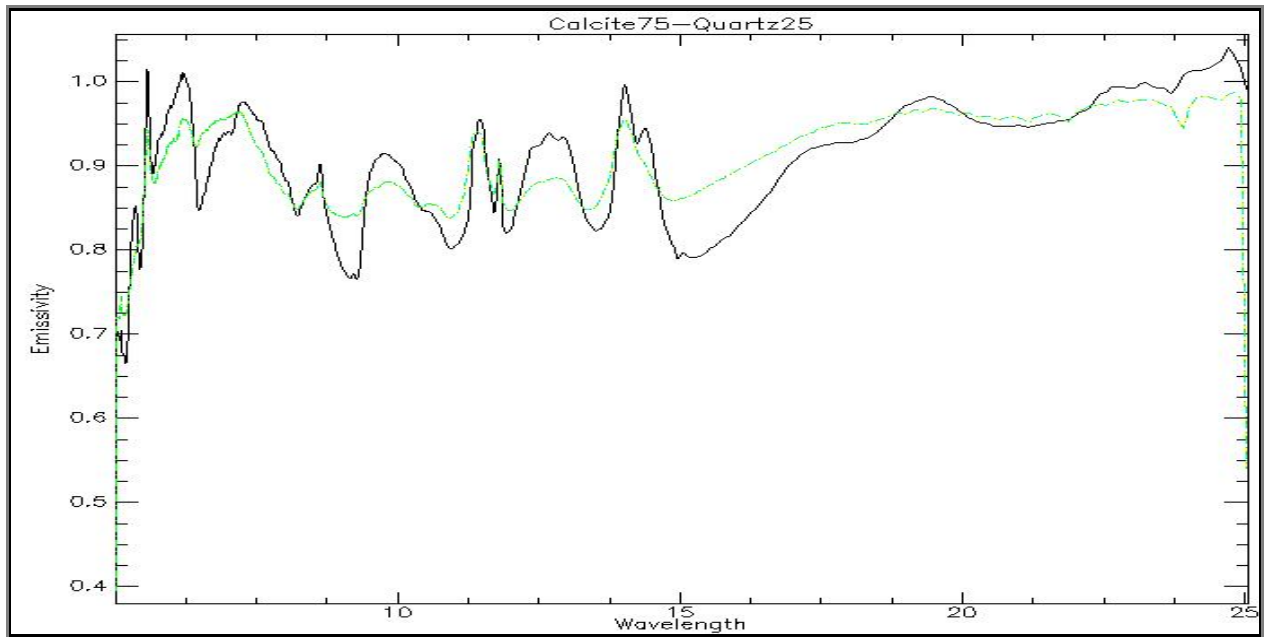


**Figure 3.41 Spectral deconvolution of a calcite and quartz 75:25 mixture using only 2 end members (calcite <10, quartz 10-20).**

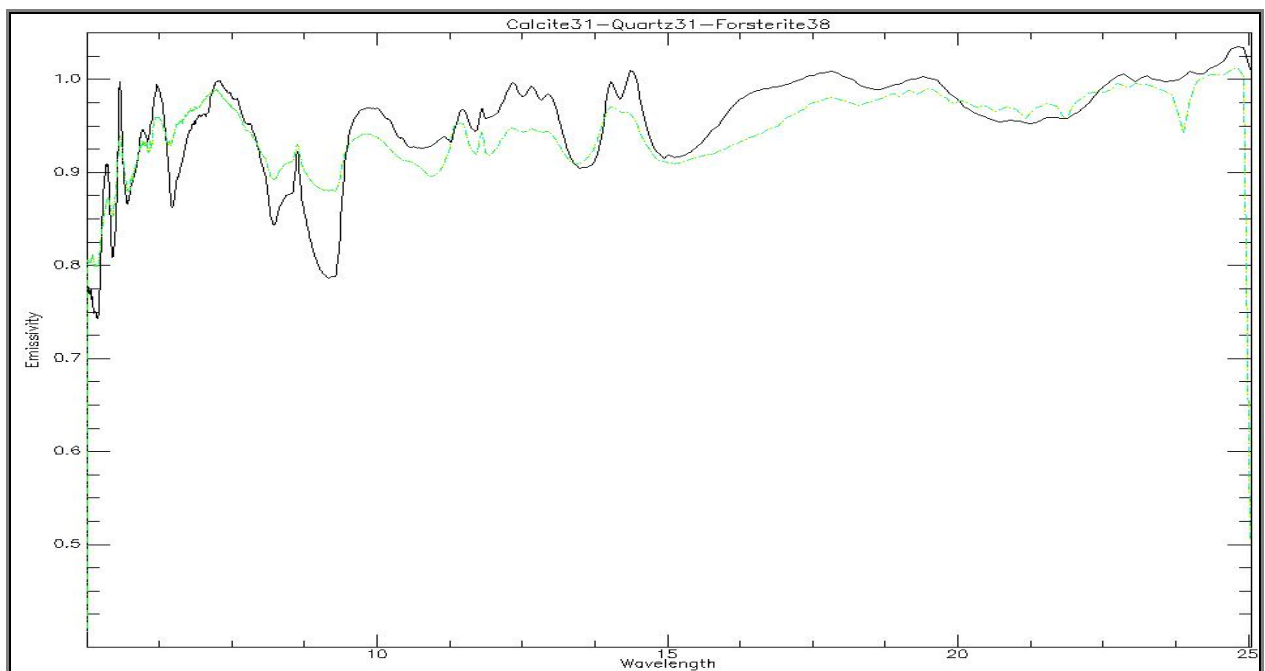


**Figure 3.42 Spectral deconvolution of a calcite, quartz, and forsterite 31:31:38 mixture using only 3 end members (calcite <10, forsterite and quartz 10-20).**



### 3.6 DISCUSSION

The fine spectral library end members were in general agreement with both ASU's spectral library and literature and retained the general spectral features of all minerals. The effect of decreasing particle size on the intensity of the emissivity troughs was evident, whereas an intensification of transparency features caused by volume scattering was also noted (Fig 3.35). These results were in agreement with the findings of Ramsey and Christensen (1998). Although these changes in band morphology were generally linear, minor non-linearity was observed and does not affect the overall results.

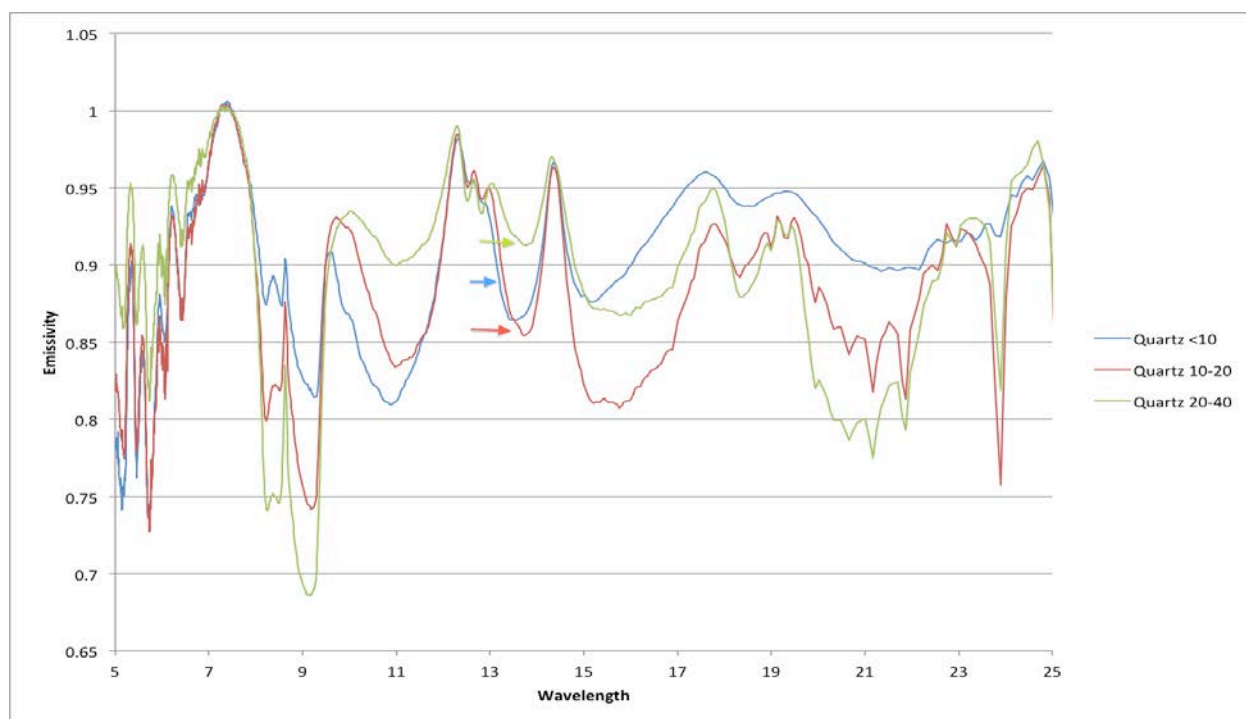


**Figure 3.43 Effects of volume scattering from smaller particles can be seen in the intensification of transparency feature troughs. Arrow point to the positions of each particle size fraction, and show that the smallest particle fraction had the deepest trough.**

Unmixing of dust spectra did not produce straightforward trends. The May spectra had the lowest model fit of any other dust spectra. Compositional results (end members present and percentages) were inaccurate and not in agreement with XRD findings. The discrepancy may be the result of changes in experimental conditions (e.g. humidity, temperature), as there was a temporal gap of over one year between dust sample analysis and mineral dust creation and analysis. Ramsey and Christensen (1998) noted that acquiring end member and mixture data on the same day reduces error significantly. Further, the number of scans performed on the May sample was 255, resulting in higher noise and a decrease in spectral resolution. The number of subsequent scans was increased to 1024, but the lack of sufficient sample size for that particular storm did not allow for a second spectroscopic analysis.

Unmixing the July spectra produced better results. The best model fit was obtained using the 28-end member spectral library created for this research. With the exception of quartz, the mineral composition was not in agreement with XRD findings. Other spectral unmixing attempts produced a better estimate of mineral composition, although they tended to over estimate the amount of quartz present and under estimate the amount of calcite. Similar results were obtained with the March spectra, where a low RMS value and better model fit did not translate into accurate compositional estimate.

Thomas et al. (1993) explain that surfaces with mixed composition result in radiation reflected with significantly different reflectance spectra, resulting in reststrahlen peaks of one mineral being reflected less strongly if it encounters another mineral particle that has a reststrahlen peak at a different wavelength. This can suppress an otherwise prominent reststrahlen band and cause under or over estimation by the model. Ramsey and Christensen (1998) concluded that the strongly absorbing portion of the emissivity spectrum had the largest

residual errors, as unmixing in this region becomes slightly nonlinear. They also noted the largest errors were associated with the strong absorption characteristics of quartz.

Solving for an unknown spectrum is a function of measuring the difference between two or more known end members. This assumption is only valid when the unknown spectrum is bounded by the known end members in emissivity space. The dust spectra had an upper emissivity boundary of  $\sim 1$  and a lower boundary of 0.94, whereas the mineral end members (with the exception of andesine, fayalite and kaolinite) had a lower emissivity boundary of 0.60. Consequently, the unknown end members will be outside of the known end members' boundary, resulting in less accurate predictions. This is evident in the over estimation of andesine, kaolinite, and fayalite, as the lower boundary of these end members is much closer to the dust samples. Additionally, the visual misfit of the model in comparison to the mixed spectra amounts to less than 2% (Ramsey and Christensen, 1998), deeming the results valid despite the visual discrepancy.

XRD and SEM results were not conclusive in terms of all end members present, as some minerals were not identified for reasons discussed in section 3.4.1. Further, the new fine spectral library is missing gypsum, Chlorite/Serpentine, and pure fayalite, and consequently, the model will attempt to compensate for the lack of these end members either by over or under estimating certain minerals, or by identifying other minerals that are not present in the dust sample.

The results of unmixing the three mixtures were not straightforward. The end members in all three mixtures were identified correctly. However, the percentages were not representative of the actual amounts used to create the mixtures, particularly in the calcite + quartz 50:50 mixture and the calcite + quartz + forsterite mixture (see Table 3.4). These findings validate the

model's ability to identify different end members correctly. Nonetheless, the model's ability to predict end member quantities is questionable.

### 3.7 CONCLUSION

Particle size plays a major role in spectral analysis, particularly in the  $< 60 \mu\text{m}$  fraction. Appropriate size fraction end members should be used for spectral deconvolution, and attention must be paid to their spectral range and resolution, as both can affect residual errors and introduce uncertainties. Lower RMS values are not an indicator of a correct compositional fit, as spectral features of certain minerals may be greatly affected by the presence of other minerals, resulting in either over or under estimation. Similarly, higher RMS values may not invalidate the results, and other parameters, such as end members identified and their concentration, must be considered when evaluating the outcome of the model.

A basic knowledge of the possible constituents of an unknown mixture is valuable and can help produce better predictions by increasing the number of end members in spectral deconvolution. The lack of gypsum, Chlorite/Serpentine, and pure fayalite end members in the new spectral library may have contributed to misidentification of mixed minerals or led to over or under estimation of other present end members. It is therefore important that those missing end members be incorporated into this library if further future analysis of the same dust samples is to be performed.

The spectral deconvolution model was generally accurate in identifying mineral end members present in the dust samples and the mixtures. However, it failed to accurately identify the percentages of these end members. Non-linear behavior with spectral deconvolution was

observed as a result of the fine-grained particle size. Consequently, restricting spectral deconvolution to the specific end members found in the mixed spectra did not eliminate this effect and produced inaccurate end member percentages. Nevertheless, the results obtained through spectral deconvolution with a fine-grained spectral library were more accurate and more representative of the mixed spectra than results obtained through large-grained spectral libraries, such as ASU's library. This demonstrates the importance of using a library with the correct particle size when performing spectral deconvolution on mixed spectra.

## **4.0 THERMAL INFRARED REMOTE SENSING OF DUST STORMS IN THE MIDDLE EAST**

### **4.1 INTRODUCTION**

A great deal of interest had been expressed to studying eolian processes in general and dust storms in particular. Dust storms have far reaching impacts (see section 2.3.3) that extend to non-arid regions, such as northern Europe and Canada (Goudie and Middleton, 2006). Therefore, it is important to understand the processes that initiate, transport, and sustain dust storms, in addition to identifying source areas or dust hotspots. Remote sensing offers indispensable tools that allow for observing, gathering information, and characterizing dust storms. The purpose of this study is to utilize the thermal infrared (TIR) capabilities of both ASTER and MODIS data to accurately describe the dust content (particle size and mineral composition) of storms affecting Kuwait, and potentially establish a link to areas that may be identified as dust sources affecting that region.

### **4.2 BACKGROUND AND PREVIOUS WORK**

Numerous models and algorithms had been developed to characterize dust. Both the Total Ozone Mapping Spectrometer (TOMS) and the Atmospheric Infrared Sounder (AIRS)

instruments measure global aerosol thickness and depth to identify dusty regions (Chiapello et al., 2005, Engelstaedter et al., 2007, Strow et al., 2003, Pierangelo et al., 2004). Other studies, such as Engelbrecht et al. (2009) and Erell et al. (1999) have utilized conventional geochemical analytical tools, such as X-ray Diffraction (XRD) or Scanning Electron Microscope (SEM) to quantify the mineral composition and properties of dust aerosols. More recently, the effects of dust plumes on radiative forcing and possible connections to upper atmospheric temperature changes have been examined (Scheidt, 2009). This study will attempt to utilize the TIR capabilities of two satellite instruments, ASTER and MODIS, to analyze satellite data pertaining to three dust storm samples that were acquired over a period of one year from Kuwait. Results will be evaluated based on particle size and mineral compositions identified in comparison to previous XRD, SEM, and spectroscopic analyses.

Radiation emitted from a surface is a function of temperature and emissivity, and therefore, the temperature of the surface must be known to determine emissivity (Thomson et al., 1993). However, emissivity is also related to reflectance, as explained by Kirchhoff's law:

$$E = 1 - R, \quad (1)$$

where  $E$  = emissivity and  $R$  = reflectance (Salisbury et al., 1992). This assumption holds true only under isothermal conditions, and therefore, atmospheric conditions and downwelling from the atmosphere must be corrected (Salisbury et al., 1992, King et al., 2004). Both ASTER and MODIS data used for this study have undergone atmospheric correction upon acquisition (Levy et al., 2003), thus eliminating the need for further corrections.

Changes in emissivity are indicators of changes in composition and therefore geologic studies are less concerned with absolute temperature (Kearly et al., 1993). Mineral aerosols can be difficult to detect over arid regions, particularly when the aerosol content is similar to the

background. Therefore, changes in temperature were examined as means for separating dust plumes from background or clouds. On average, eolian surfaces have temperatures over 300 K, whereas clouds are much cooler at  $< 250$  K. Dust plumes are cooler than their surroundings yet warmer than clouds, and typically have temperatures  $\sim 280$  K, depending on the thermal properties of the mineral content (Baddock et al., 2009, Levy et al., 2003).

## **4.3 METHODOLOGY**

### **4.3.1 Forward and Back Trajectory Models**

Hybrid Single Particle Lagrangian Integrated Trajectory (HYSPLIT) is a model that simulates air parcel trajectories for dispersion and deposition using a set of algorithms and meteorological data. It is a joint effort between the National Oceanic and Atmospheric Administration (NOAA) and the Australian Bureau of Meteorology (Stunder et al., 2010). The model can perform forward or backward trajectory models. Both models have similar parameters, where the user defines the starting point (forward trajectory) or the ending point (backward trajectory). This point can either be chosen from a predefined list of global meteorological stations, or by entering the coordinates manually for a known area of interest. Once a starting or ending point is defined, the user chooses the day and time (UTC), and specifies the number of hours needed for tracking the air parcel either forward or backward. This is a subjective step that depends on the end user's objectives and knowledge of certain climatic events, such as dust storms. Finally, the user can define up to three different elevations where air parcels can be tracked, and the lowest default elevation value is 500 meters.



The first step in identifying possible dust hotspots affecting Kuwait included creating a back trajectory model, with Kuwait being the end point. A back trajectory model was created for each dust storm, with a total run time range between 48 to 96 hours. Deciding the number of hours was based on satellite image observations of dust plumes before they reached Kuwait, with each storm having different sets of weather mechanisms, making each storm unique. The model allows for up to three different elevations to be specified by the end user, and based on prior knowledge of the extent of these storms, elevations chosen were 500, 1000, and 3000 m respectively. The default minimum elevation of 500 meters was maintained, as air parcels near the surface can be affected by changes in ground temperature due to solar radiation or urban effects. Figures 4.1, 4.2, and 4.3 show the findings of the HYSPLIT model.

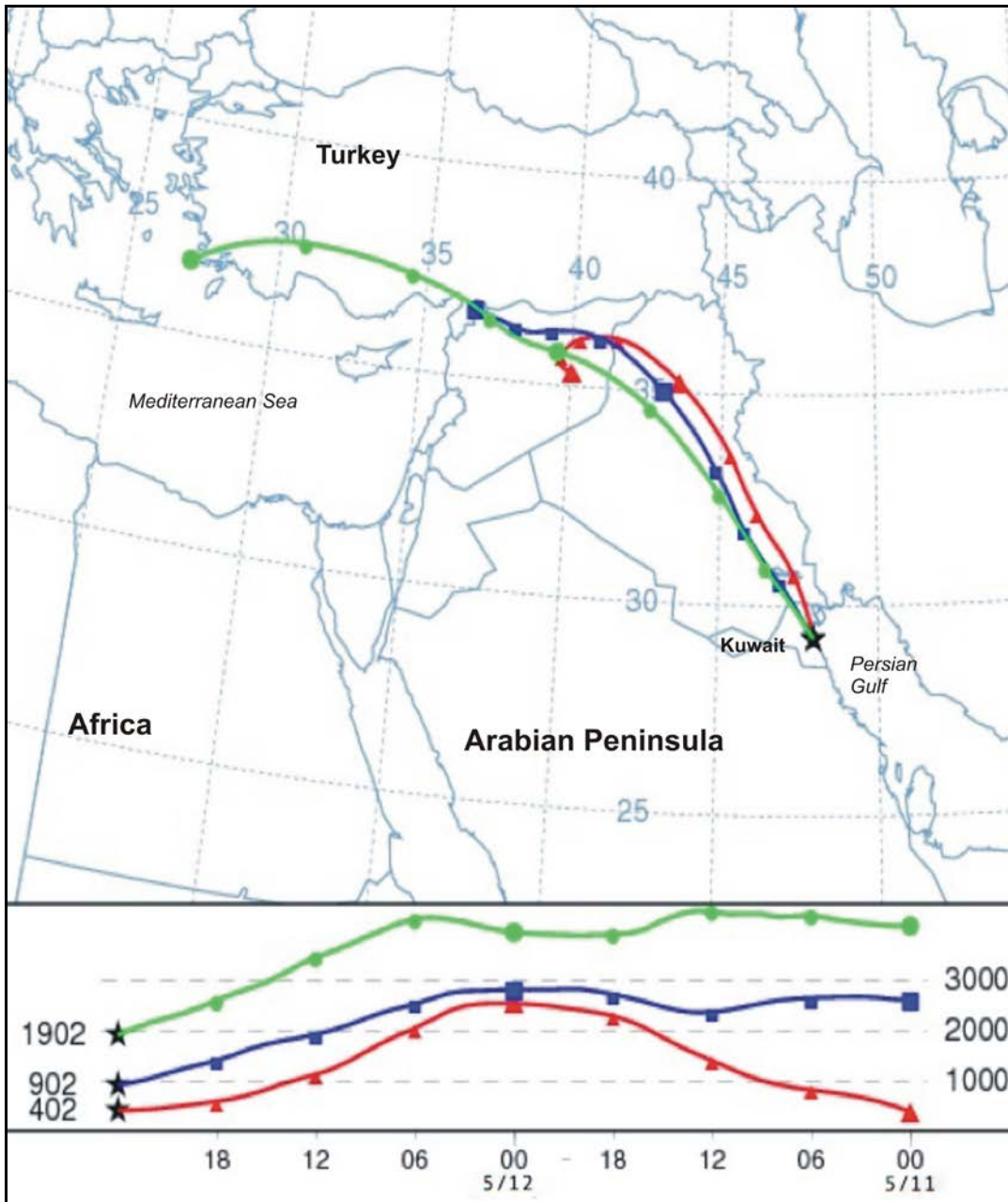


Figure 4.1 HYPSLIT back trajectory model results at different elevations starting over Syria and Southern Turkey beginning May 11, 2010 and ending 48 hours later in Kuwait (black star). Red = 500 m, blue = 2000 m, green = 3000 m.

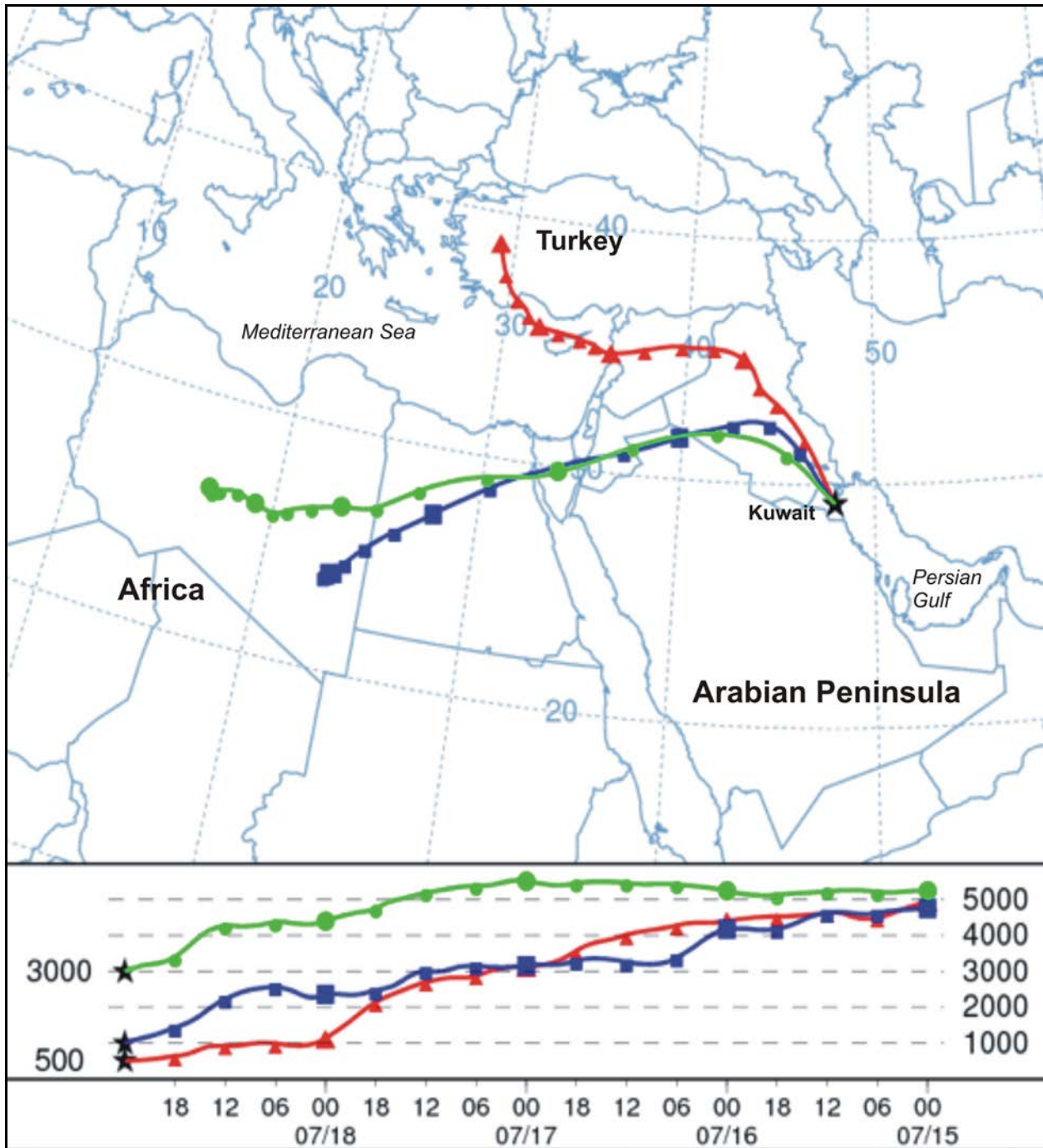


Figure 4.2 HYP SLIT back trajectory model results at different elevations starting over Turkey and Northern Africa beginning July 15, 2010 and ending 96 hours later in Kuwait (black star). Red = 500 m, blue = 2000 m, green = 3000 m.

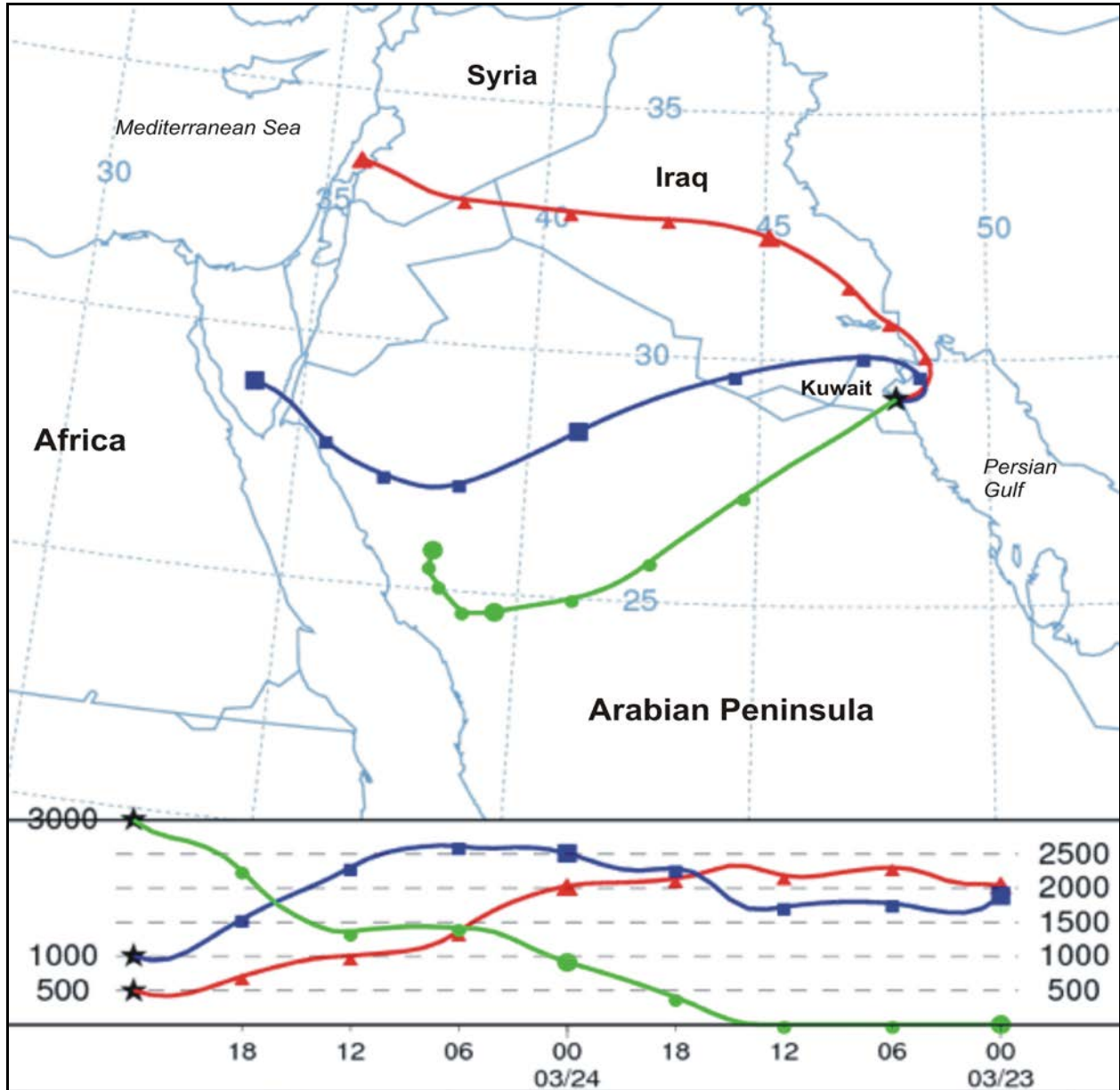


Figure 4.3 HYPPLIT back trajectory model results at different elevations starting over Syria (2000 m), Sinai desert (2000 m), and Saudi Arabia (surface level) beginning March 23, 2011 and ending 48 hours later in Kuwait (black star). By far this is the most complex of all three models. Red = 500m, blue = 2000m, green = 3000m.

Two of the three back trajectories had a path that went over eastern Syria and Iraq, further confirming that both areas are potential dust hot spots. The back trajectory model for March was more complex, with western Saudi Arabia (3000 m) and the Sinai Peninsula (1000 m) identified as other hot spots. The western coast of Saudi Arabia is dominated by volcanic deposits (Pollastro et al., 1997) and therefore that region can be eliminated. The Sinai Peninsula was not identified as a dust source in eolian literature, and therefore that area can also be eliminated. Further, the 500 m trajectory shares a similar path with the other models, thus it was deemed the likely path taken by the air parcels. All trajectory models agree for the lower altitude air masses, with most dust entrainment and transport occurring in lower altitudes.

To validate the results of the back trajectory models, forward trajectory models were created, with one hot spot in eastern Syria ( $36^{\circ} 10' N$ ,  $39^{\circ} 11' E$ ) defined as the starting point. This hot spot was chosen based on prior satellite observations, showing a dust plume over that area on May 11, 2010, before reaching Kuwait 72 hours later. With the exception of May, the July and March forward trajectories had a path that went over Iraq and reached Kuwait (Figures 4.4, 4.5, 4.6). MODIS satellite data of the region prior and during the May 2010 dust storm showed a dust plume originating in eastern Syria and following the same trajectories outlined by the forward and backward models over Iraq before reaching Kuwait (Fig. 4.7).

A world soil map (Fig. 4.8) shows that areas of eastern Syrian and western Iraq have calcite and gypsum rich soils. Specifically, the second hotspot is dominated by calcic xerosols, with pockets of gypsic xerosols, further confirming that the dust source of these storms was eastern Syria and western Iraq.

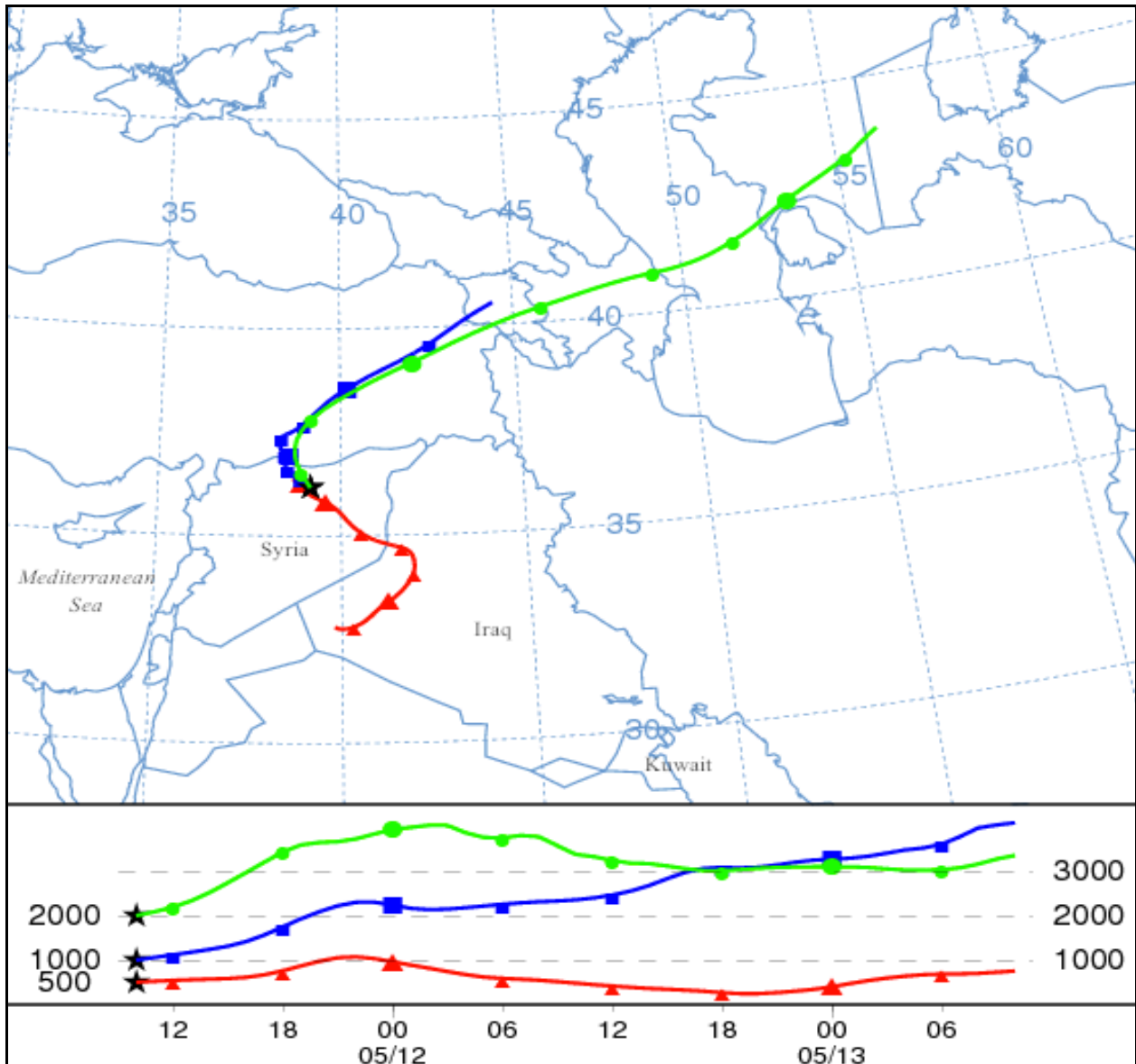


Figure 4.4 HYP SLIT forward trajectory model results at 500, 1000, and 2000 m elevations starting over hotspot in eastern Syria beginning May 11, 2010 and ending 48 hours later over Iraq, Turkey, and Russia. Red = 500 m, blue = 2000 m, green = 3000 m.

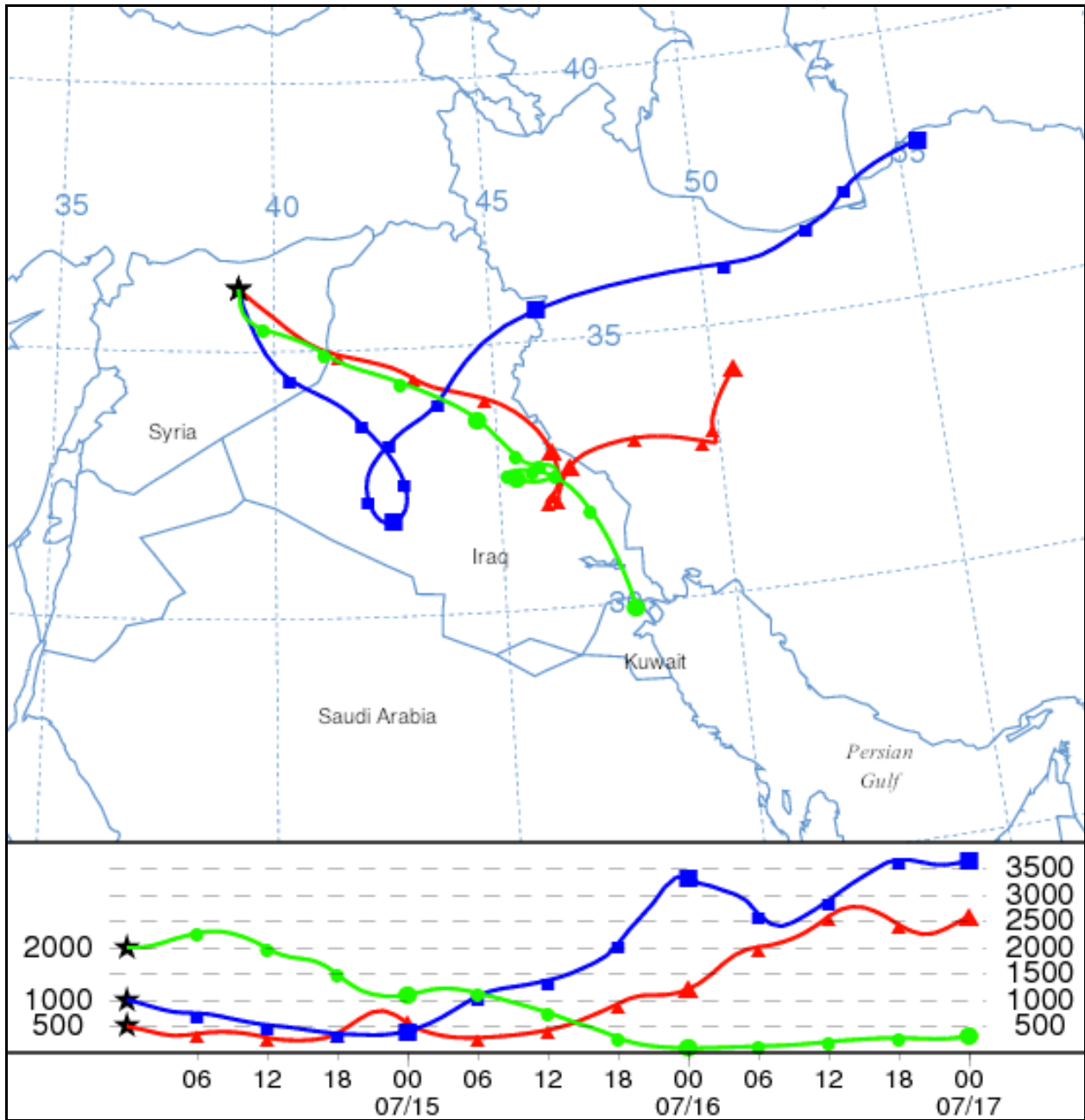


Figure 4.5 HYP SLIT forward trajectory model results at 500, 1000, and 2000 m elevations starting over hotspot in eastern Syria beginning July 14, 2010 and ending 72 hours later over Iraq, Iran, and Kuwait. Red = 500 m, blue = 2000 m, green = 3000 m.

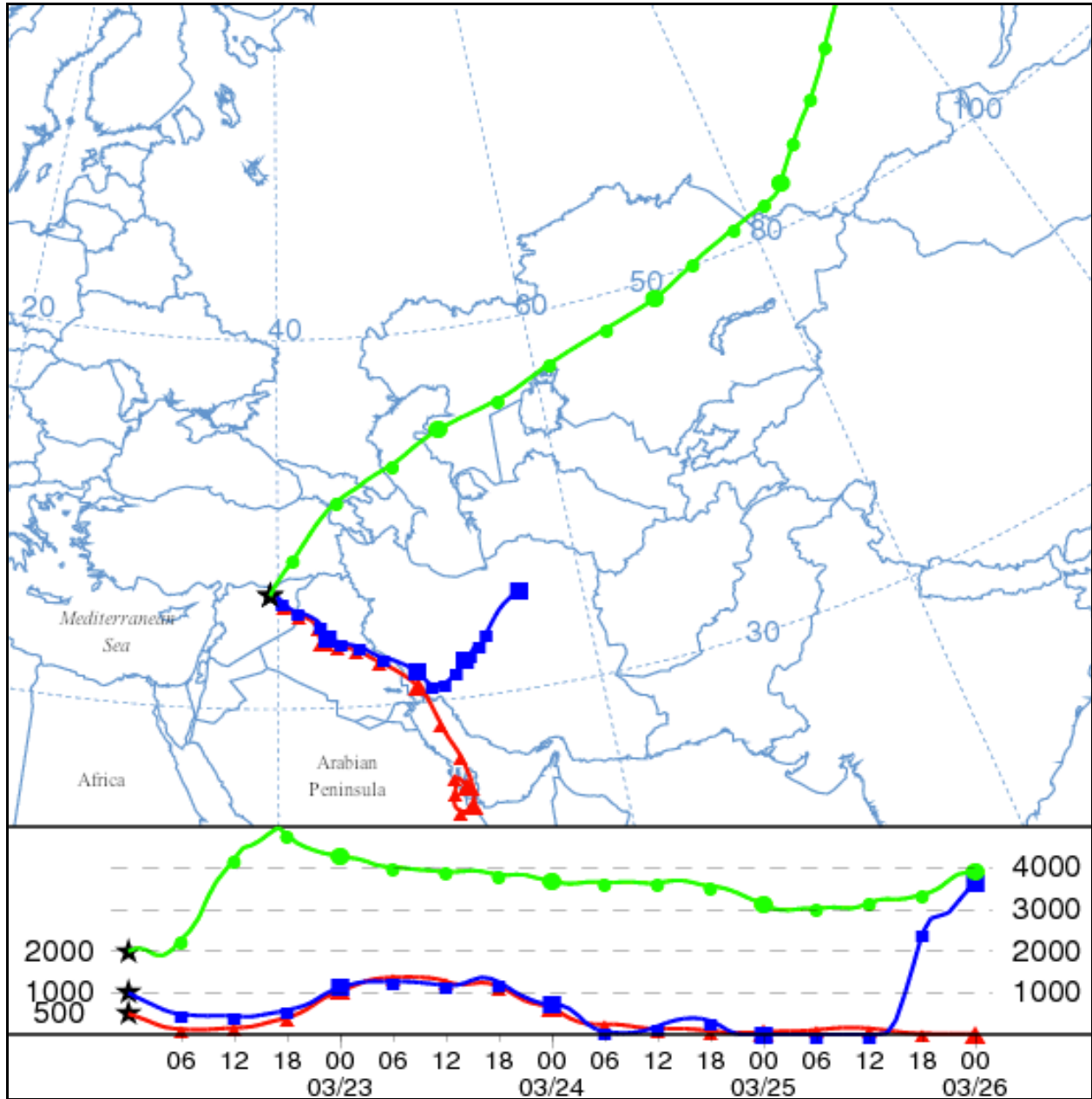
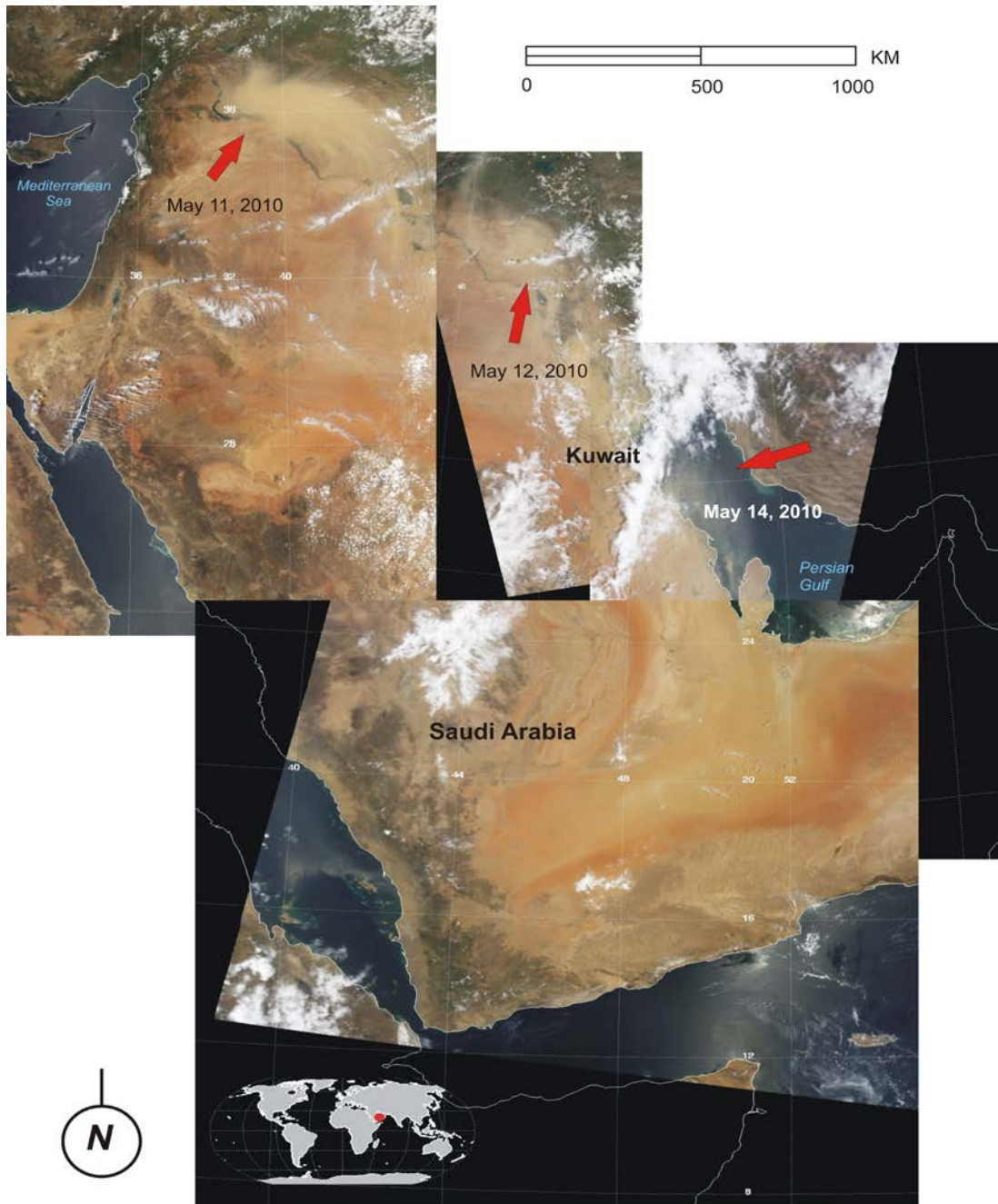
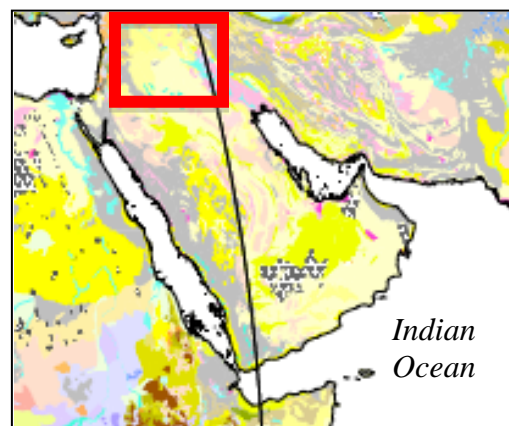
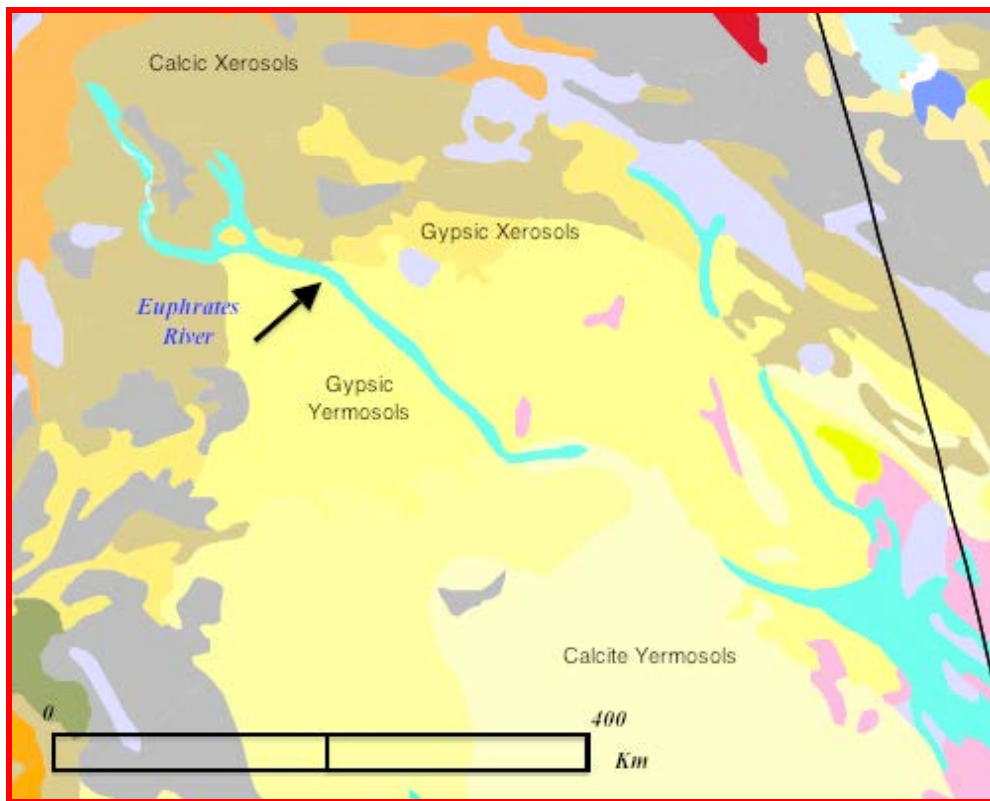


Figure 4.6 HYPSLIT forward trajectory model results at 500, 1000, and 2000 m elevations starting over hotspot in eastern Syria beginning March 22, 2011 and ending 96 hours later over Iraq, Iran, Persian Gulf, and Russia. Red = 500 m, blue = 2000 m, green = 3000 m.





**Figure 4.7 MODIS satellite data of the region prior to and during the May 2010 dust storm shows a dust plume originating in eastern Syria and following the same trajectories outlined by the forward and backward models over Iraq before reaching Kuwait (modified from <http://modis-atmos.gsfc.gov>).**



**Figure 4.8 World soil map showing high concentrations of calcite and gypsum in the soils of the hotspot (modified from FAO soil map).**

### **4.3.2 Satellite Data Acquisition**

A combination of Advanced Spaceborne Thermal Emission and Reflection (ASTER) and Moderate Resolution Imaging Spectroradiometer (MODIS) data were used for the purpose of this research. ASTER was launched in 1999 on board NASA's Terra satellite, and it has five TIR bands with a spatial resolution of 90 m (Hulley et al., 2011). The relatively high resolution of ASTER's TIR data is an advantage, however, a repeat time of 16 days and inconsistencies in data acquisition over the study area translated to the absence of any data corresponding to dust storm events in question. In addition to being on board the same satellite, the TIR products of ASTER and MODIS are believed to be reasonably compatible in semi-arid regions (Akhoondzadeh et al., 2008, Hulley et al., 2011), and therefore, MODIS was the primary data used. First launched on board the Terra satellite in 1999 and later on board the Aqua satellite in 2002, MODIS has 16 TIR bands and a resolution of 1 km. Between Aqua and Terra, MODIS provides global coverage 4 times a day (Levy et al., 2003), resulting in high temporal coverage and abundance of data. Data for both instruments were acquired through the NASA Land Processes Distributed Active Archive Center's (LP DAAC) web site.

ASTER has a wide range of data products from digital elevation models (DEM) to surface reflectance in the visible and near infrared (VNIR) regions. ASTER uses a temperature/emissivity separation algorithm to derive emissivity and surface temperature (Gillepsie et al., 1998), and produces AST\_05 surface emissivity and AST\_08 surface kinetic temperature products. Both types of data are key components in analyzing spectra for mineral abundance and dust plume vs. cloud discrimination in satellite images and were therefore used

for analysis. ASTGTM DEM data was also incorporated into the analysis to account for topography of hotspots. Atmospheric correction is automatically applied when generating level 2 products (Levy et al., 2003), thus eliminating the need for correction by the end user.

Although MODIS has an emissivity product in levels 2 and 3, it was decided to use the level 1B calibrated radiance data, as it contained a higher number of bands (16 bands compared to only 2 bands in the emissivity product). This allowed for more flexibility in data analysis, where radiance data can be used to derive emissivity and surface temperature, in addition to increasing accuracy in mineral identification by reducing the number of unknowns.

The criteria for selecting satellite data is outlined in Table 4.1, and depended on the results of the back trajectory models (described in section 4.5.1) and the dust samples collected from the study area.

**Table 4.1 Type, criteria, and purpose for selecting satellite data for analysis.**

Data Type	Criteria	Time	Purpose
MODIS L1B	Clear	Summer months (cloud-free)	Decorrelation stretch and unmixing of surface material to identify dust “hotspots”.
MODIS L1B	Dusty	May + July 2010, March 2011	Comparison with dust storm samples collected from field.
ASTER L2 AST_05, ASTGTM	Clear	Summer months (cloud-free)	For areas identified as dust “hotspots” by clear MODIS and back trajectory models, surface material analyses

ASTER L2 AST_05, AST_08	Dusty	May + July 2010, March 2011	(AST_05), and digital elevation models (DEM)(ASTGTM). Comparison with dust storm samples collected from field (AST_05), distinguishing clouds from dust plumes (AST_08).
----------------------------	-------	--------------------------------	--

---

### 4.3.3 Processing of Satellite Data

Clear MODIS scenes were used to examine surface lithology and pick potential hotspots based on their composition and the forward and back trajectory models. Using a conversion kit for the ENVI software, MODIS radiance data were geo-referenced (WGS-84) and converted to reflectance values. Solving for emissivity requires making 1 assumption to solve for the other unknowns, as defined by the Planck equation (Ramsey et al., 1999, Kealy et al., 1993). An assumed emissivity value of 0.98 was used to separate emissivity and temperature using the emissivity normalization method. A decorrelation stretch was applied to enhance the emissivity data and highlight variation in surface lithology (Gillespie et al., 1986). Decorrelation stretching is a technique that transforms highly correlated TIR data by removing the correlation, thereby allowing for subtle variations to be more visible (Katra and Lancaster, 2008, Vaughan et al., 2005).

A combination of bands 32 (red), 31 (green) and 29 (blue) was plotted. Red areas are interpreted as being quartz rich, green as granitic or vegetation, and blue being mafic or carbonate rich (Fig. 4.9) (Gillespie et al., 1986, Scheidt, 2009). The same steps were repeated for all dusty MODIS scenes. After careful examination of both the clear MODIS decorrelated data and the back trajectory models, two potential hotspots were chosen near the Iraqi - Syrian border ( $35^{\circ} 52' N, 39^{\circ} 11' E$  and  $36^{\circ} 24' N, 39^{\circ} 11' E$ ), and higher resolution ASTER data were acquired for those two hotspots. Eleven ASTER scenes were mosaicked to create a single scene for the first hotspot (Fig. 4.11), and twelve other ASTER scenes were mosaicked for the second hot spot (Fig. 4.12). A band scale factor of 0.001 was applied to the mosaicked scenes by performing a band math function to convert the ASTER TIR digital numbers to emissivity values. This was followed by a decorrelation stretch (Fig. 4.13) to highlight surface lithology. Similarly, ASTER DEM scenes for the same hotspots were mosaicked, and a contour line overlay was applied to highlight changes in elevation (Fig. 4.14). These methods were repeated and applied to the dusty ASTER scenes, with the exception of mosaicking, as the different ASTER scenes were acquired at different dates and therefore contained different information.

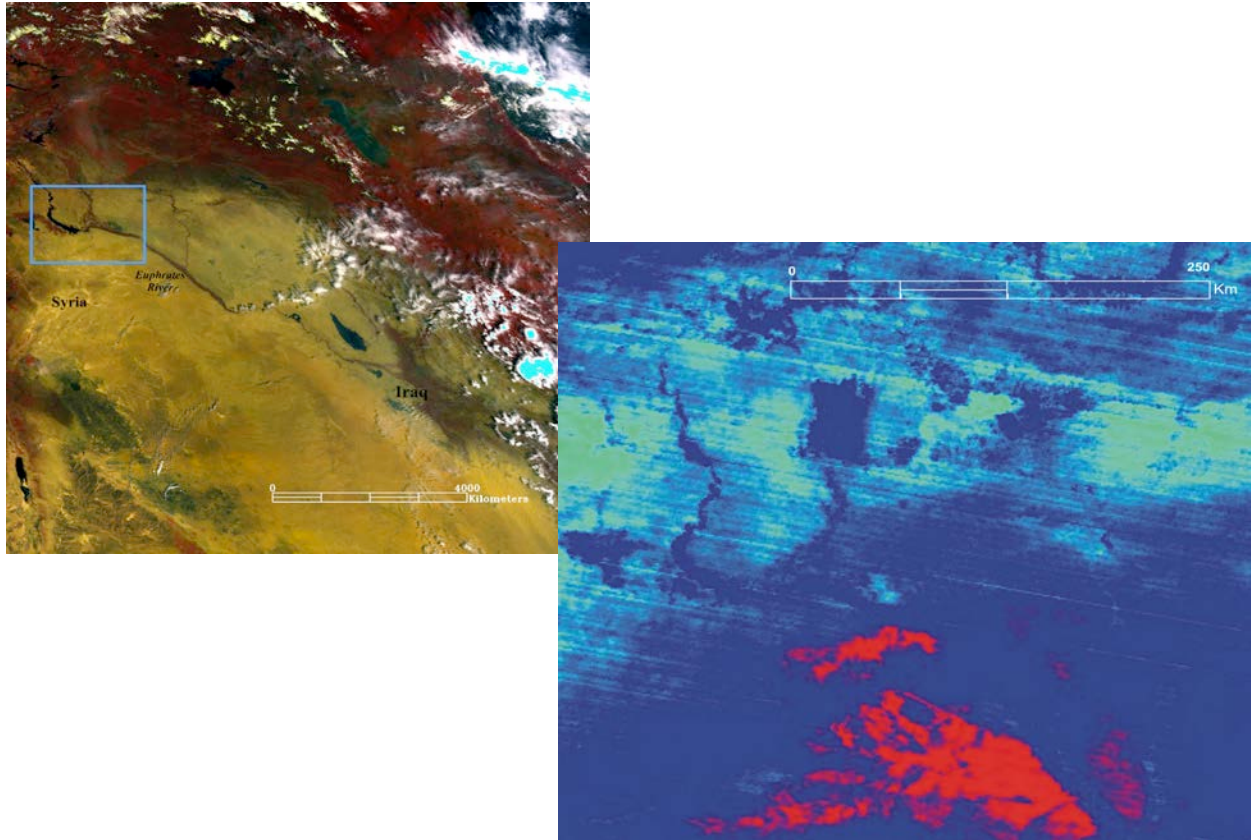


**Figure 4.9 Top: General area of study, blue box highlights the region where the hotspots were located. Bottom: Decorrelation stretch of a clear MODIS subset image for both hotspots showing areas of high quartz (red) carbonates (cyan, blue). R = B32, G = B31, G = 29.**

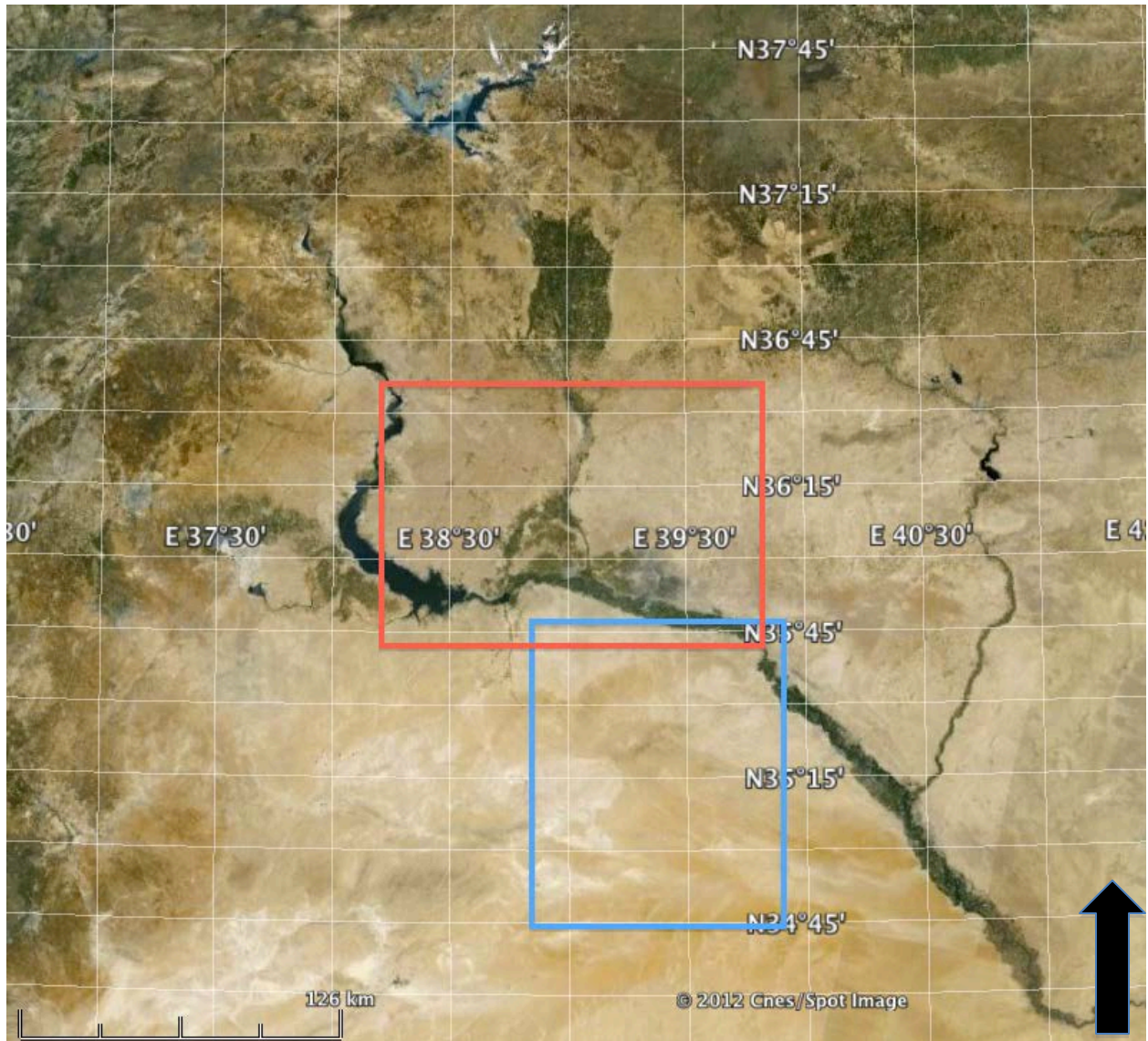
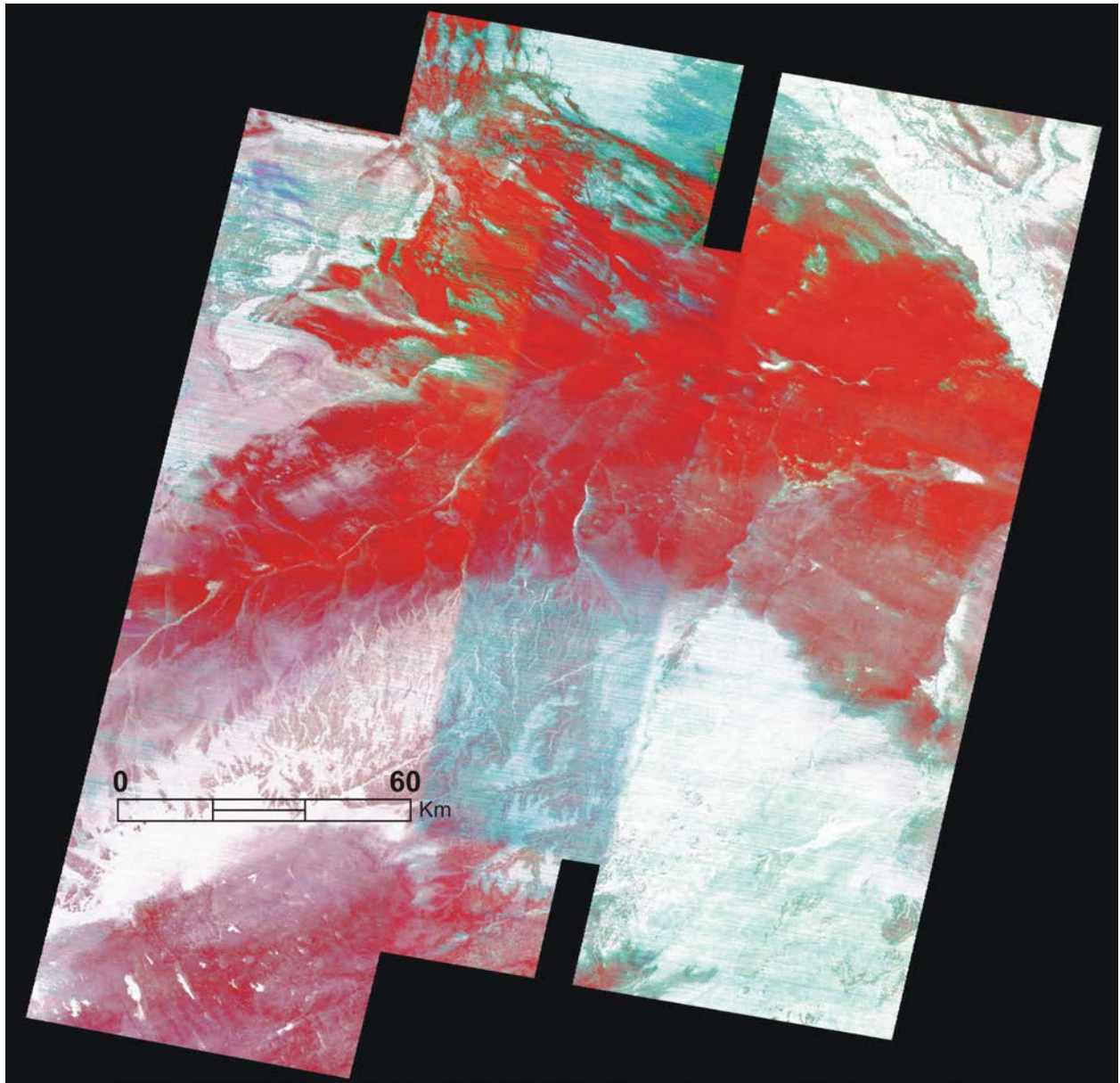
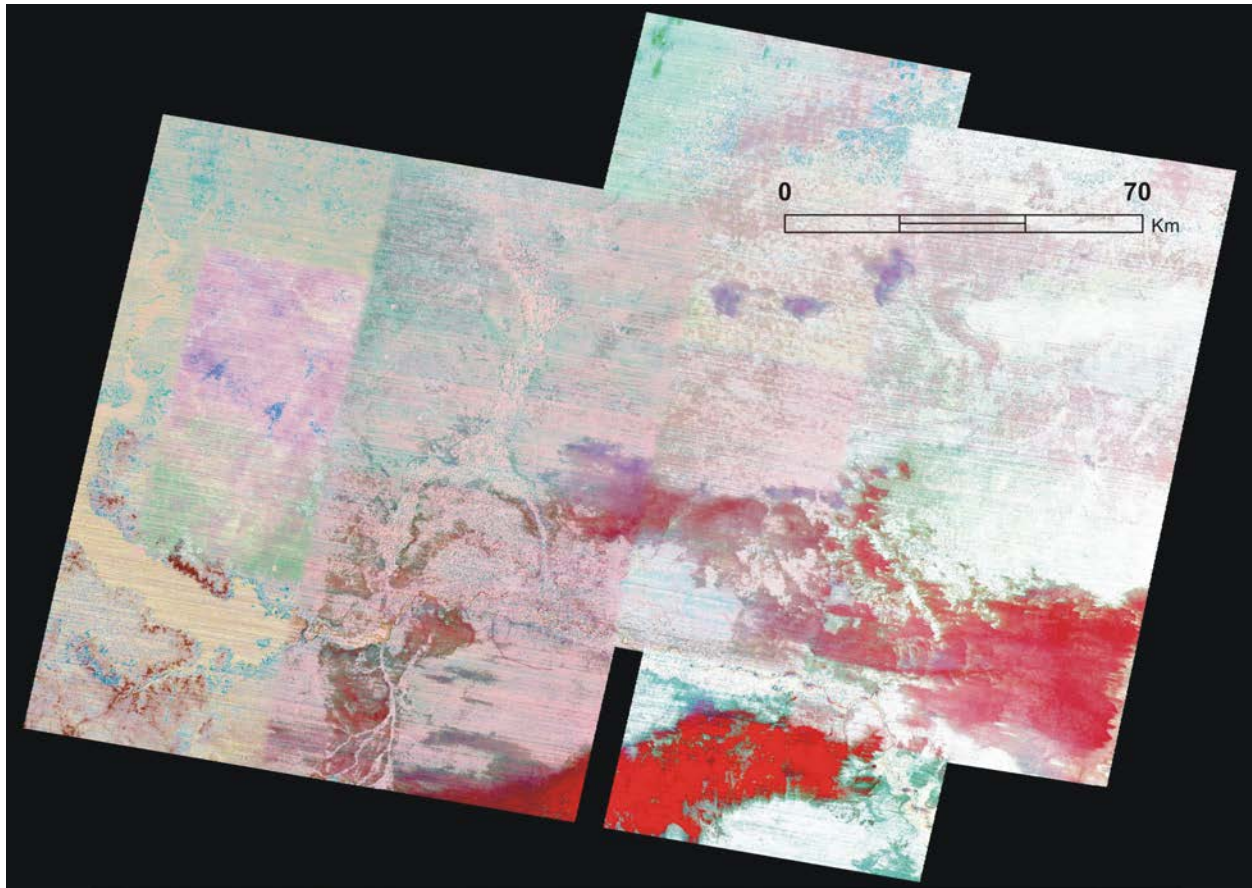


Figure 4.10 General map of study area highlighting the two hotspots. The first hotspot is highlighted by a blue box, the second hotspot is highlighted by a red box (modified from GoogleEarth).





**Figure 4.11 11 ASTER scenes were mosaicked to create a single dataset of the first hotspot (R=B14, G=B12, B=B10).**



**Figure 4.12** 12 ASTER scenes were mosaicked to create a single dataset of the second hotspot (R=B14, G=B12, B=B10).

As outlined in section 3.1, assuming linear mixing of thermal radiant energy is valid, and therefore, mixed spectra retain the spectral features of each particle in proportion to its areal extent (Ramsey and Christensen., 1998, Ramsey et al., 1999). Consequently, linear deconvolution can be used to retrieve composition and concentration from TIR data, including satellite images, using a library of known end members. Based on the XRD and CCSEM findings in section 3.5.1, a combination of end member libraries were used to unmix both clear and dusty ASTER and MODIS images using the image deconvolution option. ASTER bands 10, 11, 12, 13, and 14 were used, as these are the TIR bands and they correspond to the atmospheric

window described earlier. Initially, only MODIS bands 29, 31, and 32 were used, as these have similar wavelength regions to the TIR ASTER bands. Band 30 was excluded due to its opacity caused by ozone absorption. In later stages of analysis, it was decided to include MODIS bands 33 through 36 to increase data resolution and sensitivity. These bands are typically excluded due to their sensitivity to atmospheric moisture. However, the study region is very arid and humidity averages 7%, particularly during summer months, and therefore noise caused by atmospheric moisture would be minimal. The success of image deconvolution was measured by how well the model predicted the end members and the particle size fraction of unmixed spectra, and by the root mean square (RMS) error that is calculated for each unmixing process. RMS values equal to or less than 0.05 indicate a good fit for ASTER, whereas a higher value of 0.1 is used to evaluate MODIS results, as MODIS has a much lower resolution in comparison to ASTER (Liu et al., 2005).

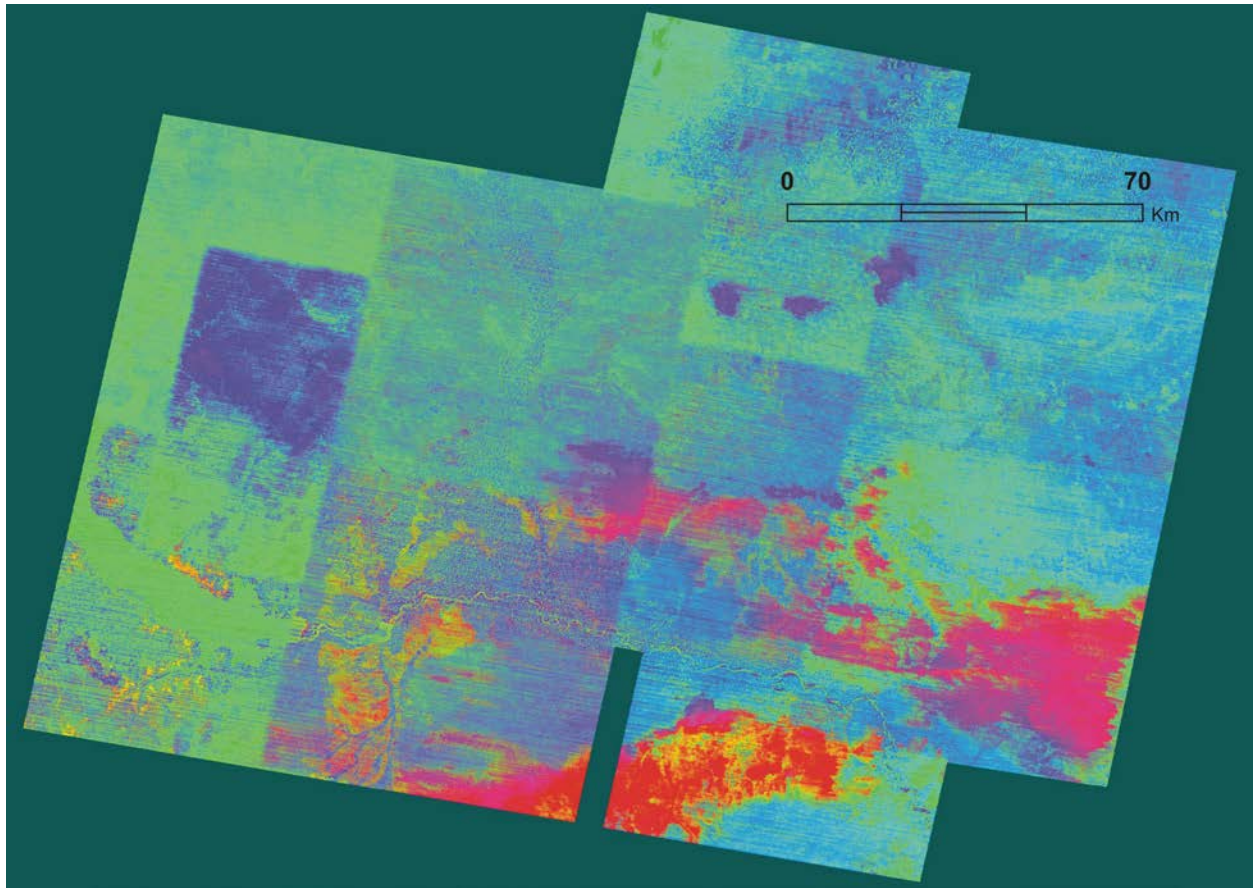


**Figure 4.13** Decorrelation stretch of clear ASTER data highlights differences in surface lithology (Bands 14, 12, 10).

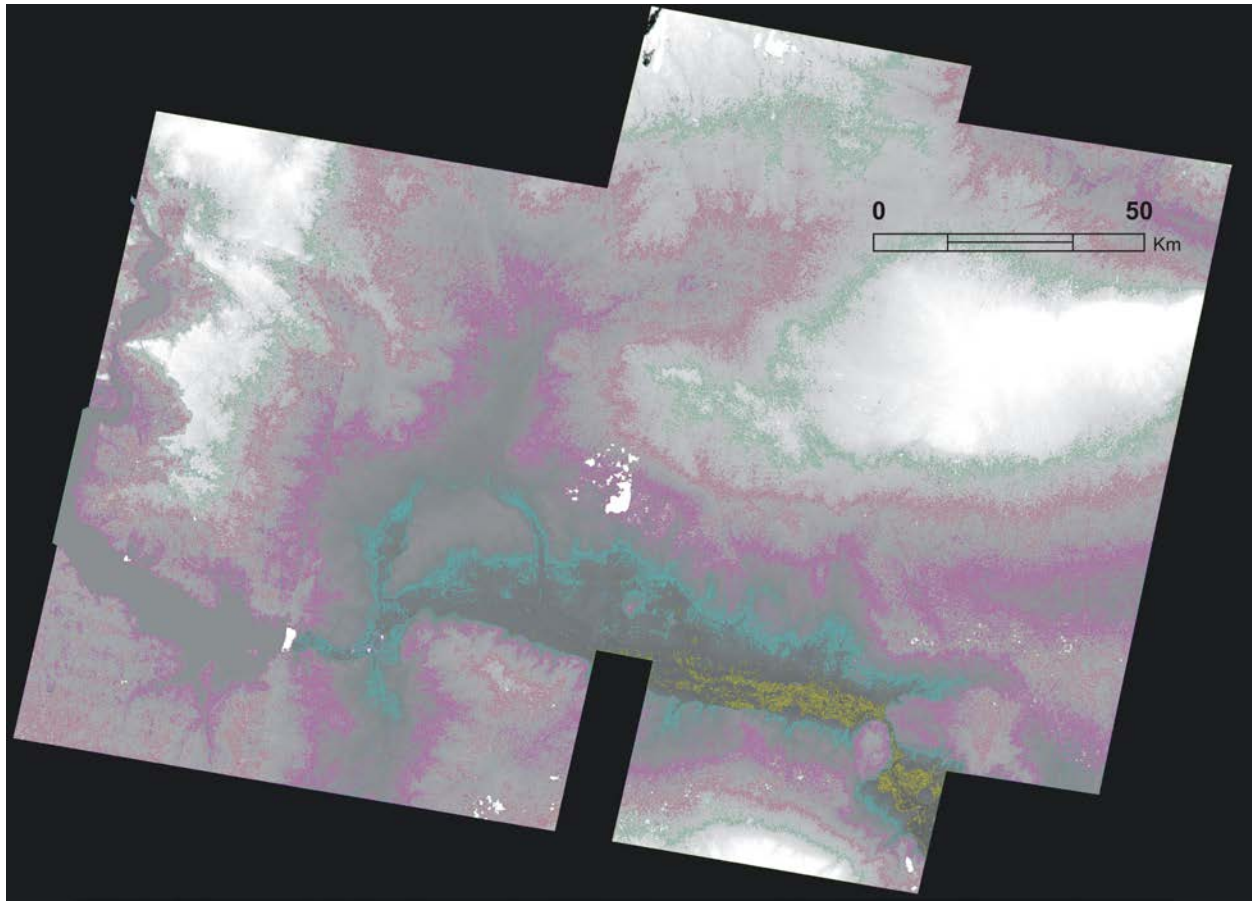


**Figure 4.14** ASTER (ASTGTM) level 2 DEM data for the second hotspot. Counter lines were overlaid on the image to highlight changes in elevation to identify topographic flats that could emit dust.

## **4.4 RESULTS**

### **4.4.1 Clear Scenes**

The image deconvolution results varied between dusty and clear datasets, and between ASTER and MODIS data. Prior to performing the unmixing, it was hypothesized that clear scenes would contain higher amounts of larger ( $>10\ \mu\text{m}$ ) particles, whereas dusty scenes would contain higher amounts of finer ( $<10\ \mu\text{m}$ ) particles. The results were partially supportive of this hypothesis.

Clear ASTER scenes had a mix of very fine and larger particles, whereas clear MODIS scenes were dominated by larger particles. Additionally, clear MODIS scenes were interpreted as having higher percentages of coarse ( $>45\ \mu\text{m}$ ) calcite, whereas clear ASTER scenes identified the finer ( $<10\ \mu\text{m}$ ) calcite size fraction. Both ASTER and MODIS results identified quartz and calcite as the main mineral end members (Figures 4.15, 4.16), with smaller amounts of kaolinite and muscovite. Image deconvolution results for clear ASTER and MODIS scenes are outlined in Table 4.2.

Mosaicking ASTER scenes that were acquired at different times or dates can result in information loss due to averaging of each pixel. To prevent any errors that might arise from mosaicking, one ASTER scene was chosen from the second hotspot mosaic for individual analysis. This scene was selected mainly due to the presence of all different color classes identified by decorrelation stretching. Different spectral library combinations were used, with emphasis on calcite and quartz due to their prominent presence in the dust samples in question. Overall, RMS values were below the 0.05 threshold, and end members identified were much closer to the composition of the dust samples (Table 4.3).

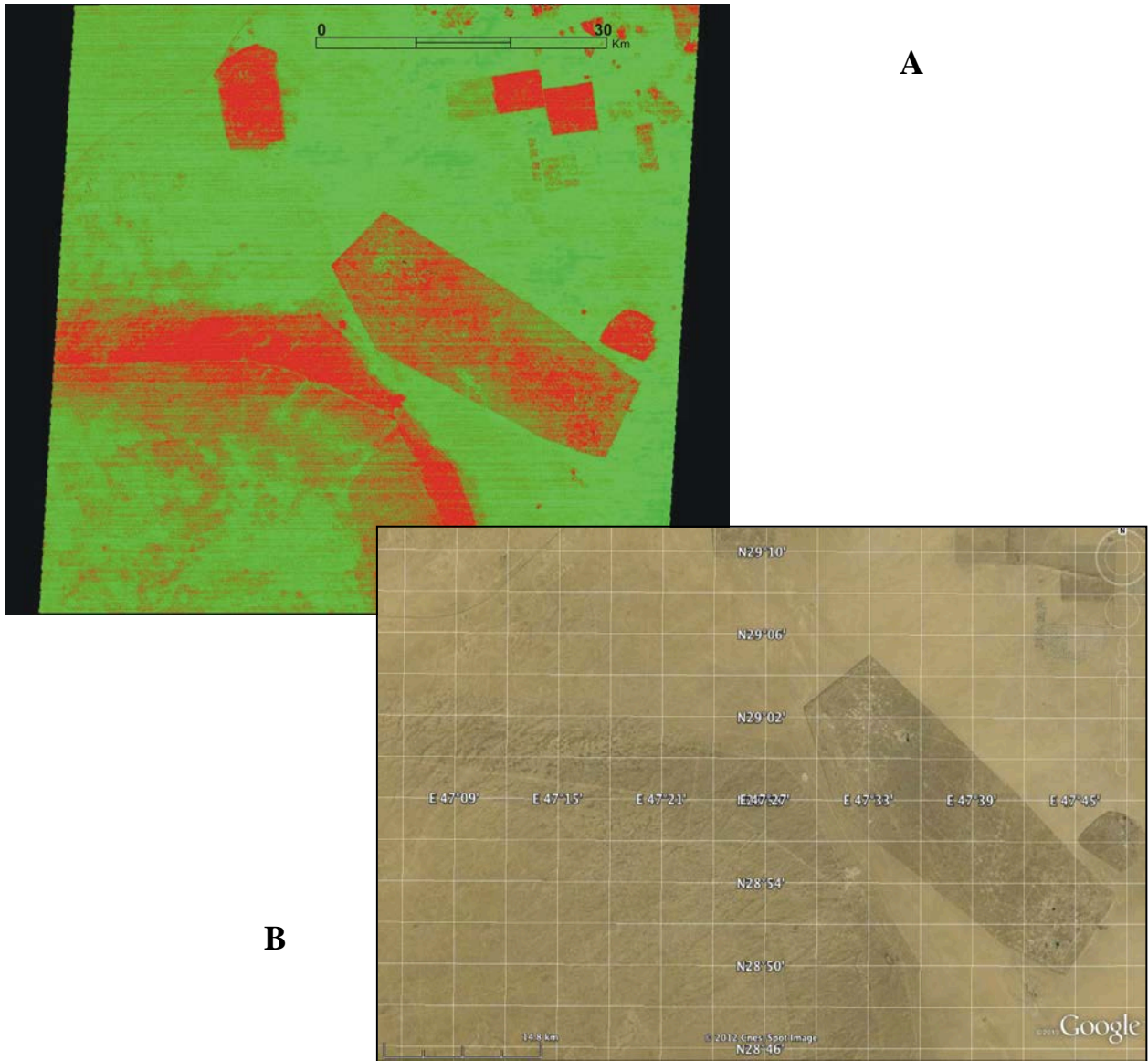
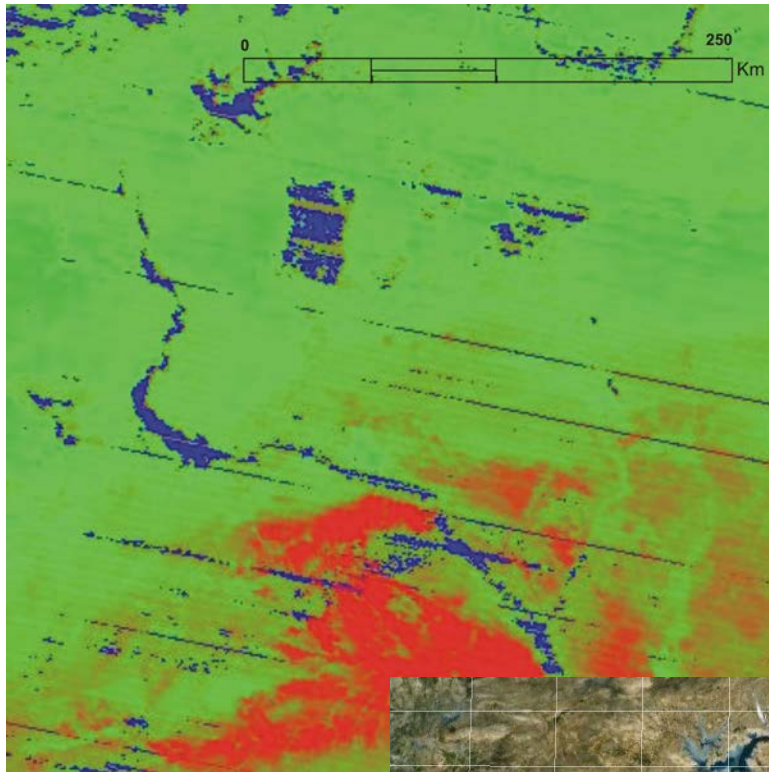
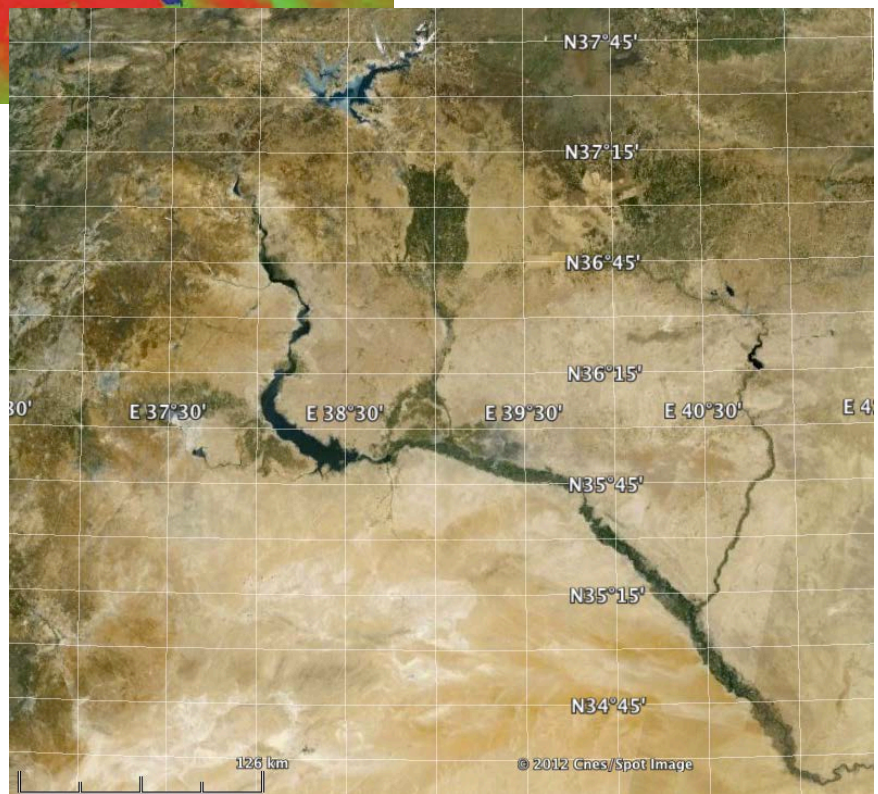


**Figure 4.15 A.** Unmixing of a clear ASTER image along the Kuwaiti-Saudi border. Areas in red have higher quartz content, whereas green areas have higher calcite content. **B.** Visible image of the same area (modified from GoogleEarth).



A



B

Figure 4.16 A. Unmixing of a clear MODIS scene that contains both hotspots (separated by the Euphrates River in blue). Areas in red have high quartz content, whereas areas in green have high calcite content. B. Visible image of the same area (modified from GoogleEarth).



**Table 4.2 Image deconvolution results for clear ASTER and MODIS data.**

Scene (times in UTM)	Library	Percentage Identified	Averaged Image RMS
ASTER			
Mosaic	Quartz 20-40	32.16%	0.013
	Calcite <10	3.5%	
	Kaolinite	0%	
	Muscovite >45	31.45%	
	Blackbody	32.70%	
Mosaic	Kaolinite	0%	0.009
	Quartz <10	3.86%	
	Quartz 20-40	63.24%	
	Calcite <10	0.007%	
	Blackbody	32.86%	
Mosaic	Kaolinite	0%	0.05
	Quartz <10	100%	
	Calcite <10	0%	
	Muscovite <10	0%	
Mosaic	May Spectra	0%	0.119
	Blackbody	100%	
706 Sept 9, 2005 (07:32)	Quartz <10	0.0029%	0.05
	Quartz 10-20	51.264%	
	Calcite <10	34.69%	
	Blackbody	14.04%	
MODIS			
040 subset Aug 28, 2011 (08:00)	Quartz 20-40	59%	0.218
	Calcite 20-45	0%	
	Calcite >45	38.64%	
	Dolomite >45	0%	
	Muscovite 20-45	2.28%	
040 subset	Quartz 20-40	5.08%	0.210
	Calcite >45	2.78%	
	Muscovite 20-45	0%	
	Kaolinite	2.12%	
	Forsterite >45	0%	
	Blackbody	95.1%	

040 subset	Quartz <10	0%	0.233
	Quartz 10-20	0%	
	Calcite <10	0%	
	Andesine <10	0%	
	Kaolinite	0%	
	Blackbody	100%	

**Table 4.3 Image deconvolution results for one clear ASTER scene.**

Scene	Library	Percentage Identified	Averaged Image RMS
AST_05_00308012008081511	Quartz <10	0%	0.019
	Quartz 10-20	61.93%	
	Calcite <10	21.14%	
	Muscovite 10-20	2.97%	
	Blackbody	13.96%	
AST_05_00308012008081511	Quartz <10	0%	0.020
	Quartz 10-20	55.88%	
	Calcite <10	18.95%	
	Kaolinite	11.21%	
	Blackbody	13.96%	
AST_05_00308012008081511	Quartz 10-20	59.79%	0.019
	Calcite <10	4.42%	
	Dolomite 10-20	15.6%	
	Fayalite mix 2.7-10	6.23%	
	Blackbody	13.96%	

#### 4.4.2 Dusty Scenes

The particle size hypothesis was partially true where dusty data was unmixed. Dusty ASTER scenes were interpreted as having very fine (< 10  $\mu\text{m}$ ) particles. However, MODIS results contained a mix of very fine and coarser particles, both suspended (dusty scenes) and on the ground (clear scenes). This discrepancy between dataset results was more evident in mineral end

member identification. ASTER data were dominated by calcite (Fig. 4.17), andesine, and kaolinite (Fig. 4.18), with very minor (< 1%) amounts of quartz (Fig. 4.19). Figure 4.20 shows RMS results for ASTER, where brighter pixels have higher RMS values and darker pixels have lower RMS values. MODIS data were more sensitive to quartz and overestimated the amount of quartz in the dust plumes in comparison to lab-analyzed dust samples. Adding the spectra of the May and July storms to the spectral library of their corresponding MODIS data had varying results. The July spectrum was identified as an end member when unmixed with dust plumes from that storm. However, May spectrum was not identified when unmixed with MODIS data from that storm (Fig. 4.21). Figure 4.22 shows RMS results for MODIS. No data showing dust plumes from the March storm was available, thus unmixing with that spectrum was not performed. Dusty image deconvolution results for dusty ASTER and MODIS scenes are outlined in Table 4.4.

**Table 4.4 Image deconvolution results for dusty ASTER and MODIS data.**

Scene (times in UTM)	Library	Percentage Identified	Averaged Image RMS
ASTER			
706 may 4, 2005 (07:33)	Quartz <10	0.334%	0.035
	Calcite <10	31.72%	
	Andesine <10	43.44%	
706	Quartz <10	0.89%	0.043
	Calcite <10	46.92%	
	Kaolinite	32.63%	
706	May	0%	0.82
	July	47.06%	
	March	1.14%	
MODIS			
5529 subset	July	14.90%	0.215

July 14, 2010 (08:20)	Quartz <10	0%	
	Quartz 10-20	85.09%	
	Calcite <10	0%	
	Kaolinite	0%	
5529 subset	Calcite <10	0%	0.216
	Calcite 20-45	0%	
	Quartz <10	0%	
	Quartz 10-20	100%	
	Kaolinite	0%	
020 subset	Calcite <10	0%	0.202
May 11, 2010 (13:21)	Calcite 20-45	59.18%	
	Quartz <10	40.23%	
	Quartz 10-20	0%	
020 subset	Quartz <10	100%	0.229
	Calcite <10	0%	
	Calcite 20-45	0%	
	Dolomite <2.7	0%	
	Muscovite <10	0%	
020 subset	May	0%	0.228
	Quartz <10	0%	
	Quartz 10-20	100%	
	Calcite <10	0%	
	Calcite 20-45	0%	
	Kaolinite	0%	

---

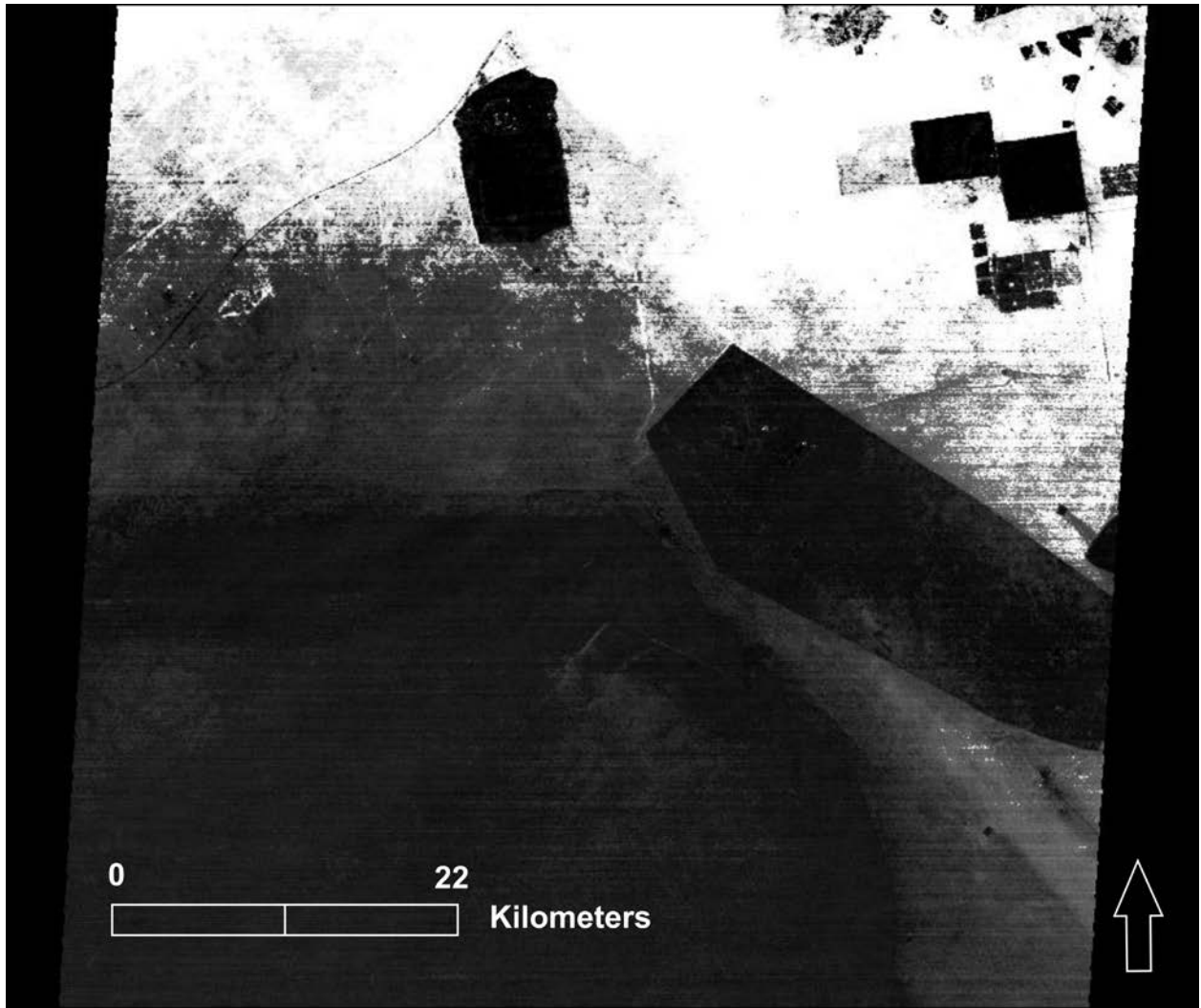


**Figure 4.17 Unmixing of a dusty ASTER near the Kuwaiti-Saudi border showing calcite content. Brighter pixels have the highest calcite content whereas darker pixels have the lowest. Based on  $\Delta T$  investigations, the southern half of the image was determined to be dusty, whereas the northern half was relatively clear.**

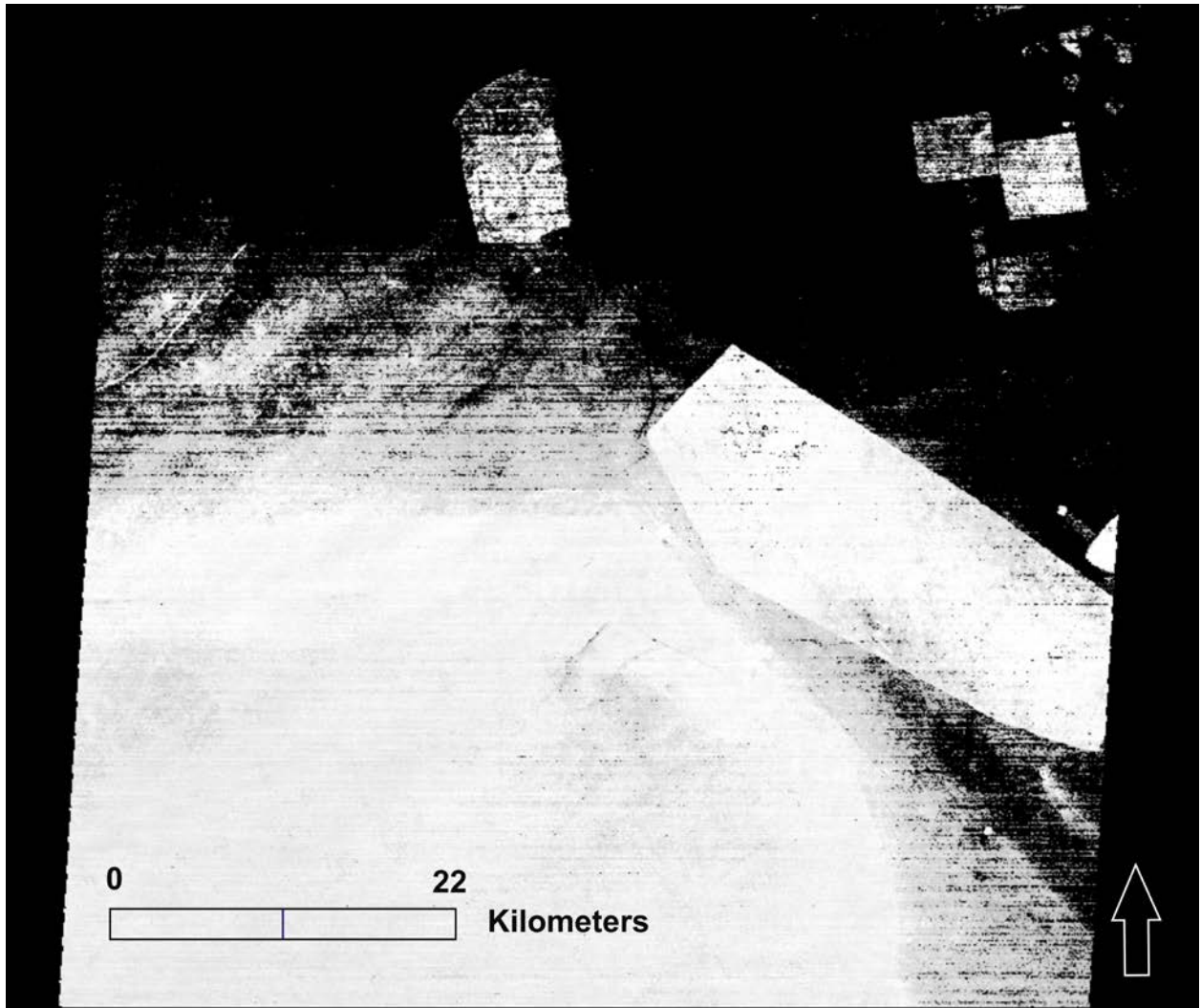
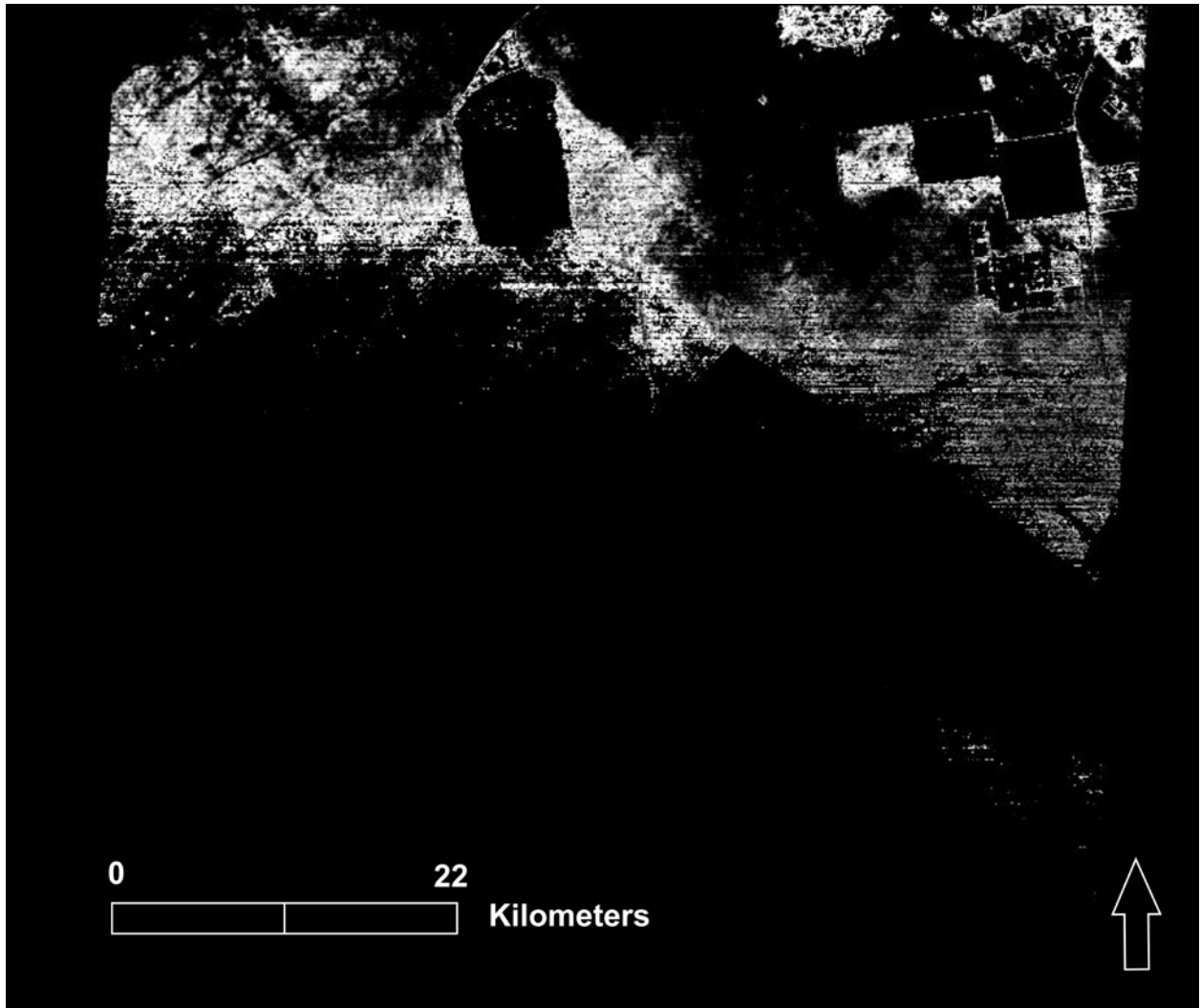
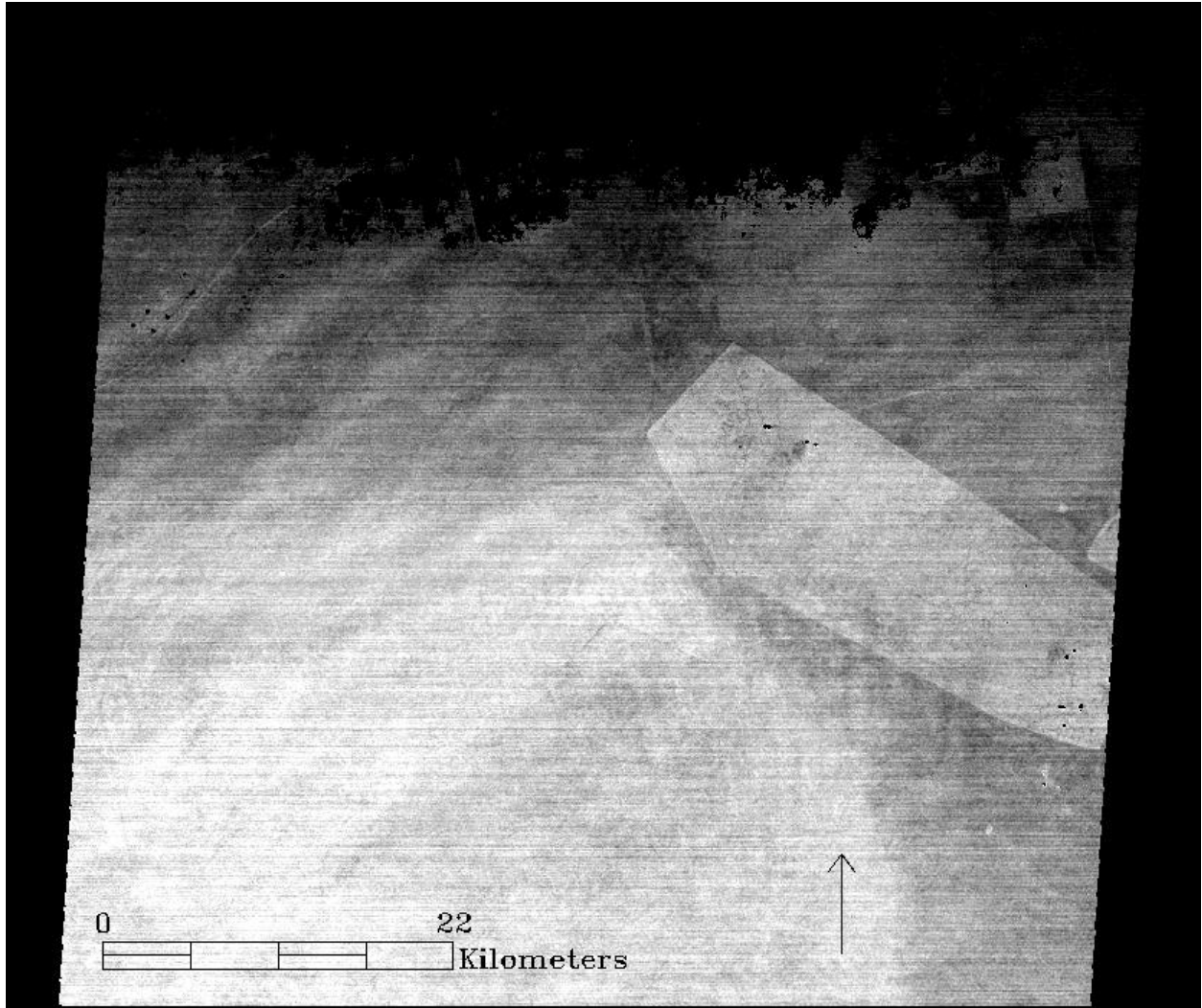


Figure 4.18 Kaolinite unmixing results for the same dusty ASTER scene, showing higher kaolinite content in the dusty areas (south).



**Figure 4.19** Unmixing results for the same dusty ASTER scene showed no quartz in the dusty areas, whereas some surficial quartz was identified in the clear upper half of the scene.



**Figure 4.20** ASTER image deconvolution RMS results. Brighter pixels indicate high RMS values, darker pixels indicate low RMS values.



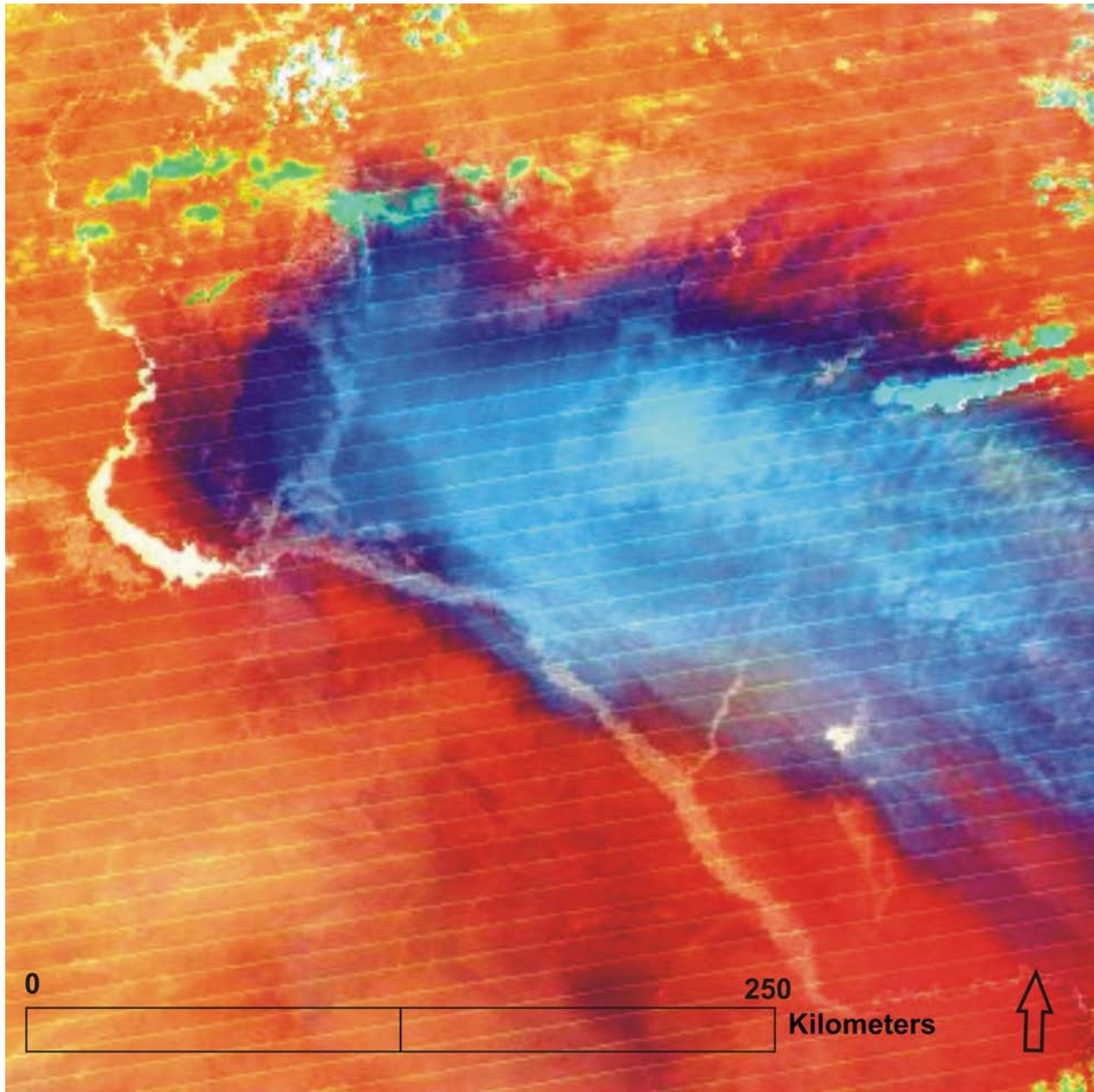


**Figure 4.21 Unmixing of dusty MODIS scene from the May storm did not identify the May spectra as an end member. Instead, it identified calcite 20-45  $\mu\text{m}$  (blue) and quartz  $<10 \mu\text{m}$  (red). Green = cloud tops.**

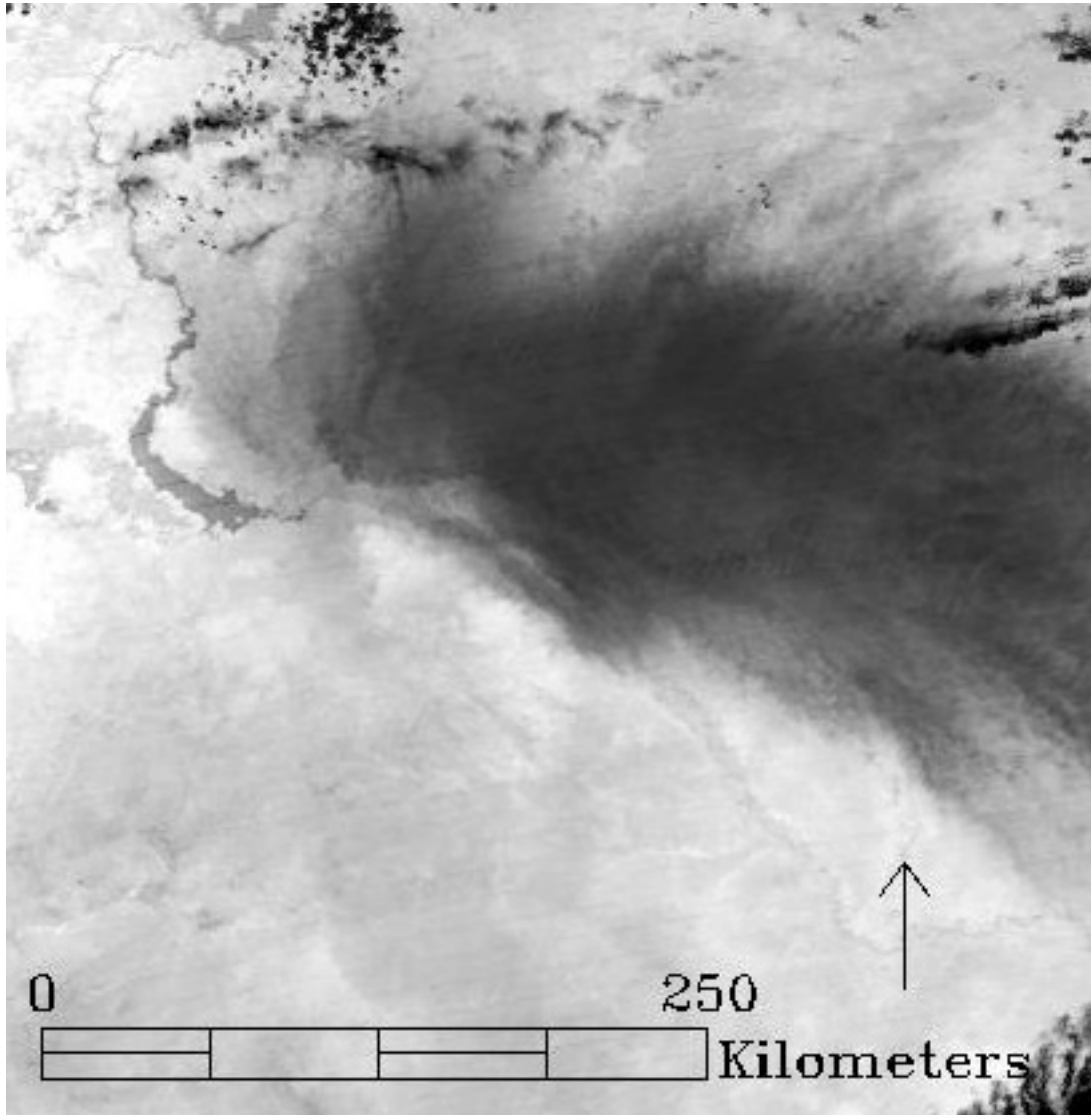


Figure 4.22 MODIS spectral deconvolution RMS results. Brighter pixels indicate high RMS values, darker pixels indicate low RMS values.

## 4.5 DISCUSSION

Unmixing of clear MODIS images produced results that were more comparable to the grain size hypothesis outlined in section 4.4.1. However, the presence of finer calcite particles in the ASTER unmixing results should not invalidate these findings. ASTER TIR data has higher spatial resolution compared to MODIS (90 m compared to 1 km). The increase in spatial resolution may result in an increase in spectral sensitivity and consequently, better analysis of surface deposits. The presence of finer calcite could be interpreted as areas of salt flats or dust hotspots that supply finer calcite to dust storms in that region. This is in agreement with previous findings that showed higher ratios of calcite to quartz in dust storms affecting Kuwait and neighboring areas (Engelbrecht et al., 2009).

The findings of dusty data unmixing were more varied. ASTER proved more sensitive to finer particles, whereas MODIS was less so. However, the presence of larger calcite particles in MODIS results may not be incorrect, as it is possible that larger calcite particles were present in the dust plume before settling in situ. End members identified in ASTER were missing quartz, a key component and the second abundant mineral identified by XRD analysis. Further, andesine and kaolinite were overestimated, and at times were assigned higher percentages than calcite. MODIS findings were more in agreement with XRD findings and identified both calcite and quartz as the main end members present in the dust plumes.

Quartz, andesine, and kaolinite have absorption features that overlap, especially in the 9 to 10  $\mu\text{m}$  region (Fig. 4.23). ASTER bands 12 (8.925 – 9.275  $\mu\text{m}$ ) and 13 (10.25 – 10.95  $\mu\text{m}$ ) are sensitive to all three minerals, and therefore, it is possible that the presence of kaolinite may suppress the spectral features of quartz, resulting in misdiagnosing quartz as andesine (Fig 4.24).

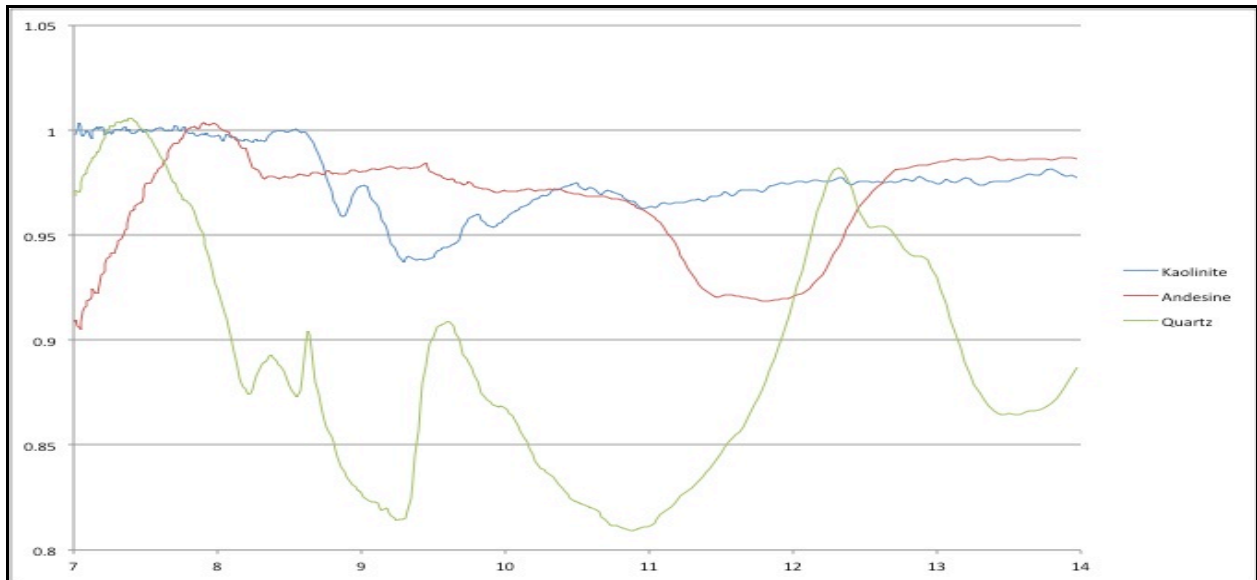


**Figure 4.23 Quartz, andesine, and kaolinite have absorption features that overlap.**

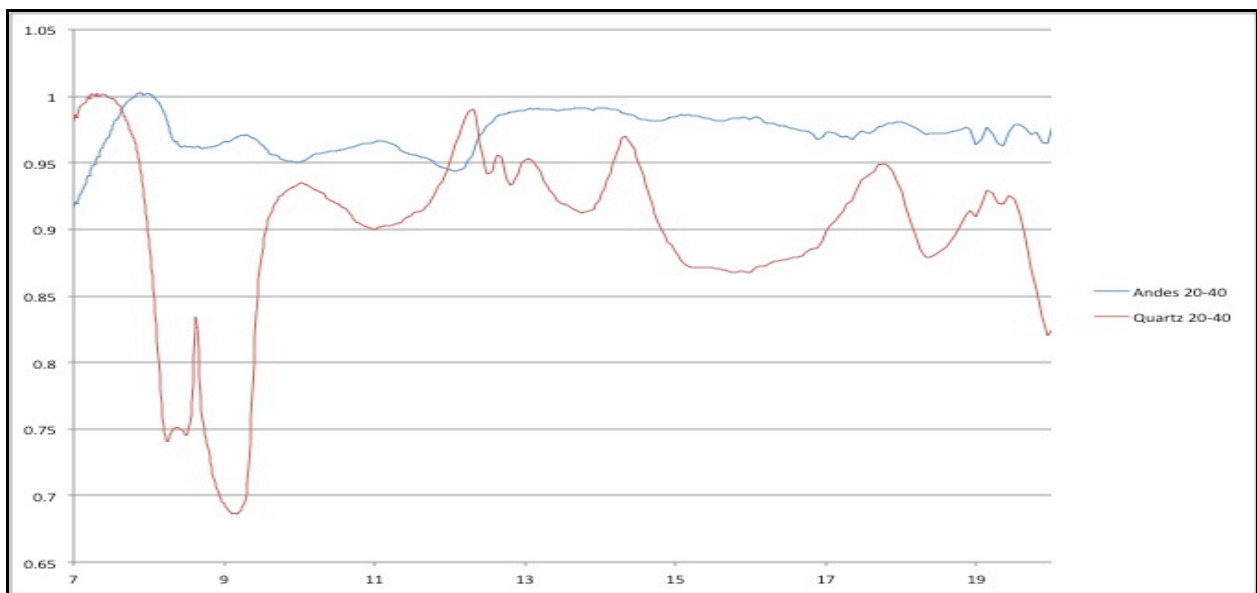


**Figure 4.24 The presence of Kaolinite can result in suppressing the spectral features of quartz, and consequently misdiagnose quartz with andesine.**

MODIS may be less prone to this issue due to the exclusion of band 30 (9.58 – 9.88  $\mu\text{m}$ ) due to ozone interference. Alternatively, falling dust may cover surfaces and create a masking effect, thereby concealing the underlying spectral features of other minerals.

RMS values and compositional analyses were in general agreement for ASTER data, both dust and clear. The only exception is the third clear ASTER scene unmixing with kaolinite, calcite, quartz, and muscovite, where both quartz and calcite yielded 100% and RMS = 0.05 (Table 4.2). This may have been the result of limiting particle size to  $< 10 \mu\text{m}$  and excluding larger particles, resulting in a misfit. All MODIS results have RMS values larger than the 0.10 threshold. The lowest RMS value = 0.202, and corresponded to the best compositional fit and the closest to the XRD results and exceeding all ASTER unmixing results. Scientific literature assessing the quality of MODIS unmixing examine all 36 bands, including the non-thermal bands (Liu et al., 2005), as unmixing is not exclusive to minerals and is commonly applied to forests and different types of grass. Therefore, the 0.10 threshold value may not truly represent unmixing of minerals in the TIR region, and a higher threshold value closer to 0.20 is possibly more representative of such analyses.

Although no significant change was observed in RMS values, unmixing of single ASTER scenes produced more accurate end member identification (Table 4.3). Mosaicking can lead to loss of information, especially when attempting to mosaic scenes that were acquired at different times. Consequently, unmixing of mosaics tends to produce results that are the average of all scenes, resulting in less than accurate interpretation.

## **4.6 CONCLUSION**

Possible dust emitting areas or hotspots were identified using a combination of forward and backward trajectory models, and thermal infrared ASTER and MODIS data. Backward trajectory models were used to identify air parcels affecting Kuwait during three different dust

storms. The results of the backward trajectories were further confirmed by running forward trajectory models from the areas that were identified as source areas in the backward trajectories. This was followed by applying decorrelation stretches to both TIR ASTER and MODIS data to highlight difference in surface lithology. Finally, image deconvolution techniques were applied to the satellite data to identify both surface and dust plume mineral compositions and particle sizes.

Image deconvolution and unmixing of satellite data produces variable results based on the type of data used in the analysis, as spatial resolution is key. ASTER data is more sensitive to smaller particles and produces higher resolution unmixing results of surficial deposits. However, underestimation of quartz is possible in the presence of other minerals with similar spectral features. This can produce inaccurate compositional estimates. MODIS data is less sensitive to finer (<10  $\mu\text{m}$ ) grains due to its lower spatial resolution. This becomes a problem when attempting to unmix dust plumes consisting of very fine particles. Nonetheless, utilizing the correct end members can overcome this problem and produce accurate compositional analysis.

Interpretation of ASTER mosaics may be misleading, as the process of mosaicking causes some loss of information in an attempt to create a seamless mosaic. Therefore, it is critical that analysis be performed on individual scenes, especially if scenes were acquired at different times.

Finally, a higher threshold RMS value to assess MODIS unmixing results may be required when working with the TIR region. The current accepted RMS value of 0.10 was derived from coarser particles and other non-geologic surfaces, and does not account for spectral

behavior associated with finer ( $<60 \mu\text{m}$ ) particles. Therefore, it is crucial to revise this value for MODIS to account for finer particles.

## 5.0 SUMMARY

Many regions are prone to the effects of dust storms, particularly arid and semi-arid regions. In particular, dust storms have become more frequent in Kuwait in the last decade (Al-Awadhi, 2005), and becoming a hazard to humans, environment, economy, and health. Therefore, it is important to understand the nature of these storms and the mechanisms resulting in their formation. Further, identifying areas that are potential sources for dust storms is key in hazard mitigation and prevention. Remote sensing techniques in general, and thermal infrared tools specifically, are great tools for monitoring dust storms and their sources, as they provide large spatial coverage and provide access to areas that are inaccessible to field research.

This dissertation is an attempt to bridge the gap between thermal infrared (TIR) techniques and eolian studies pertaining to very fine particles in general, and dust storms in particular. The absence of a reliable fine grained ( $< 60 \mu\text{m}$ ) spectral library presented a challenge that was overcome by creating a new library dedicated to seven minerals in the 2.7 to 45  $\mu\text{m}$  range. This library is an important asset for future studies in that particle size range, and will hopefully provide a tool to better understand spectral changes in intensity and morphology related to decreasing particle size. Similarly, spectral and image deconvolution techniques were examined with respect to identification of dust storm mineral content and particle size, as previous studies have determined that particles  $< 10 \mu\text{m}$  were difficult to accurately model (Salisbury et al., 1991, Ramsey and Christensen, 1998). Finally, a possible link was established



between dust storms affecting Kuwait and possible dust sources in eastern Syria and western Iraq. This was possible through the use of several back and forward Hybrid Single Particle Lagrangian Integrated Trajectory (HYSPLIT) models, in addition to results from decorrelation stretching and deconvolution of satellite data. These results were also validated using the Food and Agriculture Organization's (FAO) world soil map, confirming that these hotspots have calcite and gypsum rich soils, and that was reflected in both dust samples collected in the field and TIR analyses.

Dust samples collected from Kuwait for three different dust storms (May, July 2010, March 2011) were analyzed using CCSEM and XRD to obtain particle size distribution and mineral content. The results of both analyses were used to create very fine (2.7 – 45  $\mu\text{m}$ ) spectral libraries containing pure mineral end members, in addition to other end members that were used as proxies. The purpose of creating these libraries was to overcome the limitations associated with available spectral libraries imposed by the very fine size of dust particles. This was followed by a spectroscopic analysis, and its results were validated using the known XRD results. Finally, spectra obtained from all three dust storms, in addition to the newly created spectral library, were used to unmix clear and dusty ASTER and MODIS TIR satellite data, to survey how accurate TIR satellite data can be in identifying mineral content and associated particle sizes in dust plumes.

Analyzing dust spectra showed that particle size plays a major role in spectral analysis, particularly in the < 60  $\mu\text{m}$  fraction. Appropriate size fraction end members should be used for spectral deconvolution, and attention must be paid to their spectral range and resolution, as both can affect residual errors and introduce uncertainties. Lower RMS values are not an indicator of a correct compositional fit, as spectral features of certain minerals may be greatly affected by the

presence of other minerals, resulting in either over or under estimation. A basic knowledge of the possible constituents of an unknown mixture is valuable and can help produce better predictions by increasing the number of end members in spectral deconvolution. Further, the spectral deconvolution model succeeded in identifying mineral end members present in mixed spectra. However, the model failed with respect to identifying correct particle size ranges present in the mixed spectra. This was evident when attempts were made to unmixing three lab-created mixtures of calcite, quartz and forsterite, where the relative abundance of each mineral in the mixtures were either over or under estimated.

Image deconvolution and unmixing of satellite data produces variable results based on the type of data used in the analysis, as spatial resolution is key. ASTER data were more sensitive to smaller particles and produced higher resolution unmixing results of surficial deposits. However, underestimation of quartz is possible in the presence of other minerals with similar spectral features. This can produce inaccurate compositional estimates. MODIS data is less sensitive to finer (<10  $\mu\text{m}$ ) grains due to its lower spatial resolution. This becomes a problem when attempting to unmix dust plumes consisting of very fine particles. Nonetheless, utilizing the correct end members can overcome this problem and produce accurate compositional analysis. Finally, a higher threshold RMS value to assess MODIS unmixing results may be required when dealing with the TIR region, as the current RMS standard of 0.10 is too low.

The findings of this dissertation are important for dust hazard mitigation and prevention. Using a fine-grained spectral library for analyzing future dust storms can enhance understanding of their composition, and consequently, their possible source areas. Identifying dust source areas can be useful for dust warning systems that are based on meteorological data, where these areas

are constantly monitored for changes in air pressure or wind speed and direction. Further, careful examination of changes in land use in these areas could shed some light on any human-induced factors that may lead to erosion, and consequently, the intensification of dust storms.

## **APPENDIX A**

### **MINERAL POWDER PREPERATION AND CREATION PROCEDURES**

This appendix lists the steps and procedures involved in creating the mineral dust. Work was performed by Dr. Amy Wolfe at the EPA facilities in Oklahoma, as outlined by Wolfe et al. (2007).

## Sample Prep

### Powder Preparation

Forsterite, Fayalite, Dolomite

- Forsterite, fayalite and dolomite samples were crushed into pea – sized pieces using a sledgehammer. The sledgehammer, quartz plate, and samples were wrapped in aluminum foil to prevent contamination.
  - o Note: photos of the samples were taken before they were crushed them with a sledgehammer.
- Samples were milled into a powder using a Retch ISO-9001 mixer mill (Brinkmann Inc) equipped with stainless steel cups (25 mL in size) and stainless steel grinding balls (20 mm diameter).
  - o Forsterite, fayalite and dolomite samples were milled for 5, 2, and 3 minutes, respectively, at 100%.
  - o The powdered samples were transferred to, and stored in, acid-rinsed (~50% HNO<sub>3</sub> solution) 120 mL HDPE bottles.
- Calcite

- This sample was received in powder form (<63 mm).

Muscovite

- The muscovite sample was transferred to a ~350 mL plastic container and ground into a powder using a “knife mill” (Sunbeam Products, Inc) with a single stainless steel s – blade. The plastic container, and blade, were acid washed in a ~50% HCl nitric acid solution.
  - a. Note: a Rival 1.5cup food chopper was used to process muscovite. It’s essentially a knife mill.
  - b. Nitric was not used to clean the stainless steel blade because it would have oxidized the blade and contaminated the sample with iron. HCl was used instead.
  - o The sample was pulsed repeatedly for 10 – 15 sec until a visual inspection of the sample revealed the presence of very fine particles.
    - a. The sample was ground for a total of 1 – 1.5 hrs, spread out in 10 minute increments over an 8 hr period.
- The sample was ground twice. The first time was before sieving the sample. The sieved material was taken and re-ground to <10 mm in size.

### Wet Sieving

- The target size fraction for each sample was ~2 mm in size, approximately the size of dust particles.
- The procedure outlined in Wolfe, A.L. et al. (2007) was followed, with minor modifications.
  - o Modifications included:
    - a. The filter paper grade (50 instead of 54).
    - b. Methanol was used to wet.
  - o The paper referenced above is:
    - a. Wolfe, A.L., Liu, R., Stewart, B.W., Capo, R.C., and Dzombak, D.A., 2007, A method for generating uniform size-segregated pyrite particle fractions:

- The set-up:
  - o A vacuum filtration technique was used to obtain multiple size fractions of each mineral.
  - o Three – inch stainless steel sieves, mesh sizes 325 (45 mm), 625 (20 mm), and 1250 (10 mm) were inserted into a one-piece porcelain Büchner funnel with a fixed perforated plate (Fisher Scientific, bottom inner dia.: 72mm). A Whatman Grade 50 filter paper was placed in the Büchner funnel to collect material larger than 2.7 mm (see Fig 1 of paper).
  - o A rubber crucible adapter was used to ensure a tight seal between the funnel and 1L Pyrex side arm flask.
    - a. The flask was attached to a support stand using adjustable angle clamps.
  - o Tygon tubing was used to connect the flask to the vacuum line.
- Procedure:
  - o Approximately 40 – 50 g of the powdered mineral sample was poured onto the top of the sieve stack to begin the wet sieve process.
  - o 50% (v/v) methanol was added to the sample until the entire sample had been sieved.
    - a. Upon completion, the mineral sample was collected from each sieve and oven – dried 30 – 60 minutes at 60°C.
- When dry, the samples were transferred to acid – washed glass vials (they were boiled in a 50% HCl solution).
  - a. The targeted size fraction (2 mm) passed through the filter paper (~2.7 mm) during wet sieving. Therefore, the solution was transferred to a 500 mL beaker, evaporated to dryness, and the solid collected.
- The solid was transferred to an acid-washed glass vial (see above).
  - o Note: The % recovery for each of the samples was calculated and it was better than 95% for all mineral samples.

### **Final Products**

- The following size fractions were collected for each mineral sample:
  - \_ Forsterite, fayalite, dolomite, calcite:
    - >45 mm, 20 – 45 mm, 10 – 20 mm, 2.7 – 10 mm, <2.7 mm
  - \_ Muscovite
    - >45 mm, 10 – 45 mm, <10 mm
- o It was very difficult to acquire the <2.7 mm size fraction for muscovite.

## **APPENDIX B**

### **XRD RESULTS FROM R J LEE GROUP**

A detailed report received from R J Lee Group outlining the XRD findings of the three dust samples collected during dust storms in Kuwait.

### LABORATORY REPORT

University of Pittsburgh  
 4107 O'Hara St SRCC Room 200  
 Pittsburgh, PA 15260-3332  
 ATTENTION: Redha Mohammad  
 Telephone: 412-805-0229

Report Date: November 23, 2011  
 Samples Received: November 8, 2011  
 RJ Lee Group Job No.: CXH1019938-0  
 Client Job No.: RM  
 Purchase Order No.: N/A

#### ANALYSIS: X-ray diffraction (XRD) for crystalline phases

A portion of the sample was ground and mounted into a standard XRD holder for analysis. The sample was run on a PANalytical X'Pert Pro diffractometer using copper radiation. The resulting diffraction pattern was then analyzed using the X'Pert HighScore program utilizing the ICDD database. Quantification is based upon calibration coefficients derived from standards mixed with fluorite.

Client Sample No.: A  
 RJ Lee Group Sample No.: 10174153

Phase	Composition	Concentration
Calcite	Ca(CO <sub>3</sub> )	14-19
Quartz	SiO <sub>2</sub>	8-13
Feldspar	(K,Na,Al)Si <sub>3</sub> O <sub>8</sub>	3-8
Dolomite	CaMg(CO <sub>3</sub> ) <sub>2</sub>	1-5
Mica	KAl <sub>2</sub> (AlSi <sub>3</sub> O <sub>10</sub> )(F,OH) <sub>2</sub>	1-5
Chlorite/Serpentine	(Mg,Al) <sub>6</sub> (Si,Al) <sub>4</sub> O <sub>10</sub> (OH) <sub>8</sub>	<2
Palygorskite	(Mg,Al) <sub>3</sub> (Si,Al) <sub>8</sub> O <sub>20</sub> (OH) <sub>2</sub> · 8H <sub>2</sub> O	Trace*
Unknown**	-	Minor-Trace

\*Phases that we do not possess standards for cannot be quantified. Qualitative results are given in such cases.

Qualitative results are defined as: major: >20%, minor: 5-20% and trace: <5%.

\*\*Additional phases that were not identified may be present. It is also possible that there is an amorphous phase present that cannot be identified or quantified by XRD.



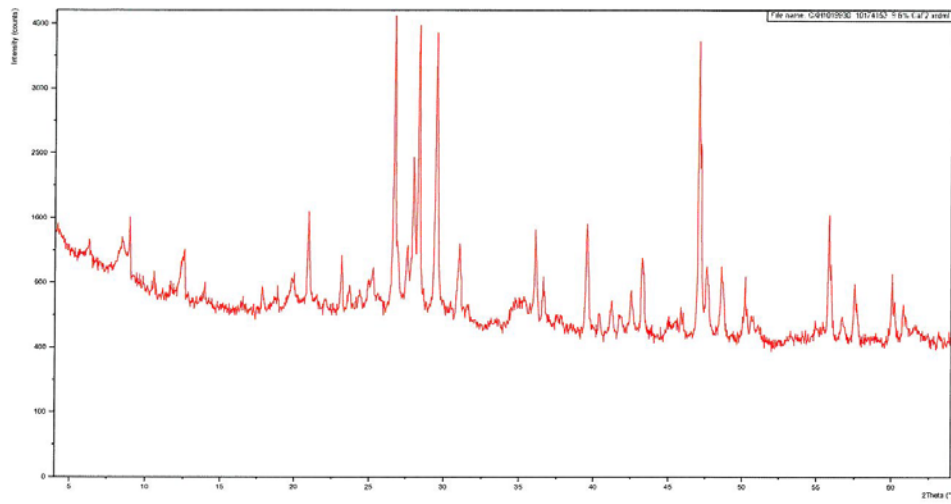


**Figure 1 –X-ray diffraction pattern of sample “A”, with degrees 2θ along the x-axis and intensity (counts) along the y-axis.**

Client Sample No.: B  
 RJ Lee Group Sample No.: 10174154

Phase	Composition	Concentration
Calcite	Ca(CO <sub>3</sub> )	26-31
Quartz	SiO <sub>2</sub>	25-30
Feldspar	(K,Na,Al)Si <sub>3</sub> O <sub>8</sub>	6-11
Dolomite	CaMg(CO <sub>3</sub> ) <sub>2</sub>	2-7
Mica	KAl <sub>2</sub> (AlSi <sub>3</sub> O <sub>10</sub> )(F,OH) <sub>2</sub>	1-5
Chlorite/Serpentine	(Mg,Al) <sub>6</sub> (Si,Al) <sub>4</sub> O <sub>10</sub> (OH) <sub>8</sub>	< 2
Palygorskite	(Mg,Al) <sub>5</sub> (Si,Al) <sub>8</sub> O <sub>20</sub> (OH) <sub>2</sub> · 8H <sub>2</sub> O	Trace*
Unknown**	-	Minor-Trace

\*Phases that we do not possess standards for cannot be quantified. Qualitative results are given in such cases.

Qualitative results are defined as: major: >20%, minor: 5-20% and trace: <5%.

\*\*Additional phases that were not identified may be present. It is also possible that there is an amorphous phase present that cannot be identified or quantified by XRD.

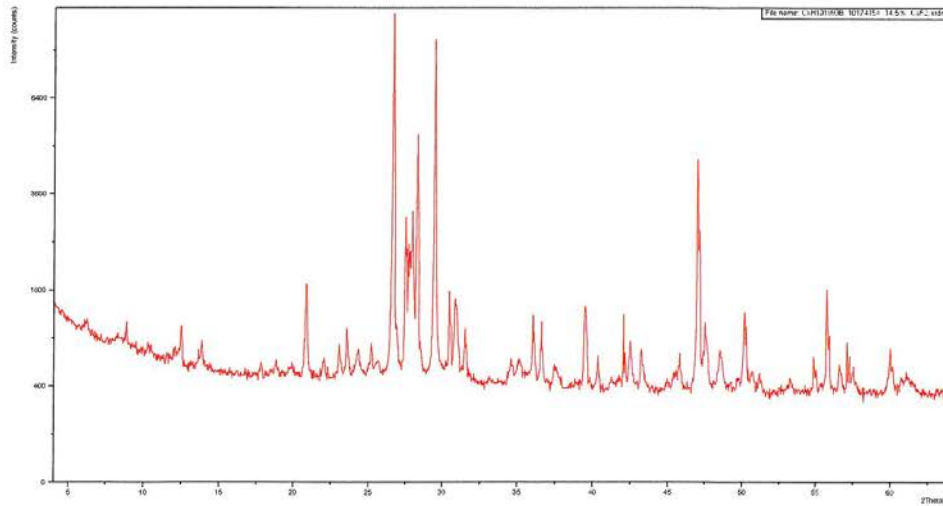


Figure 2 –X-ray diffraction pattern of sample “B”, with degrees 2θ along the x-axis and intensity (counts) along the y-axis.

Client Sample No.: C  
 RJ Lee Group Sample No.: 10174155

Phase	Composition	Concentration
Calcite	Ca(CO <sub>3</sub> )	26-31
Quartz	SiO <sub>2</sub>	25-30
Feldspar	(K,Na,Al)Si <sub>3</sub> O <sub>8</sub>	6-11
Dolomite	CaMg(CO <sub>3</sub> ) <sub>2</sub>	2-7
Mica	KAl <sub>2</sub> (AlSi <sub>3</sub> O <sub>10</sub> )(F,OH) <sub>2</sub>	1-5
Gypsum	CaSO <sub>4</sub> · 2H <sub>2</sub> O	1-5
Chlorite/Serpentine	(Mg,Al) <sub>6</sub> (Si,Al) <sub>4</sub> O <sub>10</sub> (OH) <sub>8</sub>	< 2
Palygorskite	(Mg,Al) <sub>3</sub> (Si,Al) <sub>8</sub> O <sub>20</sub> (OH) <sub>2</sub> · 8H <sub>2</sub> O	Trace*
Unknown**	-	Minor-Trace

\*Phases that we do not possess standards for cannot be quantified. Qualitative results are given in such cases.

Qualitative results are defined as: major: >20%, minor: 5-20% and trace: <5%.

\*\*Additional phases that were not identified may be present. It is also possible that there is an amorphous phase present that cannot be identified or quantified by XRD.

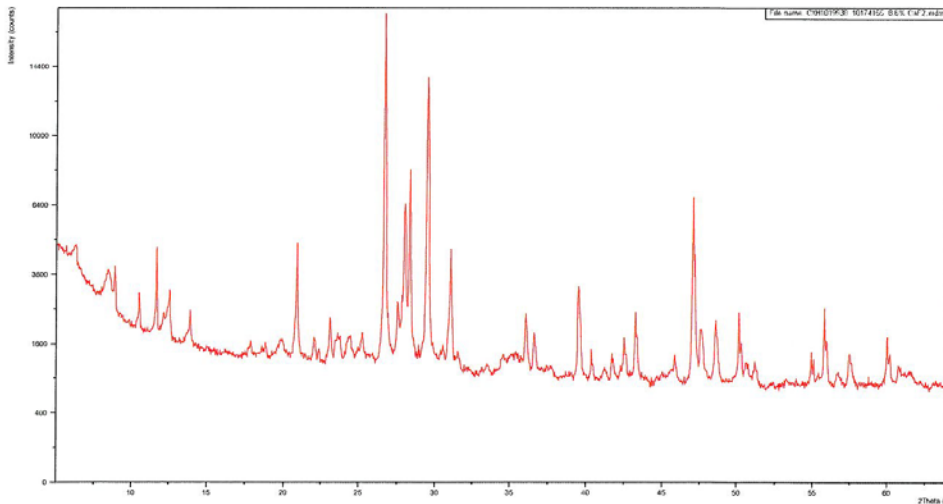
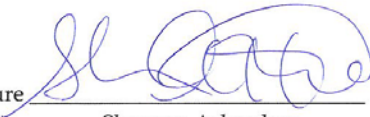


Figure 3 –X-ray diffraction pattern of sample "C", with degrees 2θ along the x-axis and intensity (counts) along the y-axis.

RJ LeeGroup, Inc.  
Project Number: CXH1019938-0  
Page 5 of 5

Authorized Signature  Date 11/23/11  
Shannon Arlauckas  
Scientist, X-ray Diffraction Group

*These results are submitted pursuant to RJ Lee Group's current terms and conditions of sale, including the company's standard warranty and limitation of liability provisions. No responsibility is assumed for the manner in which the results are used or interpreted. Unless notified in writing to return the samples covered by this report, RJ Lee Group will store the samples for a period of thirty (30) or liability days before discarding. A shipping and handling fee will be assessed for the return of any samples. This laboratory operates in accord with ISO 17025 guidelines, and holds limited scopes of accreditation under AIHA lab ID 100364, NY ELAP Lab Code 101208-0, EPA Lab Code PA00162, CA ELAP Certificate 1970, PA DEP lab ID 02-00396, VA DCLS Lab*

WWW.RJLG.COM

---

350 Hochberg Road, Monroeville, PA 15146 | PH: 724.325.1776 | F: 724.733.1799

## **APPENDIX C**

### **SPECTRAL DECONVOLUTION RESULTS FOR MINERAL MIXTURES**

Spectral deconvolution reports created by ENVI.

UnmixOut001

Calcite50-Quartz50

\*\*\*\*\* INPUT INFO \*\*\*\*\*

Number of endmembers used: 12  
Number of samples in spectra: 831  
Endmember percentages removed if below: 0

Model derived results:

Quartz 10-20:	38.4662%	//	67.0335%
Calcite 20-45:	18.9173%	//	32.9665%
Blackbody:	42.6655%		
Quartz <10:	0.0000%	//	0.0000%
Quartz 20-40:	0.0000%	//	0.0000%
Calcite <10:	0.0000%	//	0.0000%
Calcite >45:	0.0000%	//	0.0000%
Forsterite <2.7:	0.0000%	//	0.0000%
Forsterite 2.7-10:	0.0000%	//	0.0000%
Forsterite 10-20:	0.0000%	//	0.0000%
Forsterite 20-45:	0.0000%	//	0.0000%
Forsterite >45:	0.0000%	//	0.0000%
Percent summation:	100.0490%	//	100.0000%
Averaged RMS error:	0.0376		

Calcite75-Quartz25

\*\*\*\*\* INPUT INFO \*\*\*\*\*

Number of endmembers used: 12  
Number of samples in spectra: 831  
Endmember percentages removed if below: 0

Model derived results:

Calcite 20-45:	37.0703%	//	64.2792%
Quartz 10-20:	20.6005%	//	35.7208%
Blackbody:	40.7316%		
Quartz <10:	0.0000%	//	0.0000%
Quartz 20-40:	0.0000%	//	0.0000%
Calcite <10:	0.0000%	//	0.0000%
Calcite >45:	0.0000%	//	0.0000%
Forsterite <2.7:	0.0000%	//	0.0000%
Forsterite 2.7-10:	0.0000%	//	0.0000%
Forsterite 10-20:	0.0000%	//	0.0000%
Forsterite 20-45:	0.0000%	//	0.0000%
Forsterite >45:	0.0000%	//	0.0000%
Percent summation:	98.4024%	//	100.0000%
Averaged RMS error:	0.0381		

Calcite31-Quartz31-Forsterite38

\*\*\*\*\* INPUT INFO \*\*\*\*\*

Number of endmembers used: 12  
Number of samples in spectra: 831  
Endmember percentages removed if below: 0

Model derived results:

Quartz 20-40:	26.5009%	//	40.2752%
Calcite <10:	16.0928%	//	24.4573%
Forsterite 10-20:	11.2111%	//	17.0383%
Quartz 10-20:	7.0782%	//	10.7572%
Calcite >45:	4.9165%	//	7.4720%
Blackbody:	35.4974%		
Quartz <10:	0.0000%	//	0.0000%
Calcite 20-45:	0.0000%	//	0.0000%
Forsterite <2.7:	0.0000%	//	0.0000%
Forsterite 2.7-10:	0.0000%	//	0.0000%
Forsterite 20-45:	0.0000%	//	0.0000%
Forsterite >45:	0.0000%	//	0.0000%

```
UnmixOut001
Percent summation: 101.2968% // 100.0000%
Averaged RMS error: 0.0397
```

UnmixOut001

Calcite50-Quartz50

```
***** INPUT INFO *****
Number of endmembers used: 3
Number of samples in spectra: 831
Endmember percentages removed if below: 0
*****
```

Model derived results:

Quartz 10-20:	38.4292%	//	66.5857%
Calcite <10:	19.2847%	//	33.4143%
Blackbody:	42.0799%		
Percent summation:	99.7938%	//	100.0000%
Averaged RMS error:	0.0392		

Calcite75-Quartz25

```
***** INPUT INFO *****
Number of endmembers used: 3
Number of samples in spectra: 831
Endmember percentages removed if below: 0
*****
```

Model derived results:

Calcite <10:	37.8876%	//	64.9371%
Quartz 10-20:	20.4574%	//	35.0629%
Blackbody:	39.5652%		
Percent summation:	97.9103%	//	100.0000%
Averaged RMS error:	0.0436		



UnmixOut002

Calcite31-Quartz31-Forsterite38

\*\*\*\*\* INPUT INFO \*\*\*\*\*  
Number of endmembers used: 4  
Number of samples in spectra: 831  
Endmember percentages removed if below: 0  
\*\*\*\*\*

Model derived results:

Quartz 10-20:	33.0170%	//	54.4038%
Calcite <10:	19.9649%	//	32.8972%
Forsterite 10-20:	7.7069%	//	12.6990%
Blackbody:	40.5304%		
Percent summation:	101.2192%	//	100.0000%
Averaged RMS error:	0.0408		

## **APPENDIX D**

### **SATELLITE DATA**

List of all satellite data used in chapter 4.

---

Satellite Instrument	Scene ID
ASTER	AST_05_00307162008081533
	AST_05_00307162008081542
	AST_05_00307162008081551
	AST_05_00307252008080929
	AST_05_00307252008080937
	AST_05_00308082008082141
	AST_05_00308082008082150
	AST_05_00308082008082159
	AST_05_00308172008081533
	AST_05_00308172008081541
	AST_05_00308172008081550
	AST_05_00307252008080902
	AST_05_00307252008080911
	AST_05_00308012008081511
	AST_05_00308012008081520
	AST_05_00308082008082115
	AST_05_00308082008082124
	AST_05_00308172008081515
	AST_05_00308172008081524
	AST_05_00309092008082128
	AST_05_00310252004081348
	AST_05_00310252004081357

AST\_05\_00309092005073245

AST\_05\_00304042003074028

AST\_05\_00304042003074037

AST\_05\_00304042003074046

AST\_05\_00305042005073320

AST\_05\_00305042005073328

AST\_09XT\_00306072008080916

MODIS Terra

MOD021KM.A2009182.0825.005.2010246111616

MOD021KM.A2009182.1925.005.2010246113247

MOD021KM.A2009183.0730.005.2010246123723

MOD021KM.A2009185.0720.005.2010246160856

MOD021KM.A2009188.1850.005.2010246073043

MOD021KM.A2011240.0800.005.2011240151041

MOD09GA.A2010131.h21v05.005.2010133195953

MOD09GA.A2010132.h21v05.005.2010134152727

MOD09GA.A2010133.h21v05.005.2010136072941

MOD09GA.A2010134.h21v05.005.2010136142047

MOD09GA.A2010194.h21v05.005.2010196124629

MOD09GA.A2010195.h21v05.005.2010197124111

MOD09GA.A2010196.h21v05.005.2010197124111

MODIS Aqua

MYD021KM.A2010194.0820.005.2010194165529

MYD021KM.A2010195.0725.005.2010195134718

MYD021KM.A2010194.0955.005.2010195175920

MYD021KM.A2010195.1040.005.2010196153532

MYD021KM.A2010196.1120.005.2010197145634

MYD021KM.A2010129.2255.005.2010131031938

MYD021KM.A2010131.1040.005.2010132164020

MYD021KM.A2010131.2245.005.2010132171307

MYD021KM.A2010071.2255.005.2012072210122

---

## BIBLIOGRAPHY

- Akhoondzadeh, M., Saradjian, M. 2008. Comparison of Land Surface Temperature Mapping Using MODIS and ASTER Images in Semi-Arid Area. *The International Archives of the Photogrammetry, Remote Sensing and Spatial Information Sciences* 37(B8): 873-876.
- Al-Awadhi, Jasem. 2005. Dust fallout characteristic in Kuwait: a case study. *Kuwait Journal of Science and Engineering* 32:135-151.
- Al-Sulaimi, J., Khalaf, F., Mukhopadhyay, A. 1997. Geomorphological analysis of paleo drainage systems and their environmental implications in the desert of Kuwait. *Environmental Geology* 29 (1/2): 94-111
- Al-Sulaimi, J., Khalaf, F., Mukhopadhyay, A. 2000. An Overview of the Surface and Near-Surface Geology, Geomorphology and Natural Resources of Kuwait. *Earth Science Reviews* 50: 227-267.
- Alastuey, A., Querol, X., Castillo, S., Escudero, M., Avila, A., Cuevas, E., Torres, C., Romero, P., Exposito, F., Garcia, O., Diaz, P., Van Dingenen, R., Putaud, J. 2005. Characterisation of TSP and PM<sub>2.5</sub> at Izana and Sta. Cruze de Tenerife (Canary Islands, Spain) during a Saharan Dust Episode (July 2002). *Atmospheric Environment* 39(26): 4715-4728.
- Antoine, D., Nobileau, D. 2006. Recent increase of Saharan dust transport over the Mediterranean Sea, as revealed from ocean color satellite (SeaWiFS) observations. *Journal of Geophysical Research* 111.

- Athar, M., Iqbal, M., Beg, M., Al-Ajmi, D., Al-Muzaini, S. 1998. Airborne dust collected from Kuwait in 1991-1992 augments peroxidation of cellular membrane lipids and enhances DNA damage. *Environment International* 24:205-212.
- Baddock, M., Bullard, J., Bryant, R. 2009. Dust source identification using MODIS: A comparison of techniques applied to the Kale Eyre Basin, Australia. *Remote Sensing of Environment* 113: 1511-1528.
- Bagnold, R. 1941. *The physics of blown sand and desert dunes*. London: Methuen.
- Banzon, V., Evans, R., Gordon, H., Chomko, R. 2004. SeaWifs observations of the Arabian Sea southwest monsoon bloom for the year 2000. Deep-sea research part II. *Topical Studies in Oceanography* 51: 1189-1208.
- Belnap, J., Gillette, D. 1998. Vulnerability of desert biological soil crusts to wind erosion: the influences of crust development, soil texture, and disturbance. *Journal of Arid Environments* 39:133-142.
- Bhattacharjee, P., Prasad, A., Kafatos, M., Singh, R. 2007. Influence of a dust storm on carbon monoxide and water vapor over the Indo-Gangetic Plains. *Journal of Geophysical Research* 112: D18203.
- Bullard, J., McTainsh, G., Pudmenky, C. 2004. Eolian abrasion and modes of fine particle production from natural red dune sands: an experimental study. *Sedimentology* 51: 1103-1125.
- Chahine, M., Pagano, T., Aumann, H., Atlas, R., Barnett, C., Blaisdell, J., Chen, L., Divakarla, M., Fetzer, E., Goldberg, M., Gautier, C., Granger, S., Hannon, S., Irion, W., Kakar, R., Kalnay, E., Lambrigtsen, B., Lee, S., Le Marshall, J., McMillan, W., McMillan, L., Olsen, E., Revercomb, H., Rosenkranz, P., Smith, W., Staelin, D., Strow, L., Susskind, J., Tobin,

- D., Wolf, W., Zhou, L. 2006. Improving Weather Forecasting and Providing New Data on Greenhouse Gases. *Bulletin of the American Meteorological Society* 87(7):911-926.
- Christensen, P., Bandfield, J., Hamilton, V., Howard, D., Lane, M., Piatek, J., Ruff, S., Stefanov, W. 2000. A thermal emission spectral library of rock-forming minerals. *Journal of Geophysical Research* 105(E4): 9735-9739.
- Coudé-Gaussen, G. 1987. The PreSaharan loess: sedimentological characterization and paleoclimatic significance. *GeoJournal* 15:177-183.
- Dapples, E. C. 1941. Surficial Deposits of the Deserts of Syria, Trans-Jordan, Iraq, and Western Iran. *Journal of Sedimentary Petrology* 11(3): 124-141.
- DeSouza-Machado, S., Strow, L., Hannon, S., Motteler, H. 2006. Infrared dust spectral signatures from AIRS. *Geophysical Research Letters* 33: 1-5.
- Donaghay, P., Liss, P., Duce, R., Kester, D., Hanson, A., Villareal, T., Tindale, N., Gifford, D. 1991. The role of episodic atmospheric nutrient inputs in the chemical and biological ecosystems. *Oceanography* 4:62-70.
- Dufrene, Y. F. 2000. Direct characterization of the physicochemical properties of fungal spores using functionalized AFM probes. *Biophysical Journal* 78: 3286-3291.
- Edgell, Stewart H. 2006. *Arabian Deserts*. Dordrecht: Springer.
- Engelbrecht, J., McDonald, E., Gillies, J. 2009. Characterizing Mineral Dusts and Other Aerosols from the Middle East – Part 2: Grab Samples and Re-Suspensions. *Inhalation Toxicology* 21:327-336.
- Engelstaedter, S., Tegen, I., Washington, R. 2006. North African dust emissions and transport. *Earth Science Reviews* 79:73-100.



- Erell, E., Tsoar, H. 1999. Spatial variations in the aeolian deposition of dust – the effect of a city: a case study in Be'er-Sheva, Israel. *Atmospheric Environment* 33:4049-4055.
- Fischer, H., Kumke, T., Lohmann, G., Flöser, G., Miller, H., Von Storch, H., Negendank, J. eds. 2004. *The Climate in Historical Times*. New York: Springer.
- Giles, J. 2005. The dustiest place on Earth. *Nature* 434: 816-819.
- Gillespie, A., Kahle, A., Walker, R. 1986. Color-enhancement of highly correlated images. I. Decorrelation and HIS contrast stretches. *Remote Sensing of Environment* 20: 209-235.
- Gillespie, A., Mutsunaga, A., Rokugawa, S., Hook, S. 1998. Temperature and emissivity separation from Advanced Spaceborne Thermal Emission and Reflection Radiometer (ASTER) images. *IEEE Transactions on Geoscience and Remote Sensing* 36: 1113-1126.
- Gillette, D., Adams, J., Endo, A., Smith, D. 1980. Threshold velocities for input of soil particles into the air by desert soils. *Journal of Geophysical Research* 85:5621-5630.
- Gillette, D., Passi, R. 1988. Modeling Dust Emission Caused by Wind Erosion. *Journal of Geophysical Research* 93(11): 14233-14242.
- Gillette, D. A. 1999. A Qualitative Geophysical Explanation for “Hot Spot” Dust Emitting Source Regions. *Contributions to Atmospheric Physics* : 67-77.
- Goossens, D., Rajot, J. 2008. Techniques to measure the dry aeolian deposition of dust in arid and semi-arid landscapes: a comparative study in West Niger. *Earth Surface Processes and Landforms* 33(2): 178-195.
- Goudie, A. S., Middleton, N. J. 2006. *Desert Dust in the Global System*. Berlin: Springer.
- Goudie, Andrew S. 2008. The History and Nature of Wind Erosion in Deserts. *Annual Review of Earth and Planetary Sciences* 36: 97-119.

- Griffin, Dale. 2007. Atmospheric Movement of Microorganisms in Clouds of Desert Dust and Implication for Human Health. *Clinical Microbiology Reviews* 20(3): 459-477.
- Griffin, D., Kellogg, C., Shinn, E. 2001. Dust in the wind: long-range transport of dust in the atmosphere and its implications for global public and ecosystem health. *Global Change and Human Health* 2:20-33.
- Haff, P., Werner, B. 1996. Dynamical Processes on Desert Pavements and the Healing of Surficial Disturbances. *Quaternary Research* 45: 38-46.
- Hulley, G., Hook, S. 2011. Generation Consistent Land Surface Temperature and Emissivity Products Between ASTER and MODIS Data for Earth Science Research. *Transactions on Geoscience and Remote Sensing* 49(9): 1304-1315.
- Hutchison, K., Iisager, B., Kopp, T., Jackson, J. 2008. Distinguishing Aerosols from Clouds in Global, Multispectral Satellite Data with Automated Cloud Classification Algorithms. *Journal of Atmospheric and Oceanic Technology* 25: 501-518.
- Jickells, T., An, Z., Anderson, K., Baker, A., Bergametti, G., Brooks, N., Cao, J., Boyd, P., Duce, R., Hunter, K., Kawahata, H., Kubilay, N., LaRoche, J., Liss, P., Mahowald, N., Prospero, J., Ridgwell, A., Tegen, I., Torres, R. 2005. Global Iron Connections Between Desert Dust, Ocean Biogeochemistry, and Climate. *Science* 308: 67-71.
- Johnson, J., Grundy, W., Shepard, M. 2004. Visible/near-infrared spectrogoniometric observations and modeling of dust-coated rocks. *Icarus* 171: 546-556.
- Joo, Y., An, S., Kim, O., Lubroth, J., Sur, J. 2002. Foot-and-mouth disease eradication efforts in the Republic of Korea. *Canadian Journal of Veterinary Research* 66:122-124.

- Kahn, B., Eldering, A., Clough, S., Fetzer, E., Fishbein, E., Gunson, M., Lee, S., Lester, P., Realmuto, V. 2003. Near micron sized cirrus cloud particles in high-resolution infrared spectra: An orographic case study. *Geophysical Research Letters* 30(8): 1441-1446.
- Katra, I., Lancaster, Ni. 2008. Surface-sediment dynamics in a dust source from spaceborne multispectral thermal infrared data. *Remote Sensing of Environment* 112: 3212-3221.
- Kearly, P., Hook, S. 1993. Separating Temperature and Emissivity in Thermal Infrared Multispectral Scanner Data: Implication for Recovering Land Surface Temperatures. *Transactions on Geoscience and Remote Sensing* 31(6): 1155-1164.
- Kim, S., Yoon, S., Jefferson, A., Won, J., Dutton, E., Ogren, J., Anderson, T. 2004. Observation of enhanced water vapour in Asian dust layer and its effect on atmospheric radiative heating rates. *Geophysical Research Letters* 13: L18113.
- King, M., Kaufman, Y., Menzel, P., Tanre, D. 1992. Remote Sensing of Cloud, Aerosol, and Water Vapor Properties from the Moderate Resolution Imaging Spectrometer (MODIS). *Transactions on Geoscience and Remote Sensing* 30(1): 2-27.
- King, M., Kaufman, Y., Tanre, D., Nakajima, T. 1999. Remote Sensing of Tropospheric Aerosols from Space: Past, Present, and Future. *Bulletin of the American Meteorological Society* 80(11): 2229-2259.
- Kirkland, L., Herr, K., Keim, E., Adams, P., Salisbury, J., Hackwell, J., Treiman, A. 2002. Fire use of an airborne thermal infrared hyperspectral scanner for compositional mapping. *Remote Sensing of Environment* 80: 447-459.
- Kutiel, H., Furman, H. 2003. Dust Storms in the Middle East: Sources of Origin and their Temporal Characteristics. *Indoor and Built Environment* 12: 419-426.

- Le Bras, A., Erard, S. 2003. Reflectance spectra of regolith analogs in the mid-infrared: effects of grain size. *Planetary and Space Science* 51: 281-294.
- Levy, R., Remer, L., Tanre, D., Kaufman, Y., Ichoku, C., Holben, B., Livingston, J., Russell, P., Maring, H. 2003. Evaluation of the Moderate-Resolution Imaging Spectroradiometer (MODIS) retrievals of dust aerosol over the ocean during PRIDE. *Journal of Geophysical Research* 108(D19): 8594.
- Liu, W., Wu, E. 2005. Comparison of non-linear mixture models: sub-pixel classification. *Remote Sensing of Environment* 94: 145-154.
- Lyles, M., Fredrickson, H., Bednar, A., Fannin, H., Sobocki, T. 2005. The chemical biological, and mechanical characterization of airborne micro-particulates from Kuwait. Abstract. 8<sup>th</sup> Annual Force Health Protection. Conf., session 2586, Louisville, KY.
- Maher, B., Prospero, J., Mackie, D., Gaiero, D., Hesse, P., Balkanski, Y. 2010. Global connections between aolian dust, climate and ocean biogeochemistry at the present day and at the last glacial maximum. *Earth Science Reviews* 99:61-97.
- McFadden, L., Wells, S., Jercinovich, M. 1987. Influences of eolian and pedogenic processes on the origin and evolution of desert pavement. *Geology* 15: 504-508.
- Miller, S., Kuciauskas, A., Liu, M., Ji, Q., Reid, J., Breed, D., Walker, A., Al Mandoos, A. 2008. Haboob dust storms of the southern Arabian Peninsula. *Journal of Geophysical Research* 113.
- Mills, M., Ridame, C., Davey, M., La Roche, J., Gelder, R. 2004. Iron and phosphorous co-limit nitrogen fixation in the eastern tropical North Atlantic. *Nature* 429: 292-294.
- Nicholson, S E. 2000. Land surface processes and Sahel climate. *Reviews of Geophysics* 38:117-139.

- Pollastro, R., Karshbaum, A., Viger, R. 1997. Maps Showing Geology, Oil and Gas Fileds and Geologic Provinces of the Arabian Peninsula. U.S. Geological Survey Open-File report 97-470B
- Ramsey, M., Christensen, P. 1998. Mineral abundance determination: Quantitative deconvolution of thermal emission spectra. *Journal of Geophysical Research* 103: 577-596.
- Ramsey, M., Christensen, P., Lancaster, N., Howard, D. 1999. Identification of sand sources and transport pathways at the Kelso Dunes, California using thermal infrared remote sensing. *Geologic Society of America Bulletin* 111: 646-662.
- Ramsey, M., Fink, J. 1999. Estimating silicic lava vesicularity with thermal remote sensing: a new technique for volcanic mapping and monitoring. *Bulletin of Volcanology* 61: 32-39.
- Ramsey, M. 2004. *Quantitative geological surface processes extracted from infrared spectroscopy and remote sensing, in Infrared Spectroscopy in Geochemistry, Exploration, and Remote Sensing*, P. King, M. Ramsey, G. Swayze (eds.), Mineral. Assoc. of Canada, London, ON, 33, 197-213.
- Reheis, M. C. 2006. A 16-year record of eolian dust in Southern Nevada and California, USA: Controls on dust generation and accumulation. *Journal of Arid Environments* 67: 487-520.
- Ruff, S., Christensen, P., Barbera, P., Anderson, D. 1997. Quantitative thermal emission spectroscopy of minerals: A laboratory technique for measurement and calibration. *Journal of Geophysical Research* 102(B7): 14899-14913.
- Sabins, Floyd. 1997. *Remote Sensing: Principles and Interpretation*. WH. Freeman: New York.
- Salisbury, J., D'Aria, D. 1992. Emissivity of Terrestrial Materials in the 8-14  $\mu\text{m}$  Atmospheric Window. *Remote Sensing of Environment* 42: 83-106.

- Salisbury, J., Wald, A. 1991. The Role of Volume Scattering in Reducing Spectral Contrast of Reststrahlen Bands in Spectra of Powdered Minerals. *ICARUS* 96: 121-128.
- Salisbury, J., Walter, L., Vergo, N., D'Aria, D. 1991. *Infrared (2.1-25  $\mu\text{m}$ ) Spectra of Minerals*. Baltimore: The Johns Hopkins University Press.
- Salomonson, V., Barnes, W., Maymon, P., Montgomery, H., Ostrow, H. 1989. MODIS: Advanced facility instrument for studies of the earth as a system. *Transactions on Geoscience and Remote Sensing* 27: 145-153.
- Sanders, J., Putnam, S., Frankart, C., Frenck, R., Monteville, M., Riddle, M., Rochabrand, D., Sharp, T., Tribble, D. 2005. Impact of illness and non-combat injury during operations Iraqi Freedom and Enduring Freedom (Afghanistan). *American Journal of Tropical Medicine and Hygiene* 73: 713-719.
- Sarthou, G., Baker, A., Blain, S., Achterberg, E., Boye, M., Bowie, A., Croot, P., Laan, P., de Baar, H., Jickells, T., Worsfold, P. 2003. Atmospheric iron deposition and sea-surface dissolved iron concentrations in the eastern Atlantic Ocean. *Deep-sea Research Part I* 50:1339-1352.
- Scheidt, Stephen. 2009. Aeolian System Dynamics Derived from Thermal Infrared Data. PhD dissertation, *University of Pittsburgh*, Pittsburgh.
- Sokolik, I., Toon, O. 1999. Incorporation of mineralogical composition into models of the radiative properties of mineral aerosol from UV to IR wavelengths. *Journal of Geophysical Research-Atmospheres* 104:9432-9444.

- Strow, L., Hannon, S., Weiler, M., Overoye, K., Gaiser, S., Aumann, H. 2003. Prelaunch Spectral Calibration of the Atmospheric Infrared Sounder (AIRS). *Geoscience and Remote Sensing IEEE transactions* 41(2): 274-284.
- Stunder, B., Draxler, R. 2010. HYSPLIT model description and operational set up for benchmark case study. Workshop on Ash Dispersal Forecast and Civil Aviation, Geneva.
- Subba Row, D., Al-Yamani, F., Nageswara Rao, C. 1999. Eolian dust effects phytoplankton in the water off Kuwait, the Arabian Gulf. *Naturwissenschaften* 86: 525-529.
- Swap, R., Garstang, M., Greco, S. 1992. Saharan dust in the Amazon Basin. *Tellus* 44B: 133-149.
- Thomson, J., Salisbury, J. 1993. The Mid-Infrared Reflectance of Mineral Mixtures (7-14  $\mu\text{m}$ ). *Remote Sensing of Environment* 45(1): 1-13.
- Vaughan, R., Hook, S., Calvin, W., Taranik, J. 2005. Surface mineral mapping at Steamboat Springs, Nevada, USA, with multi-wavelength thermal infrared images. *Remote Sensing of Environment* 99: 140-158.
- Vincent, R., Hunt, G. 1968. Infrared Reflectance from Mat Surfaces. *Applied Optics* 7(1): 53-59.
- Washington, R., Engelstaedter, S. 2007. Temporal controls on global dust emissions: The role of surface gustiness. *Geophysical Research Letters* 34: L15805.
- Washington, R., Todd, M., Middleton, N., Goudie, A. 2003. Dust-Storm Source Areas Determined by the Total Ozone Monitoring Spectrometer and Surface Observations. *Association of American Geographers* 93(2): 297-313.

- Wells, S., Dohrenwend, J., McFadden, L., Turrin, B., Mahrer, K. 1985. Late Cenozoic landscape evolution on lava flow surfaces of the Cima volcanic field, Mojave Desert, California. *Geological Society of America Bulletin* 96: 1518-1529.
- Wentworth, C. 1922. A scale of grade and class terms for clastic sediments. *Journal of Geology* 30:377-392.
- Williams, S., Zimbelman, J. 1994. Desert Pavement Evolution: An Example of the Role of Sheetflood. *The Journal of Geology* 102: 243-248.
- Wolfe, A., Liu, R., Stewart, B., Capo, R., Dzombak, D. 2007. A method for generating uniform size-segregated pyrite particle fractions. *Geochemical Transactions* 8, 9.
- Yaalon, D., Ganor, E. 1973. The influence of dust on soils during the Quaternary. *Soil Science* 116: 146-155.
- Yan, H., Wang, S., Wang C., Zhang G., Patel N. 2005. Losses of soil organic carbon under wind erosion in China. *Global Change Biology* 11: 828-840.
- Zender, C., Bian, H., Newman, D. 2002. The mineral Dust Entrainment And Deposition (DEAD) model: Description and 1990s dust climatology. *Journal of Geophysical Research* 108.